TECHNISCHE UNIVERSITÄT WIEN
Vienna University of Technology

MedAustron

DIPLOMARBEIT

Experimental Validation of the Energy Verification System for Radio Frequency Knockout Extractions at MedAustron

Zur Erlangung des akademischen Grades

Diplom-Ingenieur/in

Im Rahmen des Studiums

Technische Physik

eingereicht von

Felix Feichtinger BSc

Matrikelnummer 01525919

ausgeführt am AtomInstitut
der Fakultät für Physik der Technischen Universität Wien
in Zusammenarbeit mit MedAustron

Betreuung:
Assistant Prof. Dipl.-Ing. Dr.techn. Albert Hirtl (TU Wien)
Assoc. Prof. Dr. Dale Prokopovich (MedAustron)
DDI Dr. Alexander Wastl (MedAustron)

Abstract

One of the most important prerequisites for the medical operation of a particle accelerator is the precise control of the particle energy, since due to the direct proportionality to the penetration depth, even a slight deviation can lead to damage to a patient's healthy tissue. At MedAustron, this control is performed by the 'Energy Verification System (EVS)'. In the event of an energy deviation that leads to a change in the penetration depth of more than 0.3 mm, this system immediately deflects the particle beam into the beam dump.

With the introduction of a new extraction method, the Radio Frequency Knockout (RFKO), a modification of the EVS is necessary. The approach for the new system is a verification via the magnetic field of the dipole magnets and the revolution frequency of the particles, which will be the content of this thesis. For this purpose, measurements of the frequency at the accelerating radio frequency cavity (RFC), the magnetic field at the dipole magnets and range measurements based on the bragg peak position using the PTW Peakfinder system in the irradiation room will be performed simultaneously in RFKO operation. A deviation of the particle energy from the nominal value, measured by the Peakfinder, should be visible in both the RFC and the magnetic field measurements. An analysis of these data should show that the chosen approach is suitable for the new EVS.

Zusammenfassung

Eine der wichtigsten Vorraussetzungen für den medizinischen Betrieb eines Teilchenbeschleunigers ist die genaue Kontrolle der Teilchenenergie, da aufgrund der direkten Proportionalität zur Eindringtiefe, schon eine geringe Abweichung zu Schäden am gesunden Gewebe einer behandelten Person führen kann. Am MedAustron wird diese Kontrolle vom "Energy Verification System (EVS)" übernommen. Dieses lenkt, bei einer Energieabweichung, welche zu einer Änderung der Eindringtiefe von mehr als 0.3 mm führt, den Teilchenstrahl sofort in den Beamdump ab.

Mit der Einführung einer neuen Extraktionsmethode, dem Radio Frequency Knockout (RFKO), ist eine Anpassung des EVS notwendig. Der Ansatz für das neue System ist eine Verifikation über das Magneteld der Dipolmagnete und die Umlauffrequenz der Teilchen. Diese Arbeit soll sich nun im Folgenden mit der Validierung dieser Methode beschäftigen. Hierzu sollen im RFKO Betrieb gleichzeitig Messungen der Frequenz an der beschleunigenden Radiofrequency Cavity (RFC), des Magnetfelds an den Dipolmagneten und Reichweiten-Messungen basierend auf der Bragg-Peak Position mit dem PTW Peakfinder im Bestrahlungsraum durchgeführt werden. Eine Abweichung der Teilchenenergie vom Sollwert, gemessen durch den Peakfinder, sollte sowohl in den RFC-, als auch den Magnetfeldmessungen sichtbar sein. Eine Analyse dieser Daten soll zeigen, dass der gewählte Ansatz für das neue EVS geeignet ist.

Contents

1. Introduction

Ion therapy is a remarkable advancement in the fight against cancerous diseases. Using the properties of charged particles travelling through matter, tumors can be treated with minimal damage to the surrounding tissue. The penetration depth of an ion beam can be matched with the depth of the tumor in the body, by adjusting the particle's kinetic energy, i.e. the particle velocity.
While this concept is simple enough, the practicalities of accelerating a particle to a viable energy, are quite complex. To create ions, atoms have to be stripped of their electrons, selected for the charge and mass state, accelerated to the desired energy and delivered to the patient on a designed path without major losses. Things are complicated even more by the fact, that the energies required for therapy are so high, that linear accelerators are no longer practical. For example, a proton beam requires a kinetic energy of 60 MeV for a penetration depth of just 3 cm. For this reason circular solutions like the *synchrotron* have to be applied. Here, particles are moving on a circular path, while being accelerated every turn. This means that, not only is the problem of keeping particles on their track amplified, but also getting them in and out of the *storage ring*, i.e. injection and extraction turn out to be very difficult challenges in themselves. Many parameters need to be tuned precisely to avoid a scraping of the beam at the walls of the machine. This means, that a successful extraction results in a beam at the desired kinetic energy, as only a tiny deviation would have most likely caused the total loss of the particles. It is, however, not entirely impossible to have these kind of deviations in an extracted beam. Furthermore, since such scenarios would compromise patient safety significantly, preventative actions have to be taken.

At the MedAustron center for particle therapy and research, located in Wiener Neustadt, Austria [1], the so called *Energy Verification System* (EVS) was installed as a safety measure for preventing the incorrect energy at flat top from being extracted. MedAustron features a synchrotron of 77.65m in circumference, providing proton beams between 62.4 and 252.7 MeV and carbon ions between 120.0 and 402.8 MeV/u, which are guided into the facility's four *irradiation rooms* (IR's), as seen in fig. 1.1. IR 2, 3 and 4 are designated for therapy purposes, while IR 1 is exclusively used for *non clinical research* (NCR) and testing components. Additionally IR1 can be provided with a proton setting of 800 MeV for NCR.

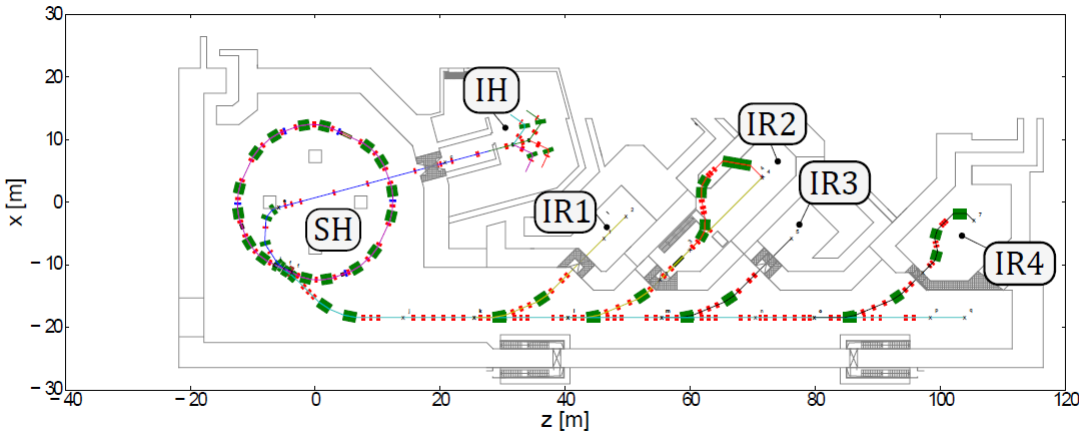

Figure 1.1.: Layout of MedAustron [2]: Particles are guided from the injector hall (IH) to the synchrotron hall (SH), where they are accelerated to the required energy and subsequently extracted into the IR's.

Particles originate in the injector hall, which can host up to four different particle source arms. They are then bunched, accelerated by the linac to around 7 MeV/u and injected into the synchrotron. The extraction of particles is conducted by the methods described in sec. 2.2.2 and yields particles in spills of 10 sec for clinical purposes.
The EVS measures the beam energy of those spills before the extraction, indirectly via the revolution frequency of the particles in the storage ring and the magnetic field of the dipole magnets keeping the beam on a circular path. The energy measurement has to be indirect, as direct measurements would interfere with the beam. If an unsafe energy deviation is detected, the beam will be extracted normally, but then guided into the *beam dump* - a massive tungsten block in the *high energy beam transfer line* (HEBT), which leads from the storage ring to the IR's [3].
An energy deviation is considered unsafe, if it exceeds $\pm 0.03\ g/cm^2$ which is approximately equivalent to 0.3 mm in water. Though the frequency and B-field deviations triggering the EVS can be calculated, a validation by experiment is imperative for safe operating conditions. Moreover, the validation has to be done for every extraction method separately as conditions can be very different (see sec. 2.2.2).
For this thesis, the experimental validation for the *Radio Frequency Knockout* (RFKO) extraction method will be performed. This extraction method is newly introduced [4] at MedAustron alongside the already EVS-validated and regularly applied *Betatron Core extraction*. The validation method itself includes the simul-

taneous measurements of the revolution frequency, B-field and penetration depth in the patient, with the bulk of the project being the data processing, to acquire meaningful results. Hence, this thesis will focus more on the practical side of constructing a validation method, conducting the measurements and data processing, rather than synchrotron kinematics. The necessary basics for understanding the topic however, including an overview of the behaviour of charged particles in matter and the basics of accelerator physics, will of course be outlined in chapter 2 - *Physical Principles*. In chapter 3 - *Materials and Methods*, the general idea for the validation procedure, plus the used methods of data acquisition and processing are described. Finally, measurement and model results are presented and plotted in chapter 4 - *Results* and are discussed in chapter 5 - *Discussion*.

2. Physical Principles

2.1. Interaction of Charged Particles with Matter

The energy loss of charged particles traveling through matter is known as the *stopping power* S, which is a composite of various effects. For low ion energies, nuclear losses, coming from electromagnetic interaction between the ion and the nuclei of the materials atoms, are most prevalent. At very high ion energies radiative losses, meaning bremsstrahlung, are the main cause for energy loss. The last important effect is electronic stopping, which occurs due to interaction between the ion and the electronic shell of the materials atoms. This is the main contributor to the stopping power for the MeV to low GeV energy range. The stopping power over ion energy and the different effect regions can be seen in fig. 2.1. Since energies used in ion particle therapy are of the order $\sim 10^2$ MeV, the effect of electronic stopping shall be investigated further.

Bethe Bloch Formula and Particle Range

The idea for a model of electronic stopping was introduced by Bohr and was in its classical form only dependent on the time, that a moving ion would spend in the vicinity of a shell electron and the resulting momentum transfer. This consideration alongside some relativistic corrections leads to the Bethe-Bloch formula [6]

$$-\frac{dE}{dx} = 2\pi N_\mathrm{a} r_\mathrm{e}^2 m_\mathrm{e} c^2 \rho \frac{Z}{A}\frac{z^2}{\beta^2}\left[ln\left(\frac{2m_\mathrm{e}\gamma^2\beta^2 c^2 W_\mathrm{max}}{I^2}\right) - 2\beta^2\right], \tag{2.1}$$

where

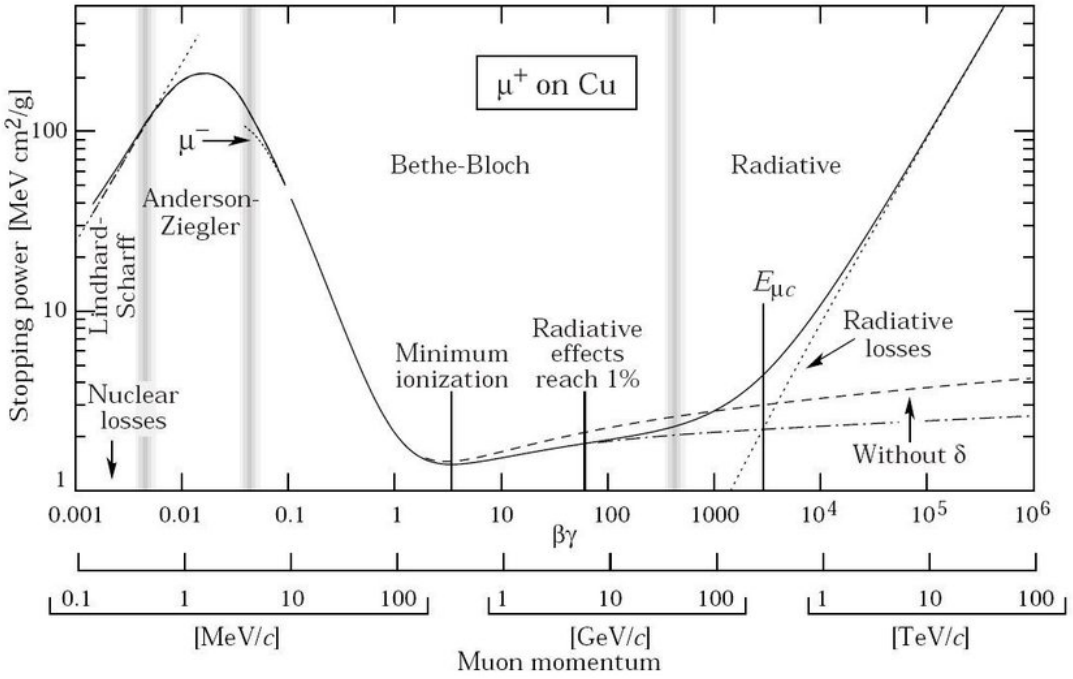

Figure 2.1.: The stopping power of charged particles has several distinct regions. In the Bethe Bloch region, the stopping power dependence is v^{-2} for low energies, but for higher energies a relativistic rise can be seen. At lower energies the Lindhard-Scharf region, describing nuclear losses and the interpolated Anderson Ziegler region can be seen. At high energies, the rise of nuclear losses can be observed. These regions are observed for all charged particles [5].

$\frac{dE}{dx}$ = The particles energy change per travelled distance
N_a = Avogadro constant
r_e = Classical electron radius
m_e = Electron mass
ρ = Density of the absorbing material
Z = Atomic number of the absorbing material
A = Atomic weight of the absorbing material
z = Charge of particle in units of e
I = Mean excitation potential
W_max = Maximum energy transfer in a single collision

It can be seen, that the stopping power changes during the interaction since a loss of energy causes a decrease in velocity and in turn a higher stopping power, leading to more energy loss. This cycle will repeat until the particle either exits

the material, or looses all of its kinetic energy. While the first case is not of interest for medical application, the second case will lead to what is called the *Bragg peak*, which can be seen by plotting $\frac{dE}{dx}$ over x, as shown in fig.2.2. Thus, the depth of the peak a certain particle entering a specific material reaches, is only dependent on its kinetic energy. This is very useful for cancer therapy, as an ion beam can be "tuned" to destroy tumors at a certain depth via ionization, while leaving healthy tissue before and after the tumor mostly intact.

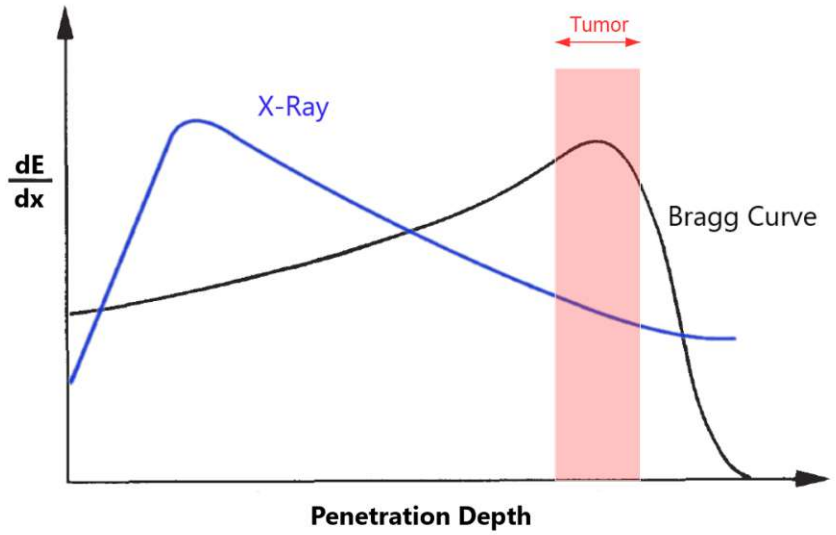

Figure 2.2.: While X-ray photons will deposit most of their energy directly after entering the body, thus damaging healthy tissue, a proton beam can be tuned via its kinetic energy, to have its peak in the desired region.

A theoretical approach to calculating the penetration depth or *Range*, is the concept of the *continuous slowing down approximation* (CSDA) range which describes the depth at which a particle has lost all of its energy by slowing down continuously in the material. It can be calculated by integrating the inverse stopping power from the initial energy to rest, thus

$$R_{\mathrm{CSDA}} = \int_0^E \left(\frac{dE}{dx}\right)^{-1} dE. \tag{2.2}$$

Range approximations

Since the integral in eq. (2.2) can be difficult to solve, either numerical methods or approximations are often used to calculate the range. One analytic simplification can be found by considering, that the only parameter changing during the interaction in this model is the velocity i.e. β. For energies that are not too high, the logarithmic term in eq. (2.1) can be ignored, thus

$$-\frac{dE}{dx} \propto \beta^{-2} \propto E^{-1} \tag{2.3}$$

and therefore:

$$R \propto E^2. \tag{2.4}$$

For a more accurate fit W.R. Leo [6] suggests

$$R \propto E^{1.75}. \tag{2.5}$$

From measured or simulated particle depths at known energies a simple scaling constant $a(E)$ can be found, to approximate ranges at similar energies, with

$$a(E) = \frac{R}{E^{1.75}}. \tag{2.6}$$

To find ranges for different particle charges and masses, scaling laws of the form

$$R_2(E_2) = \frac{M_2}{M_1}\frac{z_1^2}{z_2^2} R_1\left(E_2 \frac{M_1}{M_2}\right) \tag{2.7}$$

can be used, where

M_1 = Mass of the original particle
M_2 = Mass of the particle whose range is to be calculated
z_1 = Nuclear charge of the original particle
z_2 = Nuclear charge of the particle whose range is to be calculated

With these simple calculations a surprisingly accurate range estimate, with a relative error of only a couple % can be found for ∼100 MeV around the reference scaling constant. This can serve as a convenient tool to approximate particle range at a given kinetic energy and help to get an intuition of the matter.

Another approximation method would be, to just use a polynomial of the n^{th} order. For charged particles in water, a polynomial of the 4^{th} order

$$R(E) = a_0 + a_1 E + a_2 E^2 + a_3 E^3 + a_4 E^4, \tag{2.8}$$

yields excellent result [7]. The a_i can be determined easily by a fit of either simulations, or previously measured data.

Bragg Peak Properties

The range of a particle is not only defined by the CSDA range, however. In practice the position of the peak itself and most commonly the R_{80}, the position after the peak at which the dose has reached 80% of its maximum, are used. Especially the R_{80} yields very reliable results, since the distal slope is usually quite steep, which makes measured statistical dose fluctuations have less impact on the range.
Accordingly values like theR_{50} and R_{20} are defined as additional parameters of the peak. Also values like the width of the peak at certain heights like the R_{80} or R_{50} (FWHM), or the *penumbra* width (distance between R_{80} and R_{20}) can be used to characterize the curve as seen in fig. 2.3.

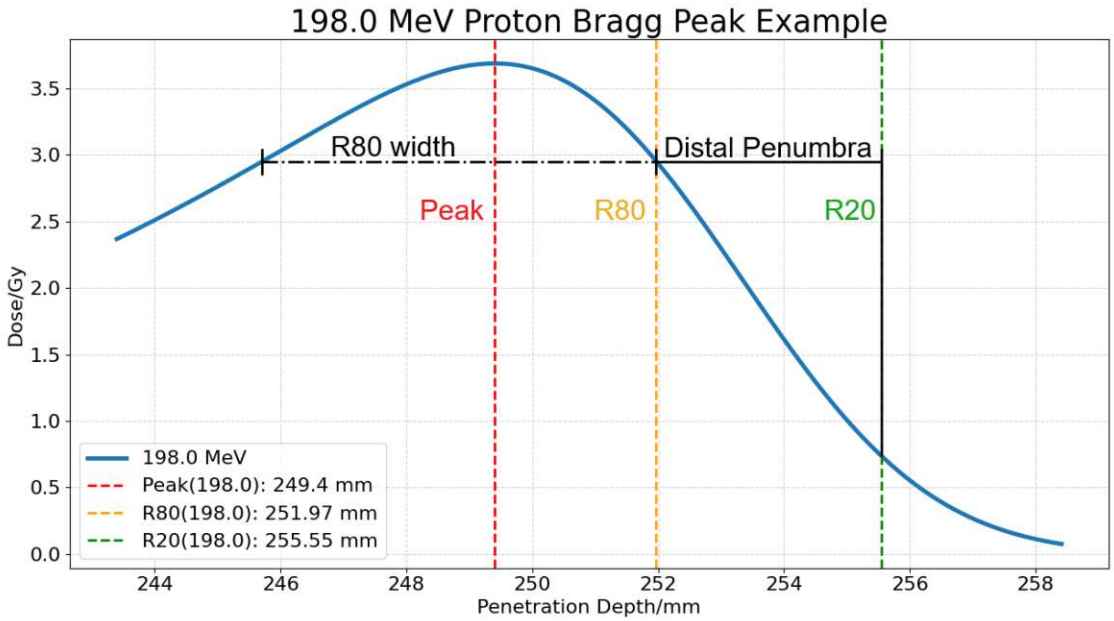

Figure 2.3.: Important properties of the Bragg peak, described in this thesis are: The Peak (red), R_{80} (yellow), R_{20} (green), R_{80} width (distance between the first and second R_{80}) and penumbra width (distance between R_{80} and R_{20}).

Lastly, there are some additional points, that won't impact the methods or results of this thesis, but should be mentioned nonetheless:

- Measuring the Bragg curve of a single particle with the same energy repeatedly will not reveal the Bragg peak, as the interaction between particle and material is a statistical process i.e. not every particle will experience the same number of collisions. This phenomenon is known as *range straggling* [6]. In this thesis, however, straggling is not an important factor, as only the statistical mean of $\sim 10^{10}$ particles is recorded.
- The Bragg curve of particles Z>1 will show a slowly decaying tail after the CSDA range due to fragmentation and resulting dose deposition of the emerging sub-particles. However, the form of the curve in the R_{80} region will be unaffected by this.

2.2. Particle Accelerators

Charged particles can be accelerated to high velocities i.e. energies by electromagnetic means such as an either static or alternating electric field for the acceleration itself and a magnetic field for controlling the particle's path. A literal straightforward concept is the group of linear particle accelerators, a term which, today, is most commonly used for machines operated by AC Voltage. One of the first advancements and a descriptive example of this concept is the *Wideröe accelerator* [8], which can be seen in principle in fig. 2.4. Here, particles are guided through pipes of alternating potential in bunches. Since the inside of the pipes are field-free, acceleration can only happen between the pipes. This means, that at a constant applied frequency, pipes need to get longer accounting for the increasing particle velocity. Additionally, the number of bunches per second is limited by the AC frequency.

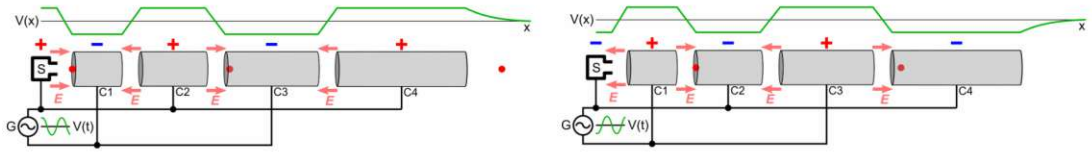

(a) t=0 (b) t=$\frac{\tau}{2}$

Figure 2.4.: In the Wideröe linear accelerator concept an alternating voltage in the pipes results in an alternating electric field between them and thus inducing an electric force on passing particles [9].

While proton energies of some MeV can be achieved by this solution, the potential for higher output energies is pretty limited due to excessive length requirements. This drawback is completely negated by a circular design, having only one acceleration section and guiding particles on a circular path using magnetic fields. In fig. 2.5, two examples of this principle can be seen. The *cyclotron* consists of two semi-circular electrodes on opposite changing electric potentials in a vacuum and an ion source in the middle, thus, like with the Wideröe machine, particles only get accelerated in the gap between the electrodes. Since the AC frequency and the magnetic field are constant, the particles radius gets bigger with increasing speed, until their spiraling path reaches a deflecting electrode, guiding them into the outgoing beam line. With this, cyclotrons usually reach energies from 10-50 MeV but can go as high as 500 MeV. For higher energies, relativistic effects will cause the particles' circular frequency to be out of tune with the AC frequency, requiring a different solution for further acceleration.

2.2.1. Synchrotron

In the synchrotron solution, the magnetic fields are continously adjusted to the particle energy and thus it is not susceptible to the cyclotrons tuning problem. Here, particles are guided through a vacuum pipe by multiple electromagnets. They are usually pre-accelerated by a linac and enter the synchrotron at about 10-20 MeV. Unlike the cyclotron, the particles' radius is kept constant, because the magnetic field is increasing along with the particle momentum, in a process known as *ramping*. Once the ramping process is complete, meaning the desired energy is reached, the beam will be extracted, the magnets will go into hysteresis and the whole process can repeat. As a result of this cycle-based acceleration, the final beam will not be delivered continuously, but rather in a so called *spill* structure. Spill lengths are determined by the extraction method and are usually in the order of a few seconds for slow methods. Energies are practically only restricted by the electromagnet's strength and the curvature of the pipe in them, since particles between the magnets are travelling in straight lines. This means that also the size of the synchrotron itself will affect the energy output. Large synchrotrons can (with some pre-acceleration synchrotrons) reach kinetic energies up to TeV (*Large Hadron Collider*).

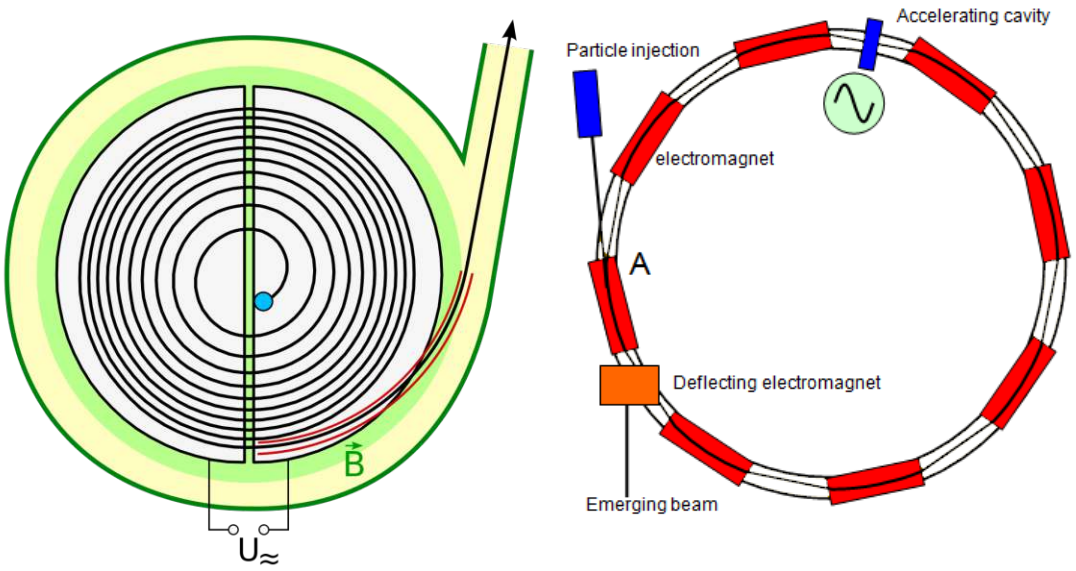

(a) Cyclotron (b) Synchrotron

Figure 2.5.: Examples for circular accelerators [10][11].

2.2.2. Extraction Methods

An important topic for synchrotrons, especially in this thesis, is the extraction of the particle beam from the main ring. In contrast to the cyclotron, where the beam will exit its spiraling path automatically at a certain energy by design, particles on a circular path in a synchrotron will have to be extracted by a separate mechanism. In the following section, the Betatron core and the Radio Frequency Knock Out (RFKO) extraction methods are discussed [12].

The general idea for these extraction methods is to get the beam to oscillate around the design path with an increasing amplitude. This can be achieved by having particles travel off the design path, where focusing elements like quadrupole magnets will try to force them back on again, causing them to oscillate around the design path. Once the amplitude is big enough, the beam can step over the *electrostatic septum*, which consists of two electrodes generating an electrostatic field, guiding particles oscillating strongly enough into the extraction line. To increase the amplitude to a point, where particles can be extracted, the beam has to be in a resonant (unstable) state. This resonance is achieved by having oscillation interfere constructively every n^{th} turn, forming a standing wave. An illustrative variable describing the resonance is the so called *tune* Q

$$Q = \frac{1}{2\pi} \oint_C \phi(s) ds, \tag{2.9}$$

where C would be the circumference of the synchrotron and $\phi(s)$ the phase advance, describing how much a particle would oscillate per path length s. Thus the tune can be understood as the number of oscillations for each turn. Since beam-optical properties can differ between the horizontal and vertical axis, the respective tunes Q_h for the horizontal and Q_v for the vertical tune can be different as well. Subsequently, a beam at an integer value $Q_\mathrm{h} = n$ in horizontal tune, with $n \in \mathbb{N}$ would be amplifying every turn, a value $Q_\mathrm{h} = \frac{n}{2}$ every second turn, $Q_\mathrm{h} = \frac{n}{3}$ every third turn and so on. These instances are called resonances of the first, second, third, etc. order respectively. Thus, higher order resonances will grow the amplitude slower. However, the tune will change for particles not travelling on the design path, so called *off momentum* particles, as focusing elements are affecting them differently. A subsequently occurring change in tune ΔQ can be described by

$$\Delta Q = Q' \frac{\Delta p}{p}, \tag{2.10}$$

where Δp is the momentum difference between off and on momentum particle with respect to the momentum p and Q' is a machine dependent parameter called

chromaticity. The horizontal spatial offset Δx from the design path an off momentum particle will experience, also called *radial loop offset*, can be related to the momentum offset $\frac{\Delta p}{p}$ via another machine parameter called the *dispersion* D_x

$$\Delta x = D_x \frac{\Delta p}{p}. \tag{2.11}$$

Even though, the chromaticity Q' and the dispersion D_x can be used as simple proportionality constants from a momentum spread $\frac{\Delta p}{p}$ to a change in tune and particle path, they are complex parameters, depending on the beam optics of the machine. Due to their complexity and sensitivity, they are often determined experimentally.

Finally, the resonance can be widened into an unstable region by introducing achromatic sextupole magnets, causing non-linear focusing effects on the beam. These effects depend on various beam parameters, most importantly the amplitude of particle oscillations. The widening of the unstable region can be seen in a so called *Steinbach Diagram* [12] in fig. 2.6, plotting the amplitude of a *waiting beam* (blue rectangle) against its momentum offset $\frac{\Delta p}{p}$.

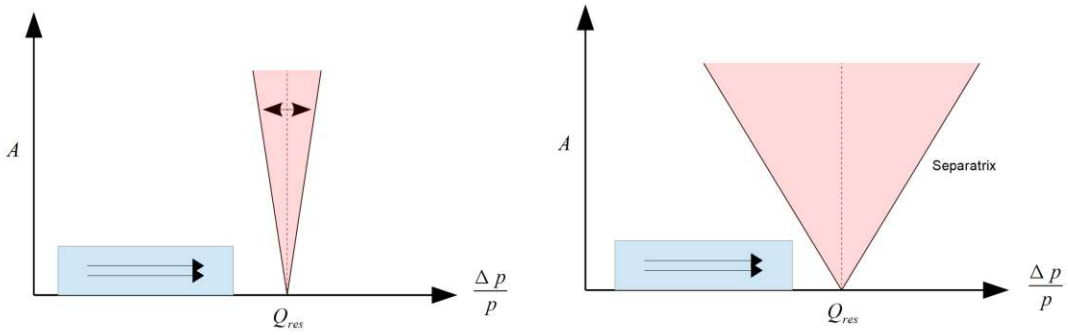

(a) Ramping the sextupole (b) After ramping of the sextupole

Figure 2.6.: The widening of the unstable region (red) in a Steinbach diagram - the so called *separatrices* separate the stable and unstable region.

To extract the beam, it has to be pushed into the unstable region by either changing its momentum offset (fig. 2.8) or increasing its amplitude (fig. 2.9). The respective extraction methods are called *Betatron Core Extraction* and *Radio Frequency Knockout (RFKO) Extraction* and will be discussed in the following sections.

Betatron Core Extraction

A Betatron core is a hollow cylindrical magnetic core wrapped by a coil. A schematic of a betatron core is pictured in fig. 2.7. A current in the coil will induce a magnetic field along the core and in turn an electric field (E) in the center of the torus, where the vacuum tube of the synchrotron's storage ring is located. The electric field can now be used to accelerate particles going through the core, causing the momentum of the circulating beam to shift into the unstable area. Fig. 2.8 shows this process in a Steinbach diagram.

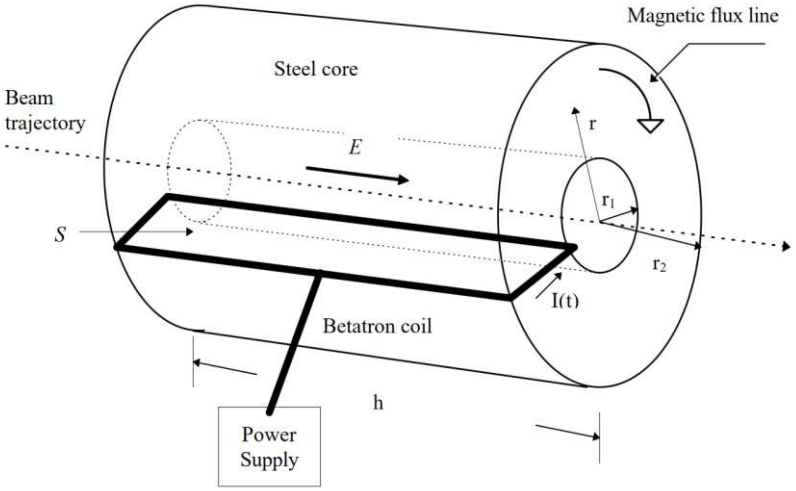

Figure 2.7.: This schematic of a Betatron Core shows an alternate current I(t) in the loop S inducing an alternating magnetic field in the core, which in turn induces an electric field (E) in the direction of the beam's trajectory [13].

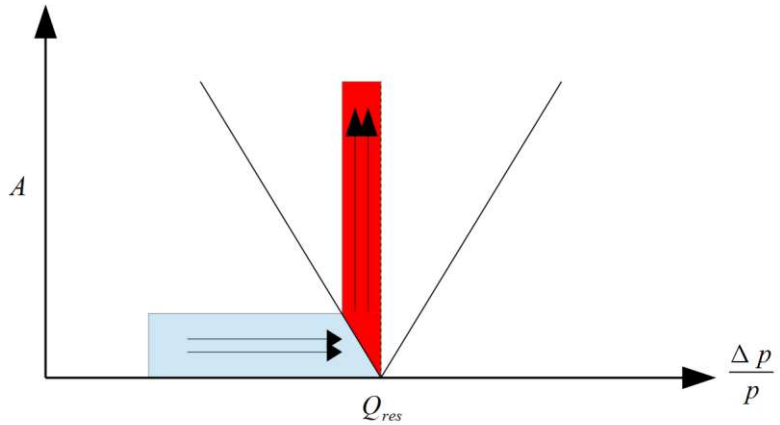

Figure 2.8.: In the betatron core extraction the beam is shifted into the unstable region by the betatron core and subsequently extracted.

RFKO Extraction

With the RFKO method, the beam is extracted by increasing its amplitude with a kicker element near a third order resonance. Such a kicker is fed with an alternate current matching the revolution frequency f_{rev} of the beam (usually in the MHz range) multiplied with the harmonics of the tune. The kicker frequency f_0 is given by [14]

$$f_0 = (n \pm q_x) f_{\text{rev}}, \tag{2.12}$$

where $n \in \mathbb{N}$ and q_x is the fractional part of the tune, meaning for instance a fractional tune of $q_x = 0.666$ for a tune of $Q_x = 1.666$. However, it has to be taken into account, that the beam is not monochromatic in momentum, meaning that the kicker frequency has to be adjusted in order to excite all particles of the bunch in the same way. The frequency modulation is given by [15]

$$f(t) = f_0 \frac{1}{2\pi} \frac{d\phi(t)}{dt}, \tag{2.13}$$

where $\phi(t)$ is a time dependent phase shift of the modulation signal, which has to be chosen in a way, that $f(t)$ matches the frequency/momentum distribution of the beam. The Steinbach diagram of an RFKO extraction can be seen in fig. 2.9. In contrast to the betatron core extraction, the waiting beam is not moved towards the resonance, but rather excited up into it.

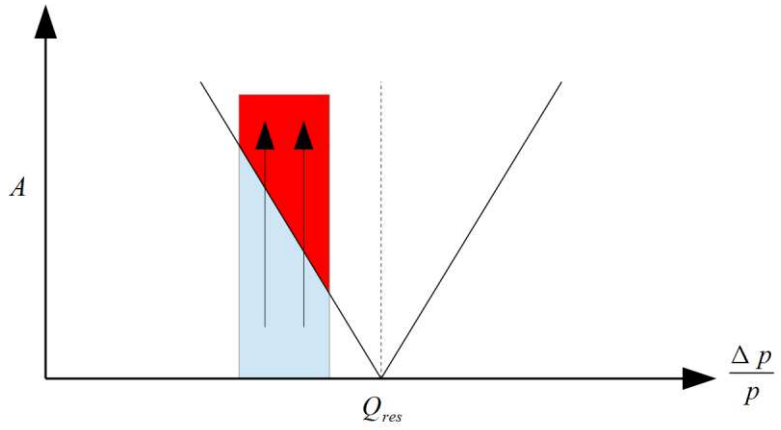

Figure 2.9.: In the RFKO extraction the beam's amplitude is increased into the unstable region by the RF and subsequently extracted.

2.3. Detector Basics

In the following section, the basics of the used sensors shall be discussed shortly. This will include the *Hall effect* for measuring magnetic fields and the functionality of the *ionization chamber*, that is used to measure deposited dose.

2.3.1. The Hall Effect

Charged particles running as a current in a conductor are still susceptible to a Lorentz force induced by a magnetic field and can be displaced in a way, that electrostatic polarization can occur perpendicular to the particles velocity. In fig. 2.10 the voltage U is applied along a plate, inducing the current I_H with electrons travelling at the velocity v [16]. A magnetic Field B pointing into the image plane causes a Lorentz force F_L on the electrons perpendicular to v and B. The resulting electron drift polarizes the plate parallel to F_L, which results in an electric field and a corresponding electric force F_{el} on the electrons, that is in equilibrium with the Lorentz force F_L. This polarization can be measured as the *Hall Voltage* U_H and calculated via

$$F_L = F_{el}, \tag{2.14}$$

$$vB = \frac{U_H}{b}, \tag{2.15}$$

$$\frac{j_H}{nq}B = \frac{U_H}{b}, \tag{2.16}$$

$$U_H = \frac{I_H B}{nqd} = A_H \frac{I_H B}{d}, \tag{2.17}$$

using

$$j_H = nqv, \tag{2.18}$$

$$I_H = j_H bd, \tag{2.19}$$

and the definition for the material specific *Hall constant*

$$A_H = \frac{1}{nq}, \tag{2.20}$$

where nq is the number and charge of electrons in I_H. Plates like the one shown in fig. 2.10 are built into sensors called *Hall Probes*, which can be used to precisely measure magnetic fields.

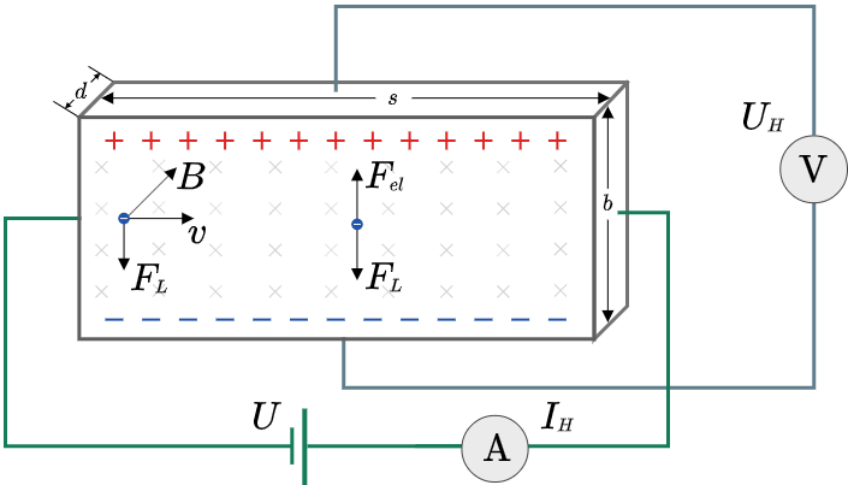

Figure 2.10.: The magnetic field B is causing the Lorentz force F_L on the electrons in the current I_H with the velocity v. The resulting polarization causes the Hall voltage U_H[17].

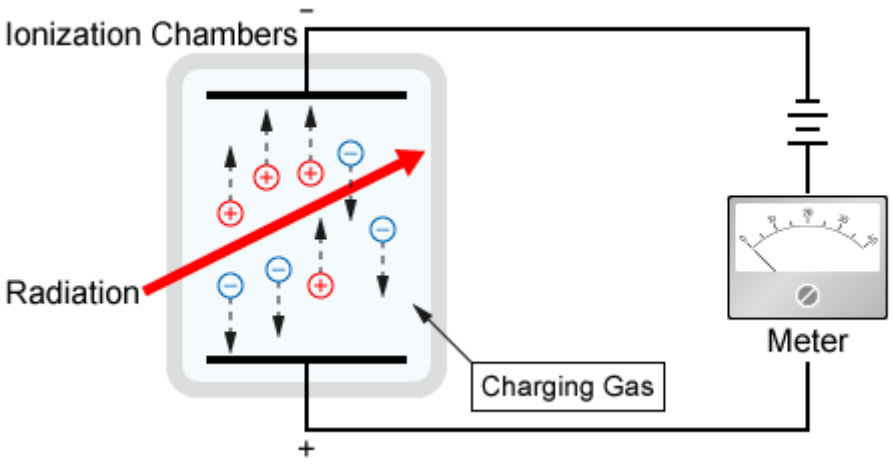

Figure 2.11.: Particles hitting the charging gas in the chamber are ionizing gas atoms, resulting in those ions being accelerated towards the anode or cathode, depending on their charge[18].

2.3.2. The Ionization Chamber

An ionization chamber is a detector for measuring the deposited dose of incoming ionizing radiation [19]. Its basic structure is that of a plate capacitor inside of a chamber filled with a gas, like air or neon, as seen in fig. 2.11. This gas is ionized by incoming radiation, leaving electron ion pairs, which are then accelerated towards anode or cathode. The resulting voltage signal is read out and used to infer the deposited dose in the chamber.

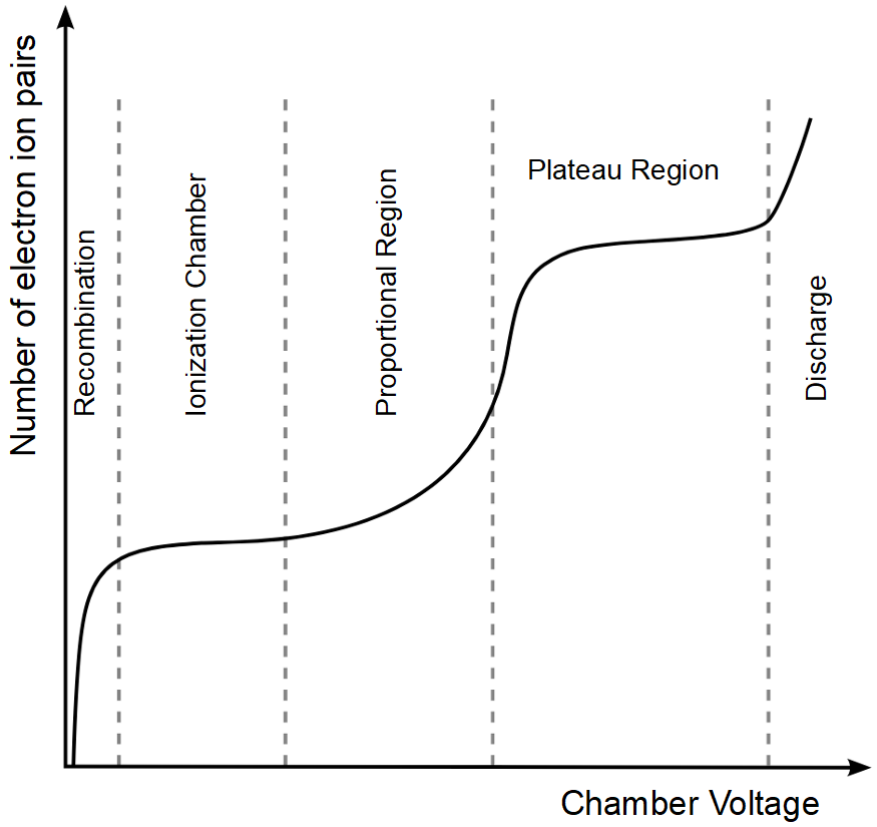

Figure 2.12.: Particles hitting the charging gas in the chamber are ionizing gas atoms, resulting in those ions being accelerated towards the anode or cathode, depending on their charge[20].

For the ionization chamber to work the voltage between the plates has to be high enough, so that the ions and electrons, created in the gas, are accelerated fast enough to reach them before recombining with each other. If the voltage between the plates is turned up even higher, the output signal will change, as ionized particles will themselves ionize more of the charging gases atoms, causing electron-

and ion avalanches. Fig. 2.12 shows the behaviour of the output signal depending on the chamber voltage. Above the ionization chamber range is the proportional range, where, even though there are already ionization avalanches, the signal is still proportional to the energy of the incoming radiation. Increasing the voltage even further leads to the plateau or *Geiger-Müller* region, where everytime a gas atom is ionized, the whole chamber will discharge at once and will create current impulses of uniform strength. Going beyond the plateau region, the gas will constantly discharge, as the energy in the electric field between the plates is so high, that the field itself will ionize the gas atoms.

3. Materials and Methods

3.1. General Method

The maximal permitted deviation from the intended R_{80} range is given as 0.3 mm in water at MedAustron. The energy verification system (EVS) is set to trigger an *interlock* at this offset, meaning a dumping of the beam in the HEBT beam dump. Unfortunately the value to trigger the interlock can't be the beam penetration depth itself, since a range measurement is destructive in nature and the EVS is a safety mechanism for patient treatment, during which the beam needs to be intact. For this reason, two other parameters proportional to the particle energy - and thus the range - are chosen as trigger values, namely the revolution frequency of particles in the main ring, also called RFC frequency and the dipole magnet current. Even though these can be calculated for any given energy (see sec. 3.1.1), since a synchrotron particle accelerator is a complex machine with many potential sources causing an alteration of these results, the need for an experimental validation of these model values arises. The fundamental idea for validation is to perform range measurements in water for a certain penetration depth R as well as for $R\pm0.3$ mm and subsequently comparing them to the respective simultaneously measured RFC frequency and dipole magnet current values at extraction. This, however, is not feasible, since the penetration depths are not a priori known in practice and even if they were, the minimal beam energy resolution of 0.1 MeV is too imprecise for an exact penetration depth offset of ±0.3mm around the design energy in water. To solve this problem, a chosen base energy and some adjacent energies (eg. $E_{\text{base}}\pm$ 0.1 MeV) are measured, and then interpolated via linear fit, to find the energy values for ±0.3 mm. Using the same method for the RFC frequency and B-field measurements and comparing them to the energy values yields the desired EVS trigger values. This comparison, or translation method, can be seen in fig. 3.1. Here, each orange dot represents a measurement. Multiple measurements allow for a linear fit between the dots which makes it possible to determine the shift energy it would take, to cause a certain range shift and vice versa. This can of course also be done with RFC frequency and B-field measurements, which means that one can now calculate the energy shift needed to offset the particle range by 0.3 mm and furthermore calculate the frequency or B-field offset caused by that same energy shift. Thus, the needed values for the EVS trigger parameters can be

determined via experiment.

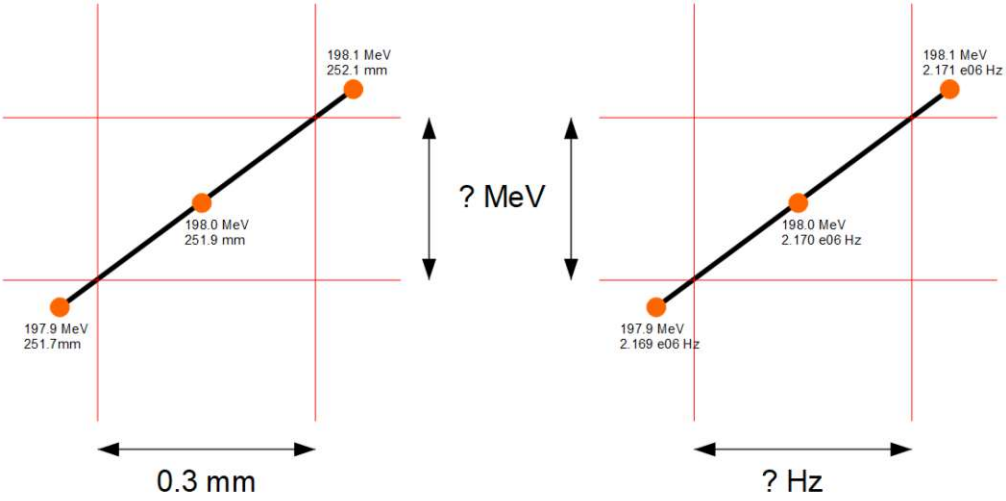

(a) Range ⟶ RFC frequency

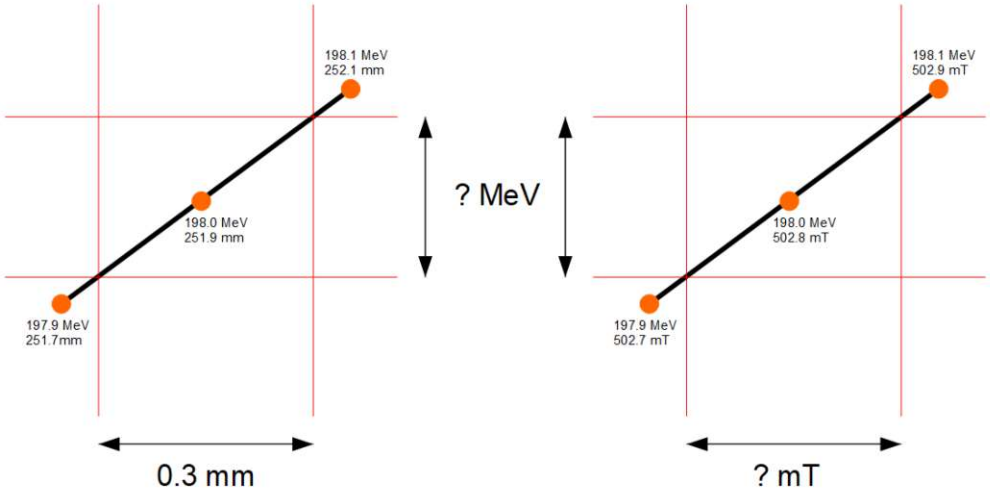

(b) Range ⟶ Magnetic field

Figure 3.1.: Simultaneous measurements of range, frequency and B-field allows for a "translation" first from range to energy and then from energy to either frequency (a) or magnetic field (b).

The goal of this thesis is to derive an accurate model for absolute and relative particle range, RFC frequencies and B-fields and validate it with measurements. Additionally, the measurements shall be used to give an estimation for false posi-

tives, meaning spills, that are within the safety regulations but would be detected as unsafe by the EVS, resulting in an interlock of the machine. A 0.3 mm limit outside of 5σ (1 in 1744278 spills) or around 1 false positive a year would be considered manageable.

3.1.1. Mathematical Model

In the following, the mathematical model, used for calculating absolute and relative particle ranges, RFC frequencies and B-fields, as well as necessary correction shall be described.

Particle Range

For an accurate energy-range model, a polynomial of the 4^{th} order in the form of eq. (2.8) order is fitted over the TOPAS simulations (see sec. 3.2). To not confuse the kinetic particle energy with total energy in further sections, kinetic energy shall be represented by T, making eq. (2.8)

$$R(T) = a_0 + a_1 T + a_2 T^2 + a_3 T^3 + a_4 T^4. \tag{3.1}$$

Magnetic Field

The magnetic field of the dipole magnets for a certain particle and energy is given by [8]

$$B = \gamma A E_0 \frac{v}{q\rho} = \frac{\beta\gamma A E_0 c}{Ze\rho}, \tag{3.2}$$

where

B = Magnetic field of the bending magnets
E_0 = Resting energy of a nucleon
A = Atomic weight of the particle
Z = Atomic number of the particle
v = The particle's velocity
q = The particle's charge
e = Elementary charge
c = Speed of light
ρ = Bending radius of the dipole magnets

With

$$\gamma = \frac{T}{E_0 c^2} + 1, \tag{3.3}$$

$$\beta = \sqrt{1 - \frac{1}{\gamma^2}} \tag{3.4}$$

Eq. (3.2) can be written as

$$B = \frac{A}{Z}\frac{\sqrt{T^2 + 2TE_0c^2}}{e\rho c}. \tag{3.5}$$

If energies and masses are both given in MeV it is useful to write eq. (3.5) as

$$B = \frac{A}{Z}\frac{\sqrt{T^2 + 2TE_0}}{\rho c} \cdot 10^6. \tag{3.6}$$

Particle Frequency

For the circular frequency of the particles in the ring the simple consideration

$$f = \frac{v}{l} = \frac{\beta c}{l}, \tag{3.7}$$

where l is the synchrotron circumference, can be modified for inputs of the particles mass and kinetic energy by using eq. (3.4) and eq. (3.3)

$$f = \frac{c}{l}\frac{\sqrt{T^2 + 2TE_0c^2}}{T + E_0c^2}, \tag{3.8}$$

which like eq. (3.6) is useful to write for given values in MeV as

$$f = \frac{c}{l}\frac{\sqrt{T^2 + 2TE_0}}{T + E_0}. \tag{3.9}$$

From eq. (3.6), eq. (3.9) and the ranges acquired by eq. (2.8) the maximally permissible deviations Δf and ΔB can be easily derived by

$$\Delta f = f(T(R)) - f(T(R - R_{\max})), \tag{3.10}$$

$$\Delta B = B(T(R)) - B(T(R - R_{\max})), \tag{3.11}$$

$$\Delta T = T(R) - T(R - R_{\max}). \tag{3.12}$$

Since $T(R - R_{\max})$ is the inverse of a polynomial of the 4^{th} order, which can be difficult to solve analytically, it is obtained numerically with the python package `scipy.optimize.fsolve`, specifically designed to find the roots of a function [21].

Off momentum corrections at MedAustron

The RFKO extraction method at MedAustron is still experimental, while betatron core extractions are established, time tested and regularly used for particle therapy. As a consequence, already existing energy settings are named for betatron core extractions and extraction energies are defined to values after the acceleration by the betatron core (sec. 2.2.2). This means that choosing a different extraction method may extract the beam at different energies. Specifically for the RFKO extraction, particles will be extracted at lower energies, as they are not accerlerated by the betatron core, but rather kicked out of the main ring. This will be visible in range- but also in the particles plateau revolution frequency, since without the acceleration, the particle velocity will be slower and hence the revolution frequency will be lower as well. The B-field measurements, however, will not be affected as the magnetic field remains constant throughout the betatron core extraction.

In mathematical terms, this means

$$R = R(T - \Delta T) \qquad f = f(T - \Delta T) \qquad B = B(T). \tag{3.13}$$

The according energy offset ΔT can be calculated by [22]

$$\frac{\Delta p}{p} = -\frac{\Delta x}{D_x}, \tag{3.14}$$

$$\frac{\Delta T}{T} = \left(1 + \frac{1}{\gamma}\right) \frac{\Delta p}{p}. \tag{3.15}$$

The measurements for this thesis were conducted at a spatial offset from the design path of $\Delta x = 17\text{mm}$ with the horizontal dispersion at the used pick up being $D_x = 8600\text{mm}$. These values can be integrated either into the model or the measurements to ensure an accurate comparison. However, even though the integration into the model would yield the same relative values as the integration into the measurements, changing the model would result in wrong particle energy values. Thus in this thesis, the resulting mismatch will be compensated by assigning range- and RFC frequency measurements their off momentum energies, while B-field measurements will remain with the respective on momentum energies.

3.2. Dose Depth Simulations with TOPAS

The *Tool for particle simulations* (TOPAS) [23] is a particle simulation software, based on the *GEANT 4 Monte Carlo Toolkit* [24], specialized for proton and ion therapy applications in radiation oncology. The input is simplified to make it more accessible for people planning medical treatment and are not working in the field of particle physics. Instead of GEANT 4 macros, TOPAS uses an intuitive parameter system to set beam and target variables, simulated effects and output options.

Simulated proton energies [MeV]						
-0.5	**-0.2**	**-0.1**	**Base**	**+0.1**	**+0.2**	**+0.5**
61.9	62.2	62.3	**62.4**	62.5	62.6	62.9
95.8	96.1	96.2	**96.3**	96.4	96.5	96.8
129.7	130.0	130.1	**130.2**	130.3	130.4	130.7
197.5	197.8	197.9	**198.0**	198.1	198.2	198.5
252.2	252.5	252.6	**252.7**	252.8	252.9	253.2

(a) Protons

Simulated carbon ion energies [MeV/u]						
-0.5	**-0.2**	**-0.1**	**Base**	**+0.1**	**+0.2**	**+0.5**
119.5	119.8	119.9	**120.0**	120.1	120.2	120.5
189.5	189.8	189.9	**190.0**	190.1	190.2	190.5
259.5	259.8	259.9	**260.0**	260.1	260.2	260.5
331.0	331.3	331.4	**331.5**	331.6	331.7	332.0
402.3	402.6	402.7	**402.8**	402.9	403.0	403.3

(b) Carbon ions

Table 3.1.: Simulated proton (a) and carbon ion (b) energies - a base energy and adjacent energies to each base of $\pm 0.5 \pm 0.2 \pm 0.1$ MeV. The adjacent energies are used to calculate the energy dependence of particle range at that base energy in linear approximation.

For this thesis, protons and carbon ions impinging a 0.5m water tank at various kinetic energies were simulated. Per particle type, energy ranges of 1 MeV width at 5 different energy levels were simulated in 7 steps as seen in tab. 3.1. The central of those 7 steps was used as base energy, meaning, that the other 6 surrounding energies were used to calculate the energy dependence of particle range at that base via a linear fit. For each simulation, the deposited dose was recorded for 10^5 particles at 10^4 bins, making the step size 0.05mm. The models used to perform the Monte Carlo simulations for each particle were taken from the GEANT4 physics

list and are listed in table 3.2. Simulation results were printed into a .csv file and were able to be processed like any other range measurements (see sec. 3.4). They were used first and foremost to fit the theoretical range model over the obtained simulated R_{80} values, but also to get a first glimpse into the numbers, that one might expect from later measurements.

GEANT4 Effect Name	**Effect**
`g4em-standard_opt4`	Standard GEANT4 electromagnetic model with more detailed low energy proton collisions
`g4h-phy_QGSP_BIC_HP`	Hadronic elastic, inelastic and capture processes
`g4decay`	Decay of excited particles
`g4ion-binarycascade`	Collision Cascades
`g4h-elastic_HP`	More precise hadronic elastic scattering
`g4stopping`	Stopping power model

Table 3.2.: Used GEANT4 simulation lists [25].

3.3. Measurements

3.3.1. Measurement Devices

Before laying out the measurement procedures conducted for this project, a short introduction to the measurement devices themselves shall be given. Since the RFC measurements are taken from the cavity itself which also provides the RF signal, this aspect does not need further investigation. However, the devices used to measure particle penetration depth and the magnetic field of dipole magnets, namely the PTW Peakfinder and the SENIS I1A Hall Probe will be described briefly.

The Peakfinder

The PTW Peakfinder [26] is a device dedicated to measure the depth of a particle beam's Bragg peak in water. In essence it consists of a water filled tube and two air filled ionization chambers - the stationary *reference chamber* (PTW 34082) (RC) and the movable *field chamber* (PTW 34080) (FC). The position of the FC is adjustable via a servo control unit, which can be controlled and automatically changed by the PTW PeakScan Software. A schematic of the peakfinder can be seen in fig. 3.2.

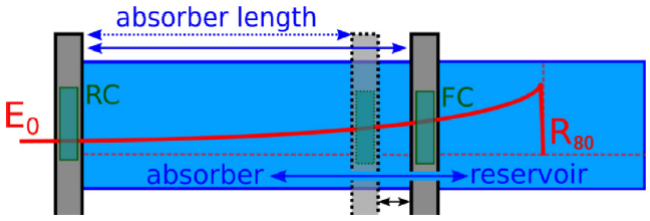

Figure 3.2.: Schematic of the peakfinder: The FC moves towards the estimated location of the bragg peak and is indirectly measuring energy deposited into the water column [27].

The peak's profile is obtained by measuring the dose deposition at adjustable intervals (stepsize $\geq 10\mu m$) in the assigned ranges. Obviously, the deposited dose in water can only be obtained indirectly by a well known conversion factor from air to water, as the dose can only be measured inside the ionization chamber. Measurement time at a certain point can be determined either by trigger, accumulated charge in the RC, or direct input of the desired time interval. For the purposes of this thesis, the accumulated charge condition seemed the most practical, since the

absence of particles between spills is not a relevant factor this way. Subsequently, it was used for all measurements.

The Hall Probe

A hall probe is a device for measuring stationary magnetic fields. It is based on the hall effect, where a magnetic field will deflect a current flowing horizontally through a conducting plate, thus inducing a vertical voltage in the plate. A schematic of the SENIS I1A hall probe used for this project can be seen in fig. 3.3.

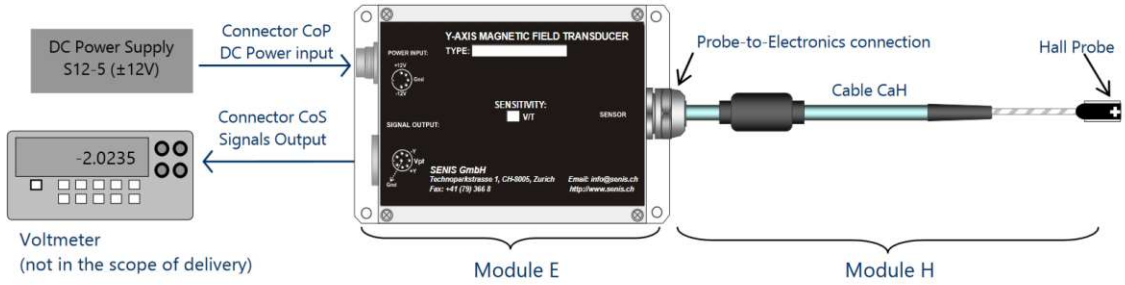

Figure 3.3.: Schematic of the SENIS I1A Hall Probe with Module H referring to the integrated hall probe and Module E to the electronics part [28].

The sensitivity of the probe is given as 5 V/T, which along with a conditioning factor from the acquisition system of 10:1 leads to a conversion factor of 2000 from the measured voltage to mT.

3.3.2. Measurments Procedure

Lower Energy [MeV]	Base Energy [MeV]	Higher Energy [MeV]
	62.4	62.7
197.8	198.0	198.2

(a) Measured proton energies

Lower Energy [MeV/n]	Base Energy [MeV/n]	Higher Energy [MeV/n]
	120.0	120.6
399.9	400.1	400.3

(b) Measured carbon ion energies per nucleon

Table 3.3.: Measured proton(a) and carbon ion(b) energies per nucleon.

Range, RFC-frequency and dipole B-field were measured simultaneously for two base energies - a high and a low one - per particle type with either one or two adjacent energies per base energy. Unfortunately, it was not possible to get measurements below the low base energy, hence the two low energy measurements are only accompanied by one adjacent energy. Regardless, at least 2 runs were recorded per energy, to get some statistical analysis. Table 3.3 shows all measured energies for both proton and carbon ions. While the RFC frequency can be taken from the cavity itself, the magnetic field was measured by a hall probe located in one of the dipole magnets. Range measurements were performed using the PTW Peakfinder (sec. 3.3.1) in MedAustron's Irradiation Room 1 as seen in fig. 3.4. The peakfinder was operated in "accumulated charge" mode with a RC charge of 10 nC, which provided a high level of accuracy, while keeping the measurement time reasonable. At the measured energies, this charge setting turned out to yield around 1 measured step per spill, making a 25 step run 20-30 spills and about 5-10 min long.

The output for each simultaneous measurement was:

- A text file containing measured depths and corresponding dose in the peakfinder
- A .msr formatted text file for each spill containing the RFC frequency, timing events in the spill cycle ("Start EVS", "Prepare Extraction", etc.) plus the corresponding times for each frequency measurement and timing event

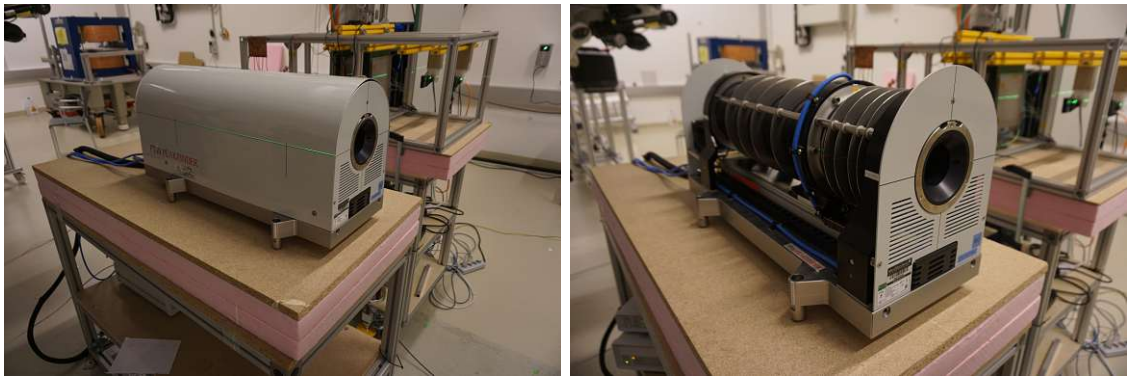

(a) With hood (b) Without hood

Figure 3.4.: The PTW Peakfinder with the hood on and off.

- A text file containing the voltage output of the hall probe at 2kHz for the entire duration of the measurement

3.4. Data Processing

The measured data sets for each energy were processed in three separate scripts and the respective results subsequently brought together with the theory results in a final 'master' script. For RFC frequency and B-field measurements, only data points taken during the extraction, also called the *plateau region* were analyzed. An outline of the processing performed by these scripts shall be given in the following section. For a more detailed description of the used python scripts, see appendix B. Additionally, a full set of sub-results and their analysis is given in appendix A.

3.4.1. Range Measurement Processing

The averaged range measurements were read in and fitted by a gaussian of the form given by

$$I(x) = \frac{a}{2}\left[e^{\frac{t^2 s^2}{2}+t(x-u)}\mathrm{erf}\left(-\frac{u-x}{\sqrt{2}s+\frac{ts}{\sqrt{2}}}\right)\right], \tag{3.16}$$

which yielded excellent results for the R_{80} region, ie. from the first R_{80} to the second one [29]. Fitted curves and original data points were analyzed and compared. For the raw data, the peak was found by just taking the depth of the highest measured dose value, while the R_{80} and R_{20} were determined by the nearest measured point, to were the actual 80% and 20% values of the peak respectively would be located. For the fitted curve, these points could obviously be determined analytically to any degree of precision, with the restriction, that the actual accuracy of those calculated values is limited by the quality of the measurement and the fit itself. An example of this comparison can be seen for the base energy of 198 MeV in tab. 3.4. The raw and fitted data for the base energy 198 MeV plus the adjacent energies 197.8 MeV and 198.2 MeV are plotted in fig. 3.5.
The so found R_{80} values of the fitted curves for a base energy plus the adjacent energies were linearly fitted over their respective energies as described in sec 3.1. Note that, since with RFKO the beam is extracted off-momentum, the actual energy values will be lower for range and RFC measurements. Finally the 0.3mm, 0.5mm and 1mm offsets from the base energy are calculated from the linear fit and are stored alongside the fit parameters of the linear fit. An example for the linear fit analysis is shown in tab. 3.5 and plotted in fig. 3.6.

Peakfinder Measurement Proton 198.0 MeV				
Raw Data				
Peak	249.4	mm	3.687	Gy
R80	251.9	mm	2.950	Gy
R20	255.4	mm	0.737	Gy
R80 width	6.5	mm		
Penumbra width	3.5	mm		
Fitted Data				
Peak	249.40	mm	3.686	Gy
R80_f	251.97	mm	2.949	Gy
R20	255.55	mm	0.737	Gy
R80 width	6.26	mm		
Penumbra width	3.58	mm		
Uncertainty	0.091	mm		
Difference Raw-Fitted Data				
Peak	0.00	mm	0.0013	Gy
R80	0.07	mm	0.0010	Gy
R20	0.15	mm	0.0002	Gy
R80 width	0.24	mm		
Penumbra width	0.08	mm		
R^2	0.999366			

Table 3.4.: Example for the analysis of measured 198 MeV data points.

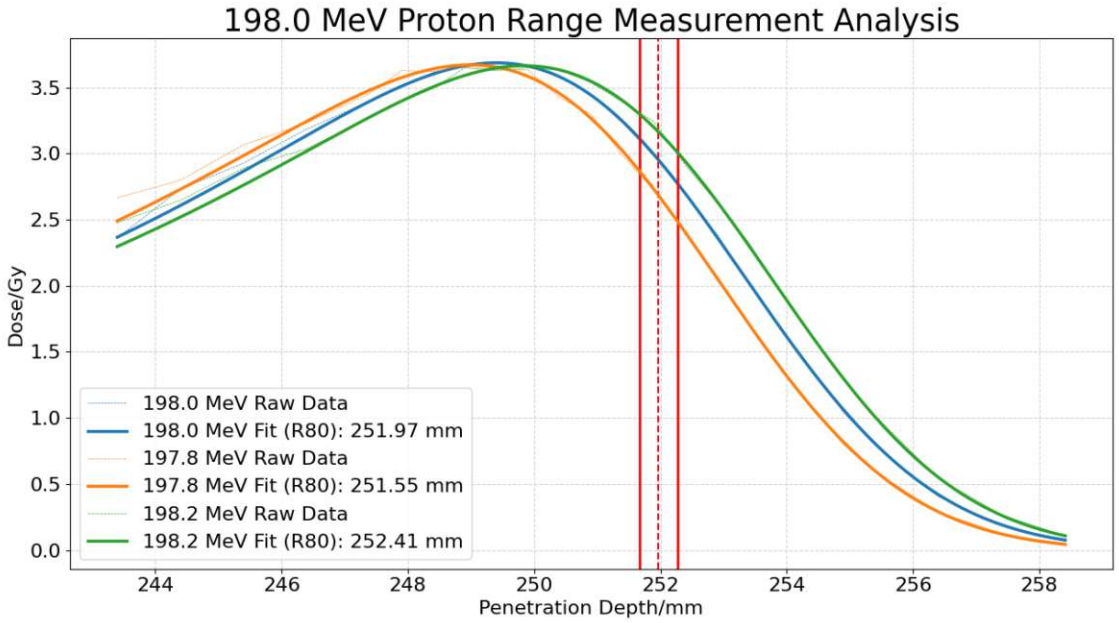

Figure 3.5.: Example for fitted Peakfinder curves at 198.0 ±0.2 MeV.

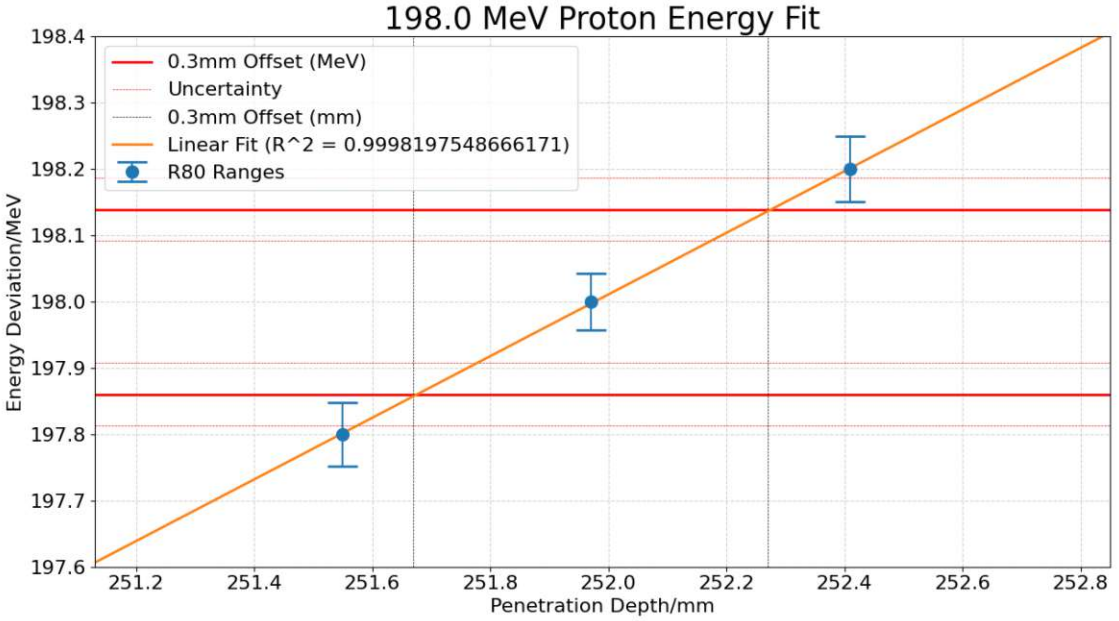

Figure 3.6.: Example for the linear fit of Peakfinder curves at 198.0 ±0.2 MeV.

Linear Fit Proton 198.0 ± 0.2 MeV		
Fit Parameters		
k	0.465032	
d	80.822675	
Energy Offset for Range Deviation		
0.3mm	0.1395	MeV
0.5mm	0.2325	MeV
1mm	0.4650	MeV
Standard Deviation	0.0468	MeV
Range Offset for 0.1 MeV Energy Deviation		
Range Offset	0.2150	mm
R^2	0.999820	

Table 3.5.: Example for linear fit analysis of fitted Peakfinder curves at 198.0 ±0.2 MeV.

3.4.2. RFC Frequency Measurement Processing

For RFC frequency measurements, each spill has its own text file, recording the ramping process. Since the frequency is held constant for the entire duration of the extraction, practically, the most commonly measured frequency in each file can be taken as the plateau frequency. The distribution of most common frequency values per spill can be seen in depicted as a boxplot and a histogram in fig. 3.7. An additional plot showing consecutive spills is shown in fig. 3.8. The 0.3 mm limits in MeV, calculated by the peakfinder measurement analysis described above, are also depicted in all 3 plots.
Taking the median of all plateau frequencies for base and adjacent energies, the 0.3mm, 0.5mm and 1mm offsets for frequency can be calculated using a linear fit and the range offsets in energy acquired by the range measurement analysis conducted beforehand (see fig. 3.1). An example for the frequency analysis for 197.8 MeV, 198.0 MeV and 198.2 MeV, alongside the linear fit parameters can be seen in tab. 3.6. Additionally, the linear fit is visualized in fig. 3.9.

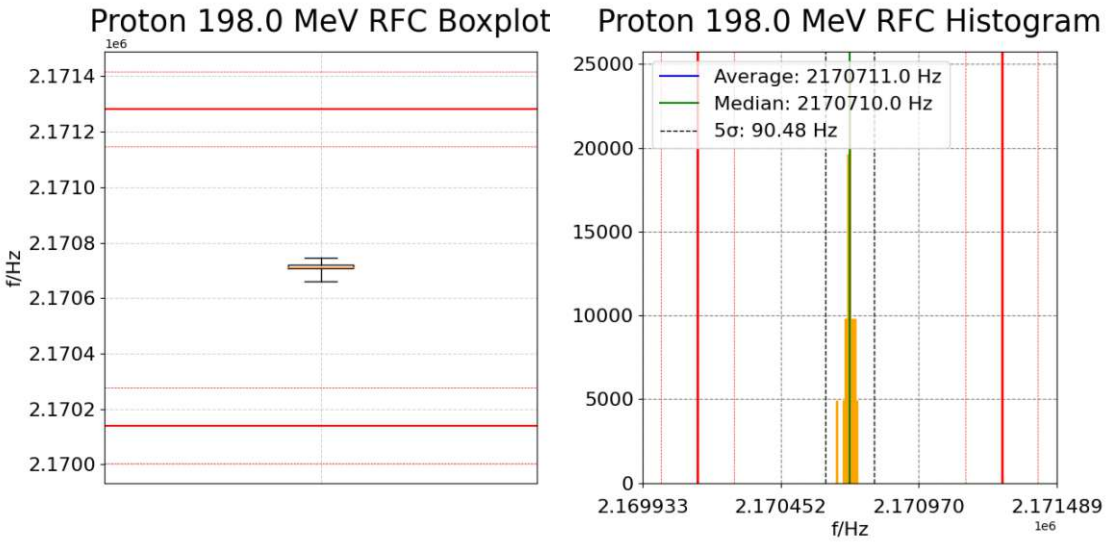

Figure 3.7.: Proton 198 MeV RFC Frequency Boxplot & Histogram with 0.3 mm limits indicated by the red lines.

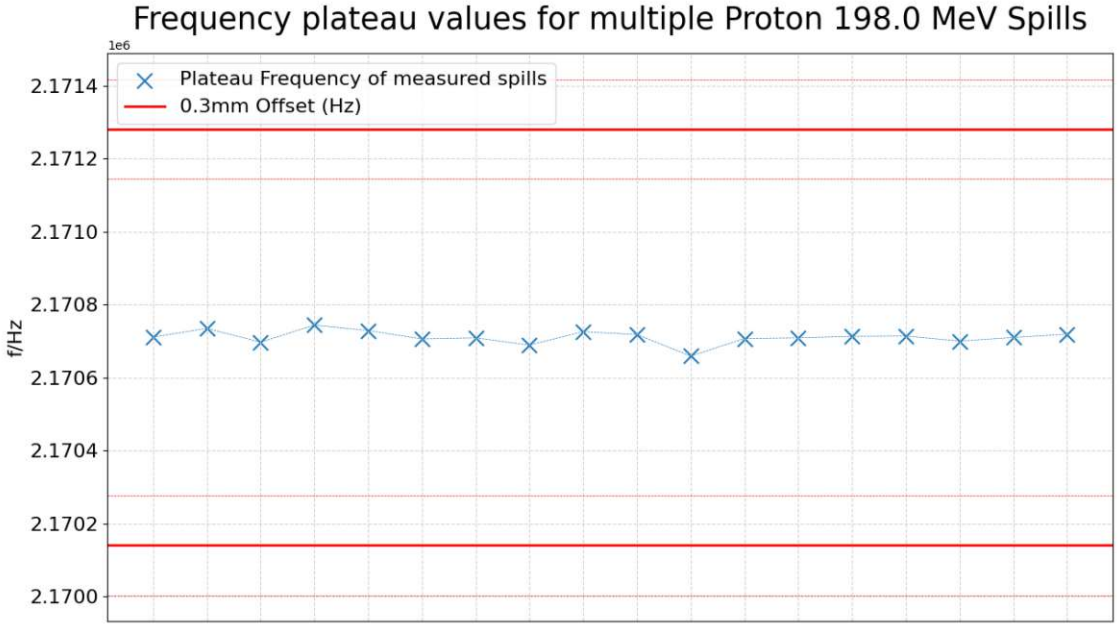

Figure 3.8.: Proton 198 MeV measured RFC Frequency spill-plateaus with 0.3 mm limits indicated by the red lines.

RFC Measurements Proton 198.0 ± 0.2 MeV		
Proton 197.8 MeV RFC Measurement		
Mean	2169877.28	Hz
Median	2169875.00	Hz
Standard Deviation	19.90	Hz
Proton 198.0 MeV RFC Measurement		
Mean	2170710.83	Hz
Median	2170710.50	Hz
Standard Deviation	18.09	Hz
Proton 198.2 MeV RFC Measurement		
Mean	2171514.05	Hz
Median	2171517.00	Hz
Standard Deviation	18.22	Hz
Fit Parameters		
k	0.000244	
d	-332.421480	
RFC Frequency Offset for Range Deviation		
0.3mm	570.93	Hz
0.5mm	951.55	Hz
1mm	1903.10	Hz
Standard Deviation	136.31	Hz
R^2	0.999886	

Table 3.6.: Example for the analysis of measured revolution frequencies, plus linear fit.

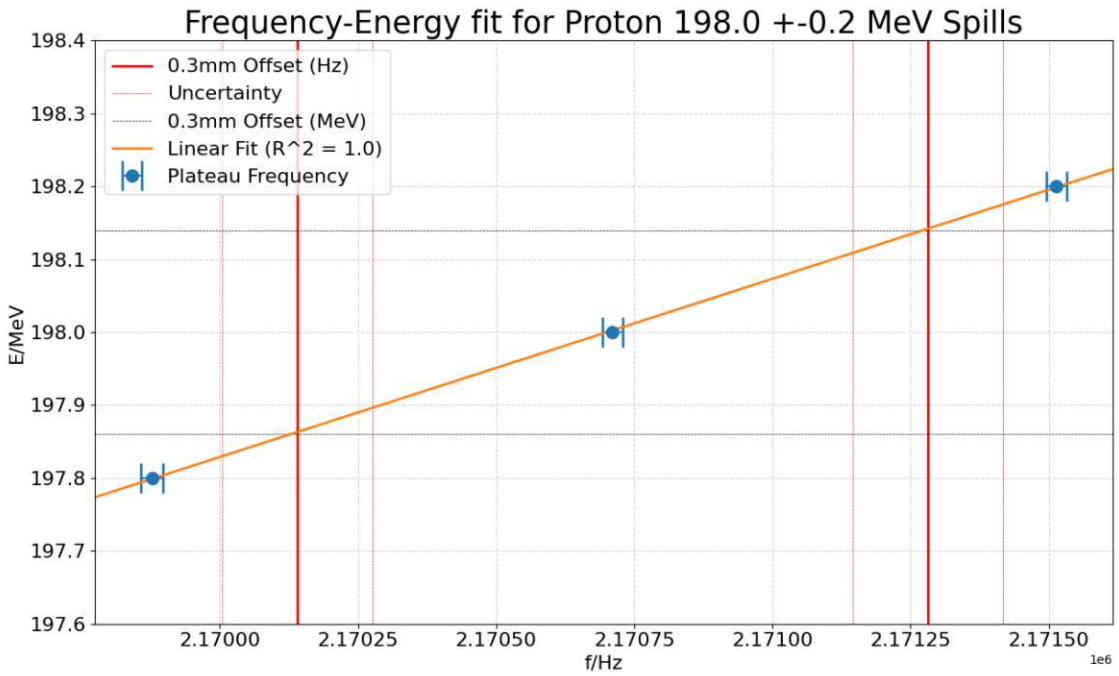

Figure 3.9.: Example for the linear fit of proton RFC measurements.

3.4.3. B-Field Measurement Processing

Lastly, for analyzing the B-field, a change of 1mV in measured hall probe voltage, due to the ramping of the dipoles was correlated with the "Start Cycle" timing event from the framework and thus correlated with all subsequent timing events. The uncertainty of the first correlation is around 20 measurement samples or 10ms, which is negligible, because the measurement of the plateau was not started until the "Start Extraction" event, at which point the B-field has plateaued for well over a second. Data points were taken for 10 seconds and the median for base and adjacent energies processed in the same way as the frequency measurements, to get the B-field offsets. Fig. 3.10 shows all measured B-field values for multiple spills of 198 MeV proton measurements in a boxplot, and a histogram. Additionally, fig. 3.11 shows all B-field values over the duration of a spill's plateau, while Fig. 3.12 visualizes the plateau duration of a measured spill. As before with the RFC chart, the calculated 0.3 mm limits from Peakfinder measurement analysis are shown in the plots. An example for the B-field measurement analysis and linear fitting can be seen in tab. 3.7 and the fitting is visualized in fig. 3.13.

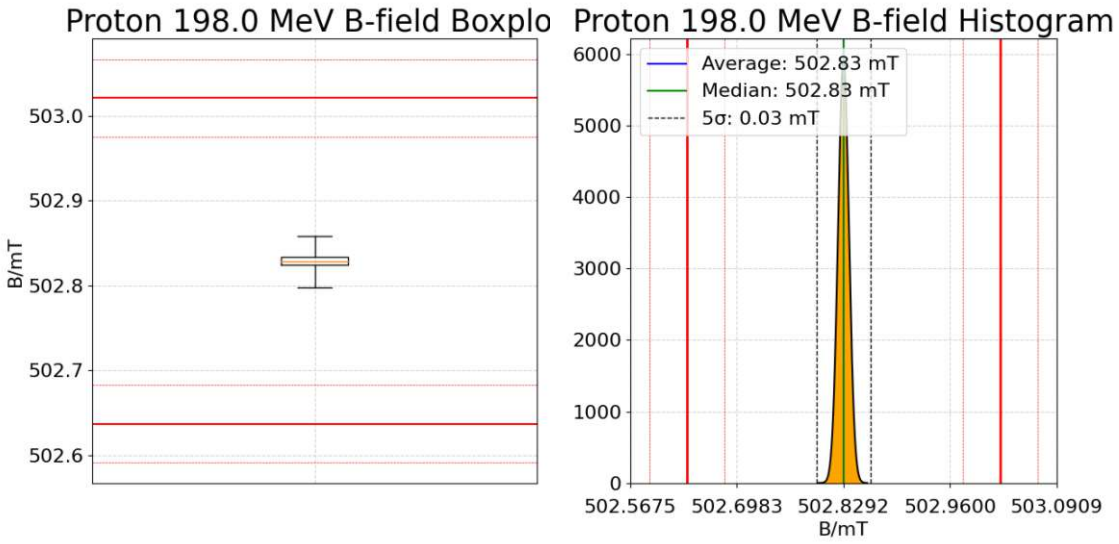

Figure 3.10.: Proton 198 MeV B-field Boxplot & Histogram with 0.3 mm limits indicated by the red lines.

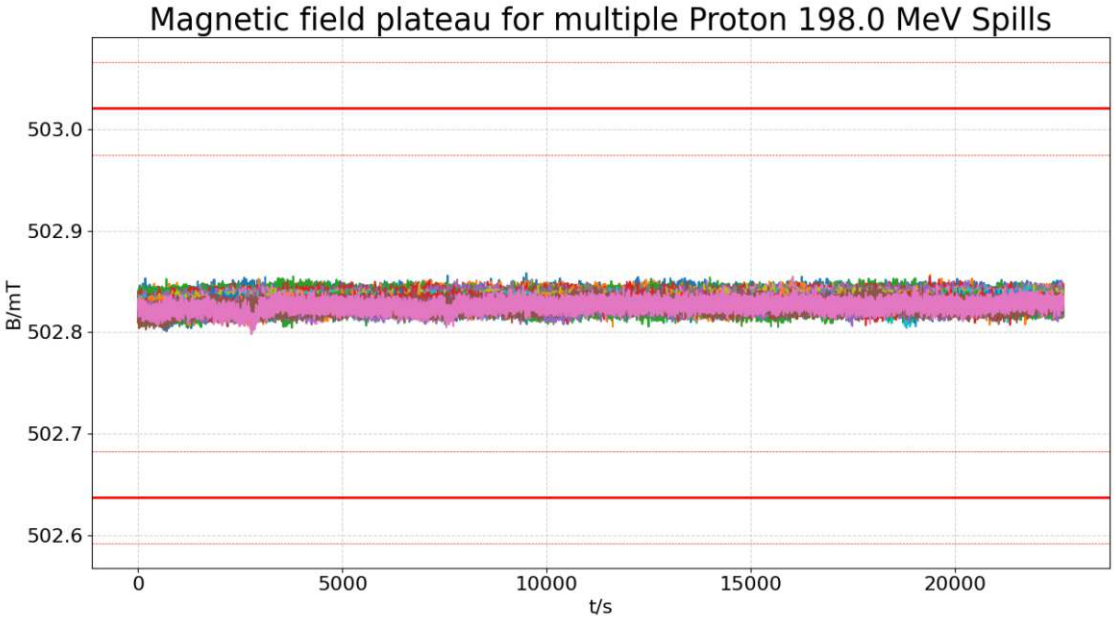

Figure 3.11.: Proton 198 MeV measured B-field spill-plateaus with 0.3 mm limits indicated by the red lines.

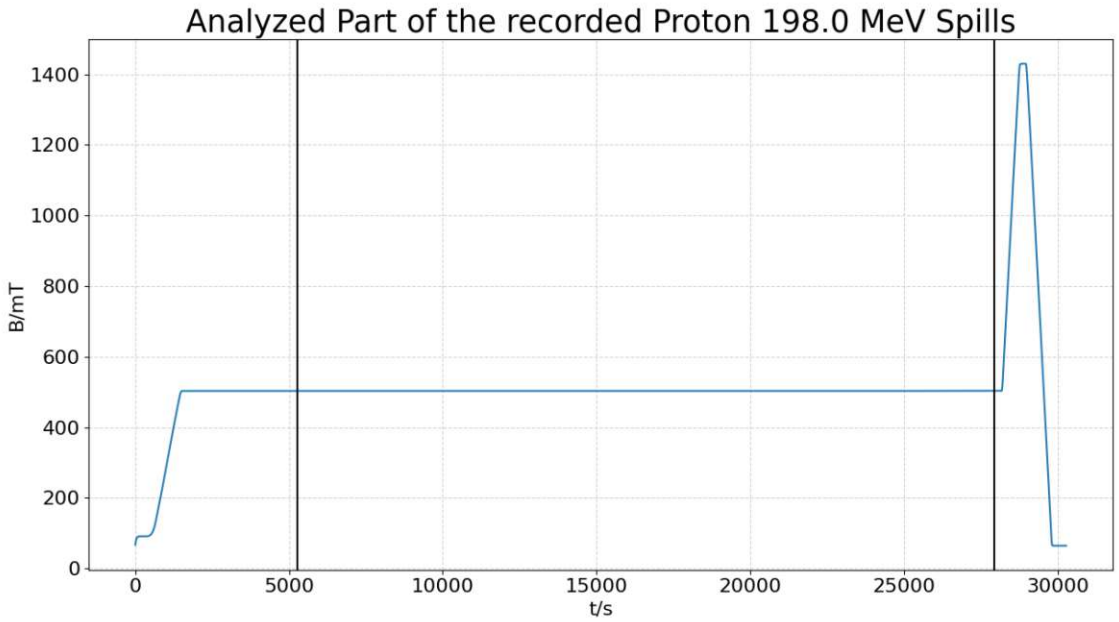

Figure 3.12.: Proton 198 MeV analyzed part of the spill in measured B-field.

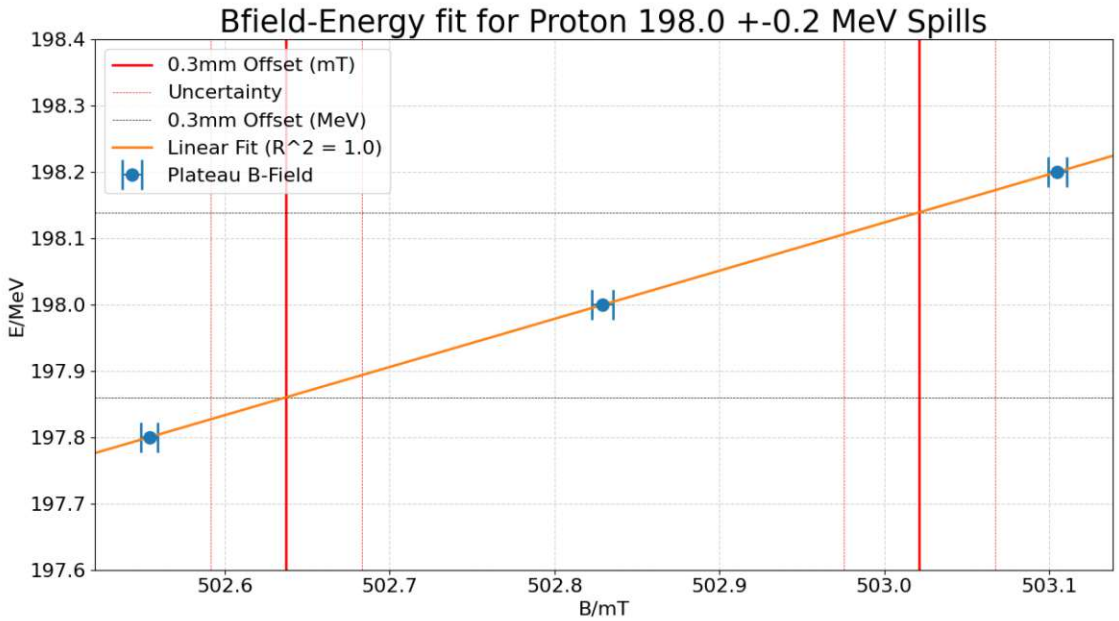

Figure 3.13.: Example for proton B-field measurement analysis.

B-field Measurements Proton 198.0 ± 0.2 MeV		
Proton 197.8 MeV B-field Measurement		
Mean	502.554	mT
Median	502.554	mT
Standard Deviation	0.0051	mT
Proton 198.0 MeV B-field Measurement		
Mean	502.829	mT
Median	502.829	mT
Standard Deviation	0.0066	mT
Proton 198.2 MeV B-field Measurement		
Mean	503.104	mT
Median	503.104	mT
Standard Deviation	0.0056	mT
Fit Parameters		
k	0.726386	
d	-167.248088	
RFC Frequency Offset for Range Deviation		
0.3mm	0.192	mT
0.5mm	0.320	mT
1mm	0.640	mT
Standard Deviation	0.0458	mT
R^2	0.999999	

Table 3.7.: Example for the analysis of measured magnetic dipole fields, plus linear fit.

3.4.4. Uncertainty Calculation

Additionally, error ranges were created by calculating the respective standard deviations with [30]

$$\sigma_x = \frac{1}{n}\sum_n \sqrt{(\overline{x} - x_i)^2} \tag{3.17}$$

and combining them according to error propagation laws

$$\sigma = \sqrt{\sigma_1^2 + \sigma_2^2}, \tag{3.18}$$

$$\sigma(y) = \sqrt{\left(\frac{dx}{dy}\right)^2 \sigma(x)}. \tag{3.19}$$

Furthermore, it was made use of the fact, that the data processing is mostly linearized, meaning eq. (3.19) simplifies to

$$\sigma(y) = k\sqrt{\sigma(x)}, \tag{3.20}$$

$$\sigma(x) = \frac{1}{k}\sqrt{\sigma(y)}. \tag{3.21}$$

To get an error bracket for the 0.3 mm limit in Hz or mT, not only have the measurement and fitting uncertainties to be taken into account, but also uncertainties from the range measurements and processing need to be considered. For a correct error assessment, the following steps need to be taken:

- Get the dose uncertainties σ_g(Gy) and σ_{lf}(Gy) of the gaussian and linear fit, respectively, for a range measurement via eq. (3.17) and combine them with eq. (3.18) to σ_{R80}(Gy)
- Use eq. (3.21) and the fact, that the R_{80} sits in the linear region of the curve, to get $\sigma_{R80}(mm)$
- Use the linear fit between range measurements to get σ_{R80}(MeV) and combine all those range uncertainties via eq. (3.18)
- Use the linear fit between either RFC frequency- or B-field- measurements to get σ_{R80}(Hz) or σ_{R80}(mT) respectively
- Combine measured RFC frequency- or B-field- standard deviations with σ_{R80}(Hz) or σ_{R80}(mT) to get a final uncertainty

3.5. Validation Criteria

As already discussed in sec. 3.1, the first goal of this thesis is the confirmation of the model derived in sec. 3.1.1 by the measurements and subsequent analysis described in sec. 3.3.2 and sec. 3.4. The EVS can be seen as validated, if the potential discrepancies between model and measurements are manageable. For instance, if the 0.3 mm limit at a certain energy would be equivalent to 2 kHz in RFC frequency, a discrepancy of 400 Hz or 20% relative error would be manageable, as the trigger condition for the EVS could be set to a tighter limit (at the cost of more potential false positives). Higher discrepancies, like >50%, would still be possible to compensate, but would also call the accuracy of either the model or the measurements into question. Discrepancies of over 100% relative error, would not be tolerable at all. For this evaluation, only the relative values, meaning the 0.3 mm offset values ΔR, Δf and ΔB for all treated energies are used. A perfect agreement between model and measured values in absolute values, meaning R(T), f(T) and B(T), is not as crucial as for relative values, since the model is not used to calculate these for the MedAustron framework. A mismatch in absolute values however, is a strong indicator of potential for improvement, since the relative values are obviously derived from the absolute ones.

The second goal is to determine the probability of a false positive, meaning that the EVS triggers an interlock, even though the beam energy is in the allowed range. Assuming a functional and correctly set EVS, the only possibility of a false interlock is given by the spill-to-spill distribution of RFC frequency and B-field values. Further assuming a gaussian distribution of these values, the probability of a false positive can be calculated by finding the standard deviation σ and checking how many standard deviations are needed to reach the 0.3 mm limit is from the mean of the distribution.

4. Results

In this section, the results of conducted measurements and calculations shall be given and compared with each other. These comparisons will be split into absolute and relative values for each quantity and particle type, the absolute referring to values directly obtained via measurement or calculation, the relative referring to the difference between two absolute values eg. $\Delta T = T(R_1) - T(R_2)$. Specifically, relative values are presented for each measured base energy and three chosen $\Delta R = R_1 - R_2$ values of 0.3 mm, 0.5 mm and 1 mm, in the form

$$\Delta T(T, \Delta R) = T(R(T) - T(R(T) - \Delta R), \tag{4.1}$$

which, for a base energy of 198 MeV and a ΔR of 0.3 mm, would look like

$$\Delta T(198\text{MeV}, 0.3\text{mm}) = 198\text{MeV} - T(R(198\text{MeV}) - 0.3\text{mm}). \tag{4.2}$$

However, only the final results are presented here, as the number of sub-results and respective figures would bloat this chapter unnecessarily. Tables and figures for measurement sub-results including a full description can be found in appendix A.1.
One last important note is, that the particle energy will be referred to as two different values, namely the on- and off-momentum energies. The way this issue will be handled here is, that when referring to the name of a energy measurement setting the on-momentum energy is used, while mentioning a measured or calculated energy value, the off-momentum energy is used. This is because the energy settings at MedAustron are referred to by their on momentum ernergy output, due to the Betatron Core Extraction being the main method used still.

4.1. Simulated Relative Values

The TOPAS simulations not only provided a good first impression at how a 0.3mm range deviation should look in terms of an energy offset, the analyzed bragg curves were also used to determine the parameters of eq.(3.1) for the mathematical model. For each particle type - protons and carbon ions - 35 curves were analyzed and the R_{80} was used as the range variable. The resulting parameters can be seen in tab. 4.1. Note, that these parameters are limited to the fitting ranges for each particle type and can be seen in tab. 3.1.

a_0	a_1	a_2	a_3	a_4
-1.610446	0.123714	7.488812e-03	-9.397654e-06	7.138342e-09

(a) Proton fit parameters

a_0	a_1	a_2	a_3	a_4
10.741378	-0.160543	3.803184e-03	-6.830650e-06	6.109014e-09

(b) Carbon ion fit parameters

Table 4.1.: Fit parameters (to the 6^{th} decimal point) for a polynomial of the 4^{th} order obtained via TOPAS proton and carbon ion dose depth simulations

As mentioned before, the simulated relative range values can also be compared to the calculated relative model values. This is done for 0.3 mm, 0.5 mm and 1 mm range offsets at different energies and can be seen in tab. 4.2, 4.3, 4.4 for protons and in tab. 4.5, 4.6, 4.7 for carbon ions. These simulated values are also visualized in comparison to calculated and measured values in fig. 4.7 and fig. 4.10. The calculation of these range offset values was conducted in the same way as the measured values, as described in sec. 3.4.1.

Simulated vs. Model relative proton energy values for 0.3mm range offset			
Base Energy [MeV]	Model [MeV]	Simulation [MeV]	ΔE [MeV]
62.4	0.314	0.3102	0.0038
96.3	0.2255	0.2212	0.0043
130.2	0.1808	0.1713	0.0095
198.0	0.136	0.1353	0.0008
252.7	0.1168	0.104	0.0128

Table 4.2.: Comparison of calculated and simulated relative proton energy values at 0.3mm range offset

Simulated vs. Model relative proton energy values for 0.5mm range offset			
Base Energy [MeV]	Model [MeV]	Simulation [MeV]	ΔE [MeV]
62.4	0.5233	0.5199	0.0034
96.3	0.3759	0.3708	0.0051
130.2	0.3014	0.2883	0.0131
198.0	0.2267	0.2254	0.0013
252.7	0.1946	0.1806	0.014

Table 4.3.: Comparison of calculated and simulated relative proton energy values at 0.5mm range offset

Simulated vs. Model relative proton energy values for 1mm range offset			
Base Energy [MeV]	Model [MeV]	Simulation [MeV]	ΔE [MeV]
62.4	1.0467	1.0443	0.0024
96.3	0.7518	0.7448	0.007
130.2	0.6028	0.5808	0.022
198.0	0.4534	0.4508	0.0025
252.7	0.3893	0.3722	0.017

Table 4.4.: Comparison of calculated and simulated relative proton energy values at 1mm range offset

Simulated vs. Model relative C-ion energy values for 0.3mm range offset			
Base Energy [MeV]	Model [MeV]	Simulation [MeV]	ΔE [MeV]
120.0	0.6008	0.574	0.0268
190.0	0.421	0.4144	0.0067
260.0	0.3483	0.3246	0.0237
331.5	0.3002	0.3	0.0002
402.8	0.2552	0.2833	0.0281

Table 4.5.: Comparison of calculated and simulated relative C-ion energy values at 0.3mm range offset

Simulated vs. Model relative C-ion energy values for 0.5mm range offset			
Base Energy [MeV]	Model [MeV]	Simulation [MeV]	ΔE [MeV]
120.0	1.0013	0.9513	0.05
190.0	0.7017	0.6933	0.0085
260.0	0.5805	0.5463	0.0342
331.5	0.5004	0.5	0.0004
402.8	0.4253	0.4678	0.0425

Table 4.6.: Comparison of calculated and simulated relative C-ion energy values at 0.5mm range offset

Simulated vs. Model relative C-ion energy values for 1mm range offset			
Base Energy [MeV/u]	Model [MeV]	Simulation [MeV]	ΔE [MeV]
120.0	2.0028	1.8945	0.1083
190.0	1.4035	1.3906	0.0129
260.0	1.161	1.1006	0.0604
331.5	1.0008	1.0	0.0008
402.8	0.8507	0.929	0.0783

Table 4.7.: Comparison of calculated and simulated relative C-ion energy values at 1mm range offset

4.2. Measured Absolute Values

In the following, the absolute values of the performed measurements are presented and compared to the calculated values in tab. 4.8a for 62 MeV protons, tab. 4.8b for 198 MeV protons, tab. 4.9a for 120 MeV carbon ions and tab. 4.9b for 400 MeV carbon ions. Additionally, a comparison for all energies will be plotted against calculated curves in fig. 4.1 for measured proton energies, fig. 4.2 for proton RFC measurements, fig. 4.3 for proton B-field measurements, fig. 4.4 for measured carbon ion energies, fig. 4.5 for carbon ion RFC measurements, fig. 4.6 for carbon ion B-field measurements.

4.2.1. Protons

The comparison between measured and calculated absolute values for measured proton base energies, depicted in tab. 4.8 shows some non negligible differences in range and frequency of up to 0.76%, that will be discussed in chapter 5. These differences can also be seen in fig. 4.1 and fig. 4.2. The difference in magnetic field strength of the dipole magnets however, is rather small showing a nice agreement of values in fig. 4.3.

Comparison of absolute values for protons				
	Energy [MeV]	Range [mm]	Frequency [Hz]	B-Field [mT]
Measurement	62.16	33.12	1335311	272.81
Model	62.16	32.86	1339635	272.90
Δ		0.25	-4323	-0.09
Δ(%)		0.76%	-0.32%	-0.03%

(a) Proton absolute values at 62.4 MeV

Measurement	197.29	251.97	2170711	502.83
Model	197.29	252.93	2174620	502.84
Δ		-0.96	-3909	-0.01
Δ(%)		-0.38%	-0.18%	-0.002%

(b) Proton absolute values at 198.0 MeV

Table 4.8.: Comparison of calculated and measured absolute values for 62.4 and 198.0 MeV protons

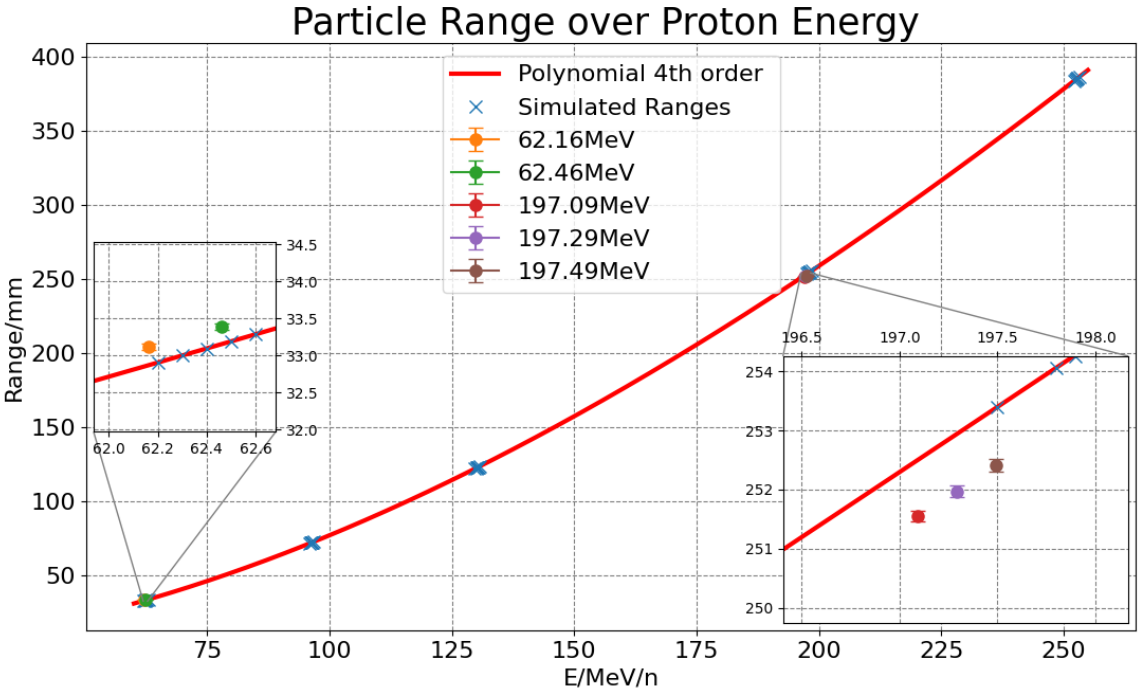

Figure 4.1.: Particle range model over energy for protons with a_i determined by simulations plotted against peakfinder measurements.

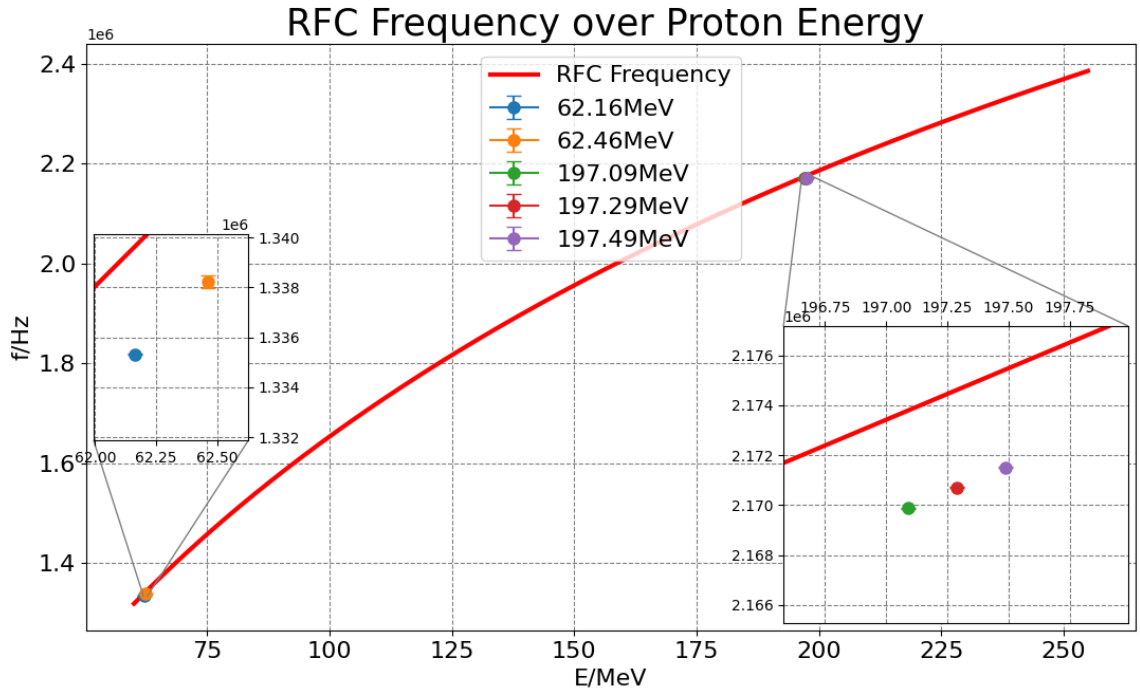

Figure 4.2.: RFC frequency model over energy for protons plotted against RFC frequency measurements.

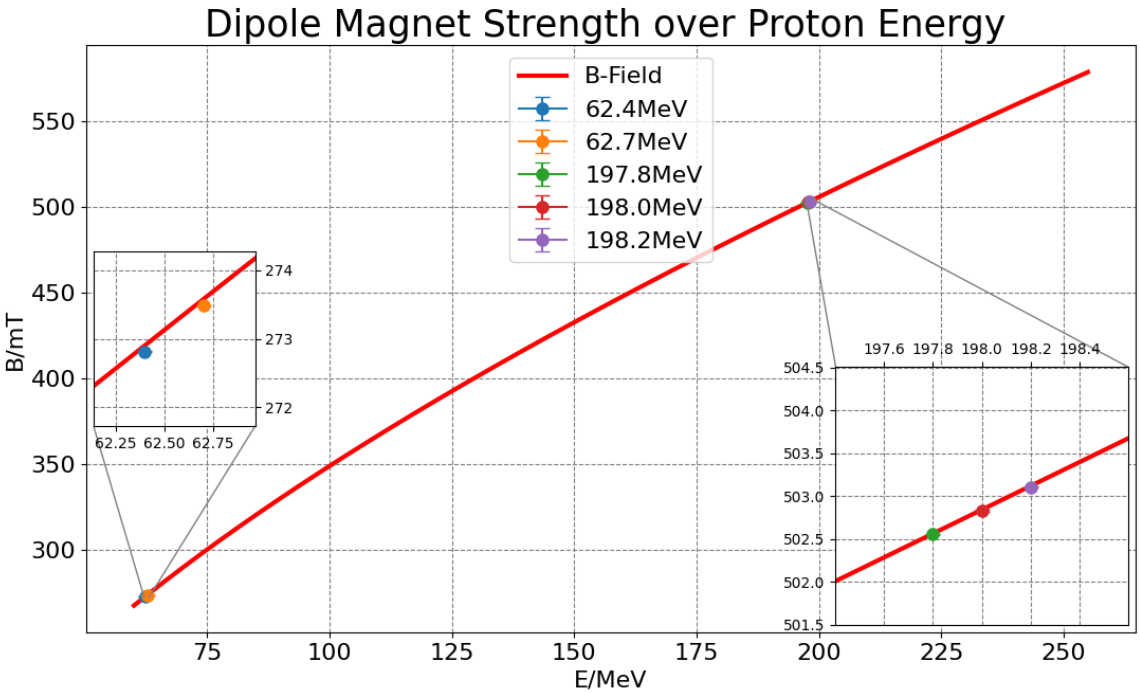

Figure 4.3.: B-field model over energy for protons plotted against B-field measurements.

4.2.2. Carbon Ions

As seen in tab. 4.9, the comparison between model and measurements for carbon ions look rather similar to the proton comparisons, in that the differences for range and frequency are larger than the difference in B-field strength and that the difference in range switches sign over energy. Again, these findings are visualized in fig. 4.4, fig. 4.5 and fig. 4.6.

Comparison of absolute values for carbon ions				
	Energy [MeV/u]	Range [mm]	Frequency [Hz]	B-Field [mT]
Measurement	119.56	35.61	1783102	765.35
Model	119.56	35.48	1788247	765.45
Δ		0.13	-5145	-0.10
Δ(%)		0.37%	-0.29%	-0.013%

(a) Carbon ion absolute values at 120.0 MeV/u

Measurement	398.76	272.22	2752795	1492.86
Model	398.76	272.82	2756127	1493.14
Δ		-0.60	-3332	-0.28
Δ(%)		-0.22%	-0.12%	-0.019%

(b) Carbon ion absolute values at 400.1 MeV/u

Table 4.9.: Comparison of calculated and measured absolute values for 120.0 and 400.1 MeV/u carbon ions

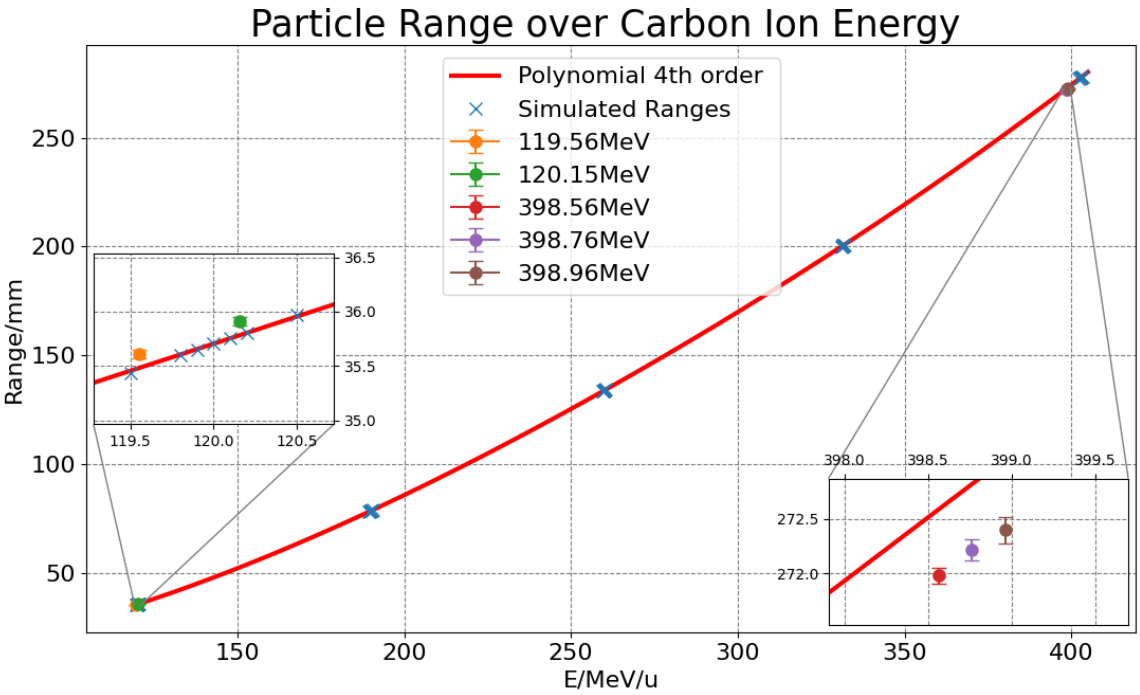

Figure 4.4.: Particle range model over energy for carbon ions with a_i determined by simulations plotted against peakfinder measurements.

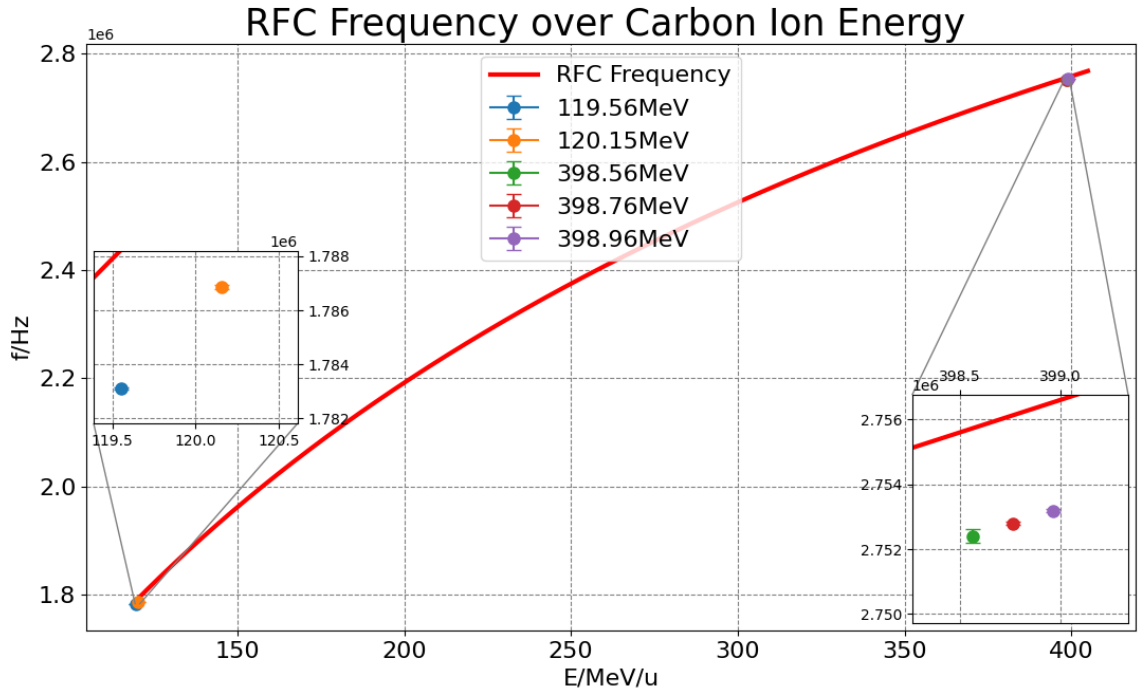

Figure 4.5.: RFC frequency model over energy for carbon ions plotted against RFC frequency measurements.

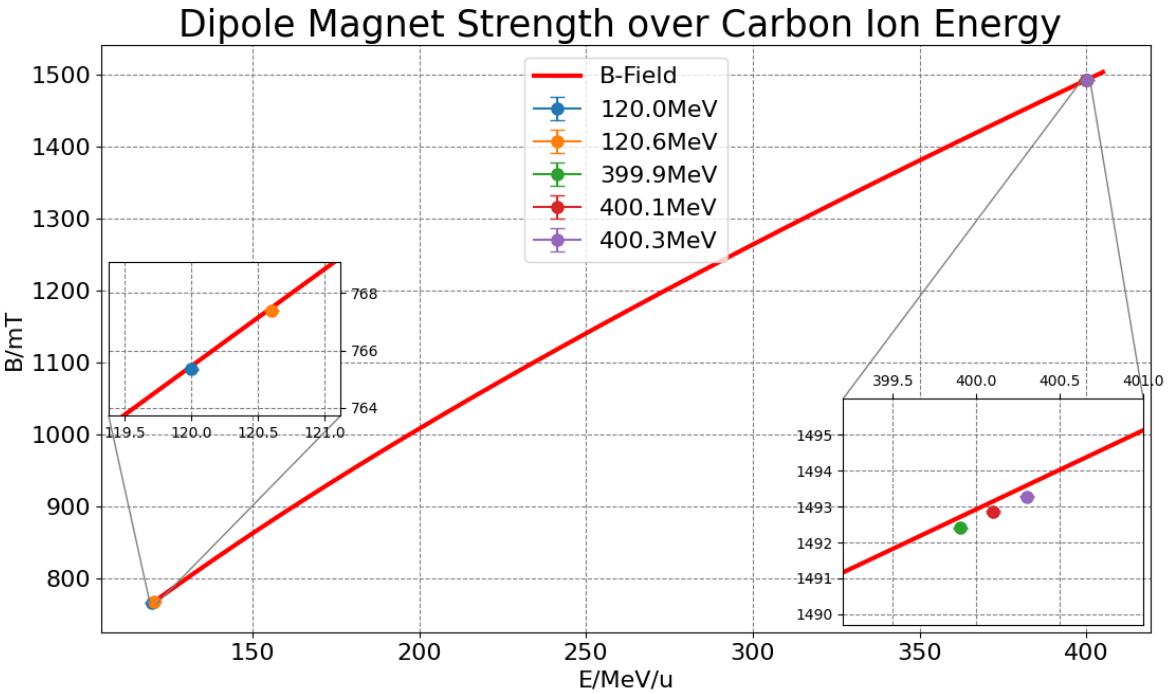

Figure 4.6.: B-field model over energy for carbon ions plotted against B-field measurements.

4.3. Measured Relative Values

In this section, the relative values in energy, revolution frequency and B-field strength at 2 base energies per particle type are presented for range differences of 0.3, 0.5 and 1 mm to the ranges of 62 MeV protons, 198 MeV protons, 120 MeV carbon ions and 400 MeV carbon ions. Each of the calculated range differences is depicted as a curve, with 2 measured range differences per curve. Which point belongs to which curve will be noted in the legend. For relative energy values, simulated data points are depicted also.

4.3.1. Protons

The comparison of calculated and measured relative values can be seen in tab. 4.10 for 62.4 MeV protons and in tab. 4.11 for 198 MeV protons. Comparisons for both base energies are visualized in fig. 4.7 for energy-, fig. 4.8 for frequency- and fig. 4.9 for B-field strength deviations. Additionally, differences between model and simulated relative energy values are given in tab. 4.2, 4.3 and 4.4.

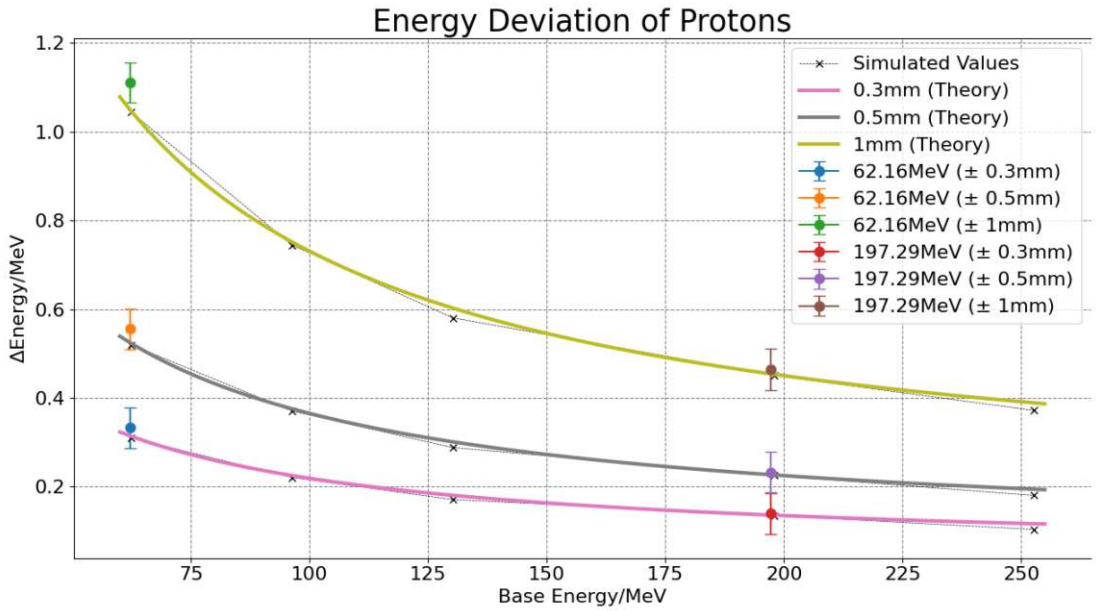

Figure 4.7.: Range deviation model (0.3-0.5-1mm) over energy for protons plotted against values obtained by analysis of range measurements.

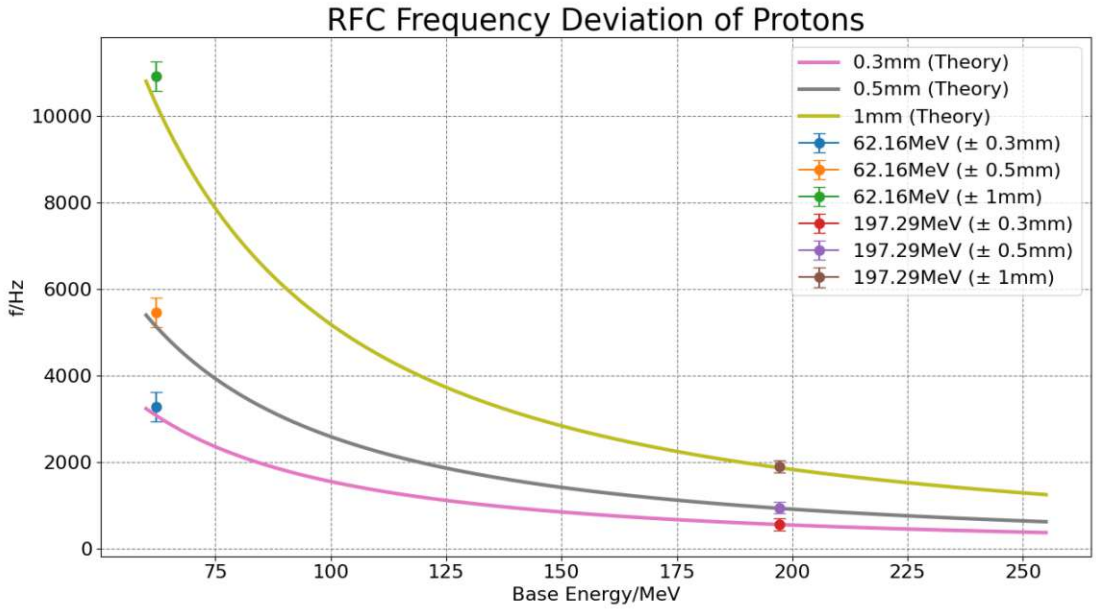

Figure 4.8.: Frequency deviation model (0.3-0.5-1mm) over proton energy plotted against values obtained by analysis of RFC and range measurements.

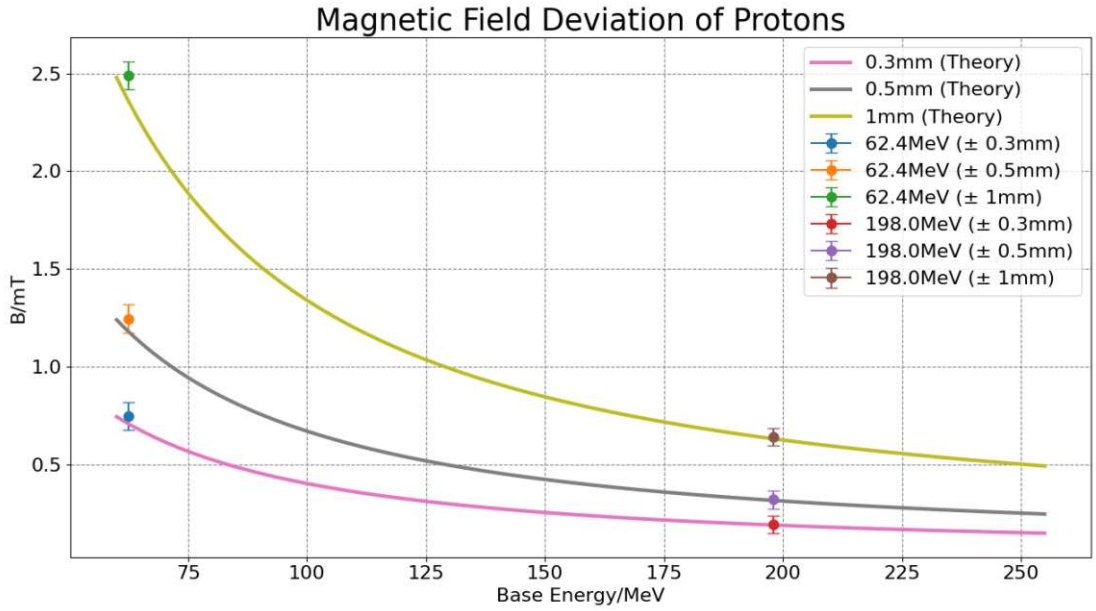

Figure 4.9.: B-field deviation model (0.3-0.5-1mm) over proton energy plotted against values obtained by analysis of B-field and range measurements.

Comparison of relative values for 62.4 MeV protons				
	ΔR [mm]	ΔE [MeV]	ΔF [Hz]	ΔB [mT]
Measurement	0.3	0.333	3275	0.747
Model	0.3	0.315	3080	0.709
Δ		0.018	195	0.038
Measurement	0.5	0.556	5459	1.245
Model	0.5	0.525	5134	1.181
Δ		0.031	325	0.064
Measurement	1	1.111	10919	2.490
Model	1	1.050	10269	2.363
Δ		0.061	650	0.127
$\Delta(\%)$		5.71%	6.33%	5.36%

Table 4.10.: Comparison of calculated and measured relative values for 62.4 MeV protons

Comparison of relative values for 198 MeV protons				
	ΔR [mm]	ΔE [MeV]	ΔF [Hz]	ΔB [mT]
Measurement	0.3	0.140	571	0.192
Model	0.3	0.136	562	0.189
Δ		0.004	9	0.003
Measurement	0.5	0.233	952	0.320
Model	0.5	0.227	936	0.315
Δ		0.006	16	0.005
Measurement	1	0.465	1903	0.640
Model	1	0.454	1872	0.631
Δ		0.011	31	0.009
$\Delta(\%)$		2.42%	1.66%	1.42%

Table 4.11.: Comparison of calculated and measured relative values for 198.0 MeV protons

4.3.2. Carbon Ions

For carbon ions, the comparison of calculated and measured relative values can be seen in tab. 4.12 for 120 MeV/u and in tab. 4.13 for 400.1 MeV/u. Comparisons for both base energies are visualized in fig. 4.10 for energy-, fig. 4.11 for frequency- and fig. 4.12 for B-field strength deviations. Differences between model and simulated values are given in tab. 4.5, 4.6 and 4.7.

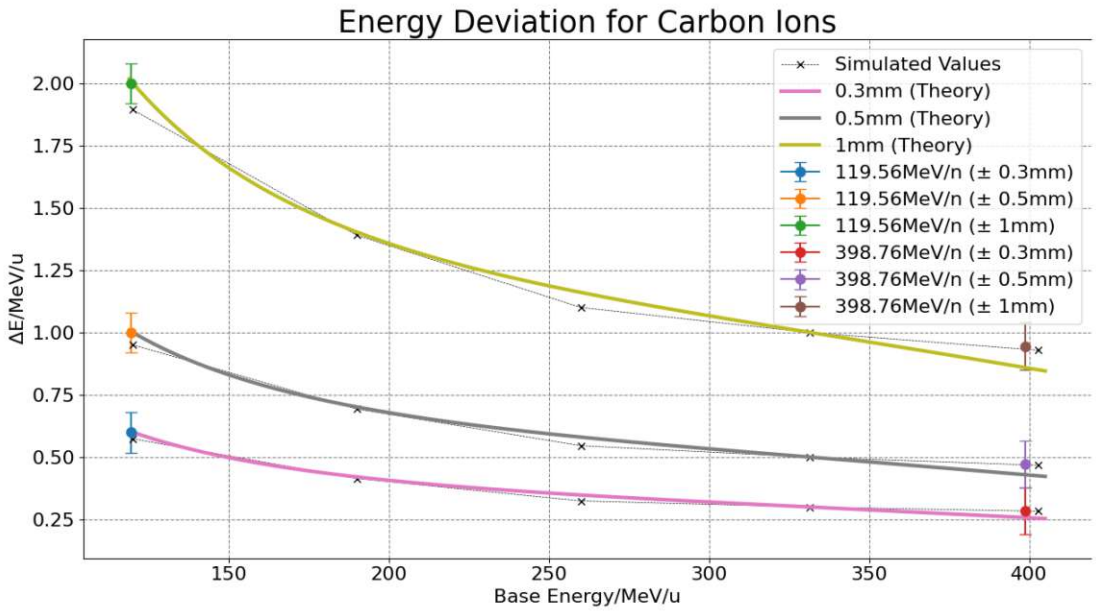

Figure 4.10.: Range deviation model (0.3-0.5-1mm) over energy for carbon ions plotted against values obtained by analysis of range measurements.

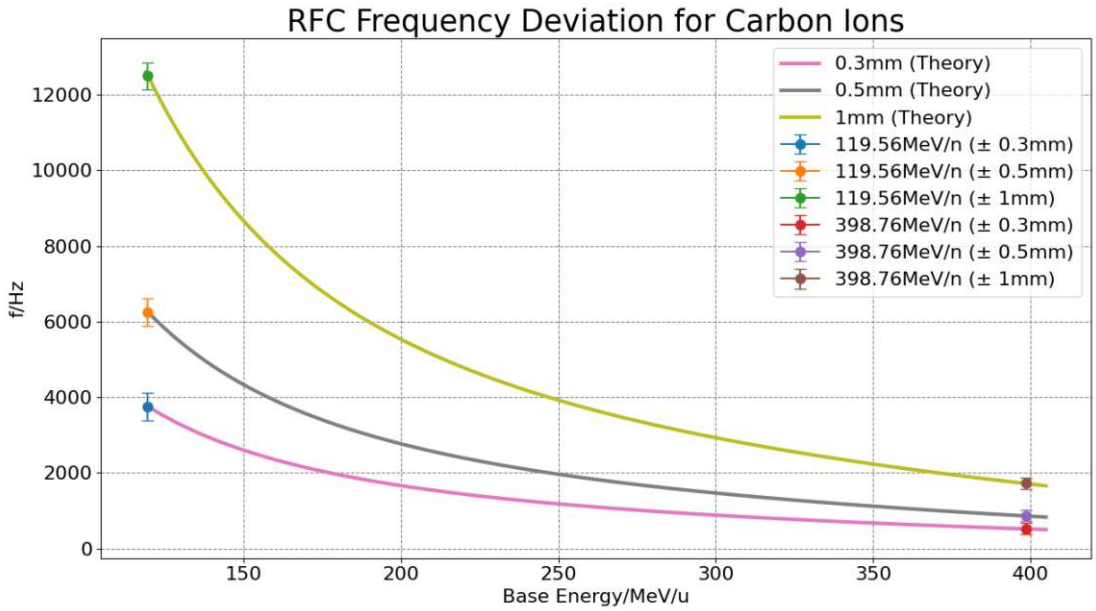

Figure 4.11.: Frequency deviation model (0.3-0.5-1mm) over energy plotted against values obtained by analysis of RFC and range measurements.

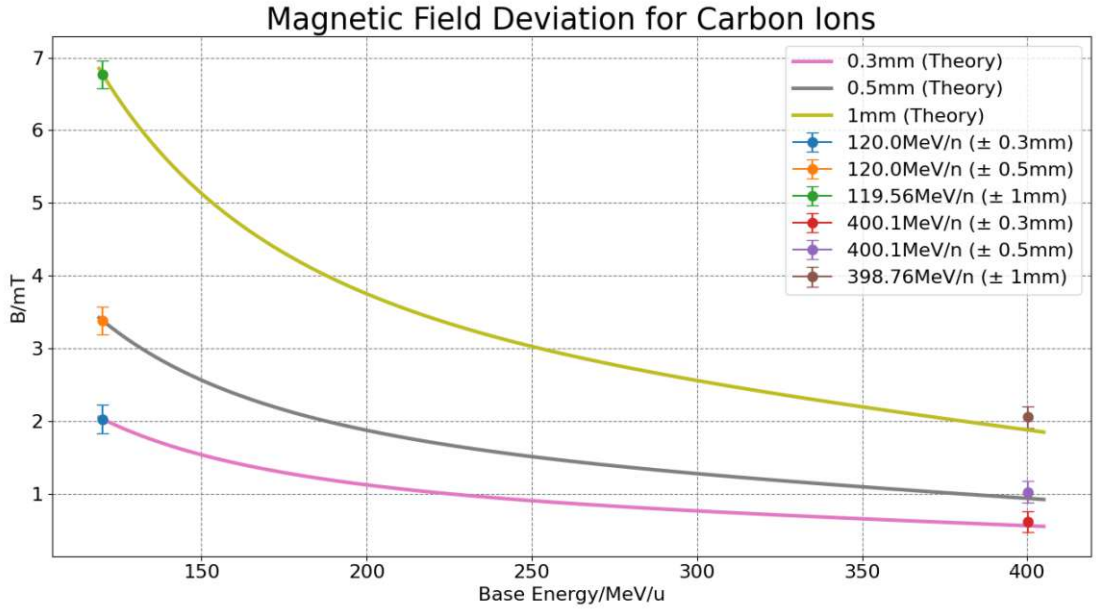

Figure 4.12.: B-field deviation model (0.3-0.5-1mm) over ion energy plotted against values obtained by analysis of B-field and range measurements.

Comparison of relative values for 120 MeV carbon ions				
	ΔR [mm]	ΔE [MeV/u]	ΔF [Hz]	ΔB [mT]
Measurement	0.3	0.600	3750	2.031
Model	0.3	0.603	3754	2.032
Δ		-0.003	-4	-0.001
Measurement	0.5	1.000	6250	3.385
Model	0.5	1.005	6258	3.387
Δ		-0.005	-8	-0.002
Measurement	1	2.000	12499	6.770
Model	1	2.010	12518	6.775
Δ		-0.010	-19	-0.005
Δ(%)		-0.49%	-0.15%	-0.074%

Table 4.12.: Comparison of calculated and measured relative values for 120.0 carbon ions

Comparison of relative values for 400.1 MeV carbon ions				
	ΔR [mm]	ΔE [MeV/u]	ΔF [Hz]	ΔB [mT]
Measurement	0.3	0.284	518	0.617
Model	0.3	0.258	514	0.564
Δ		0.026	4	0.053
Measurement	0.5	0.473	864	1.029
Model	0.5	0.430	857	0.940
Δ		0.043	7	0.089
Measurement	1	0.946	1727	2.057
Model	1	0.860	1713	1.881
Δ		0.086	14	0.176
Δ(%)		10.07%	0.82%	9.36%

Table 4.13.: Comparison of calculated and measured relative values for 400.1 carbon ions

4.4. Probability of a faulty Interlock

The final task of this thesis, is the evaluation of the obtained data to predict the odds of a faulty interlock, meaning a spill, that is within the safety regulations but would be detected as unsafe by the EVS. This is done by comparing the calculated 0.3 mm offsets to the standard deviation of RFC and B-field measurements. These comparisons can be seen in tab. 4.14 for frequency and in tab. 4.15 for magnetic field strength. From these tables, it can been concluded, that it is practically impossible to get an outlier of a spill with the correct energy, that would falsely trigger the EVS.

False Interlock by RFC frequency				
Energy [MeV]	0.3mm Offset [Hz]	Standard Deviations of Spills [Hz]	0.3mm Offset in Standard Deviations	Chance of false Interlock
62.2	3080	17.7	$\sim 185\sigma$	~ 0
62.7	3080	248.1	$\sim 13\sigma$	~ 0
197.8	562	19.9	$\sim 29\sigma$	~ 0
198.0	562	18.1	$\sim 31\sigma$	~ 0
198.2	562	18.2	$\sim 31\sigma$	~ 0
120.0	3754	41.0	$\sim 91\sigma$	~ 0
120.6	3754	65.0	$\sim 58\sigma$	~ 0
399.9	514	24.4	$\sim 25\sigma$	~ 0
400.1	514	55.9	$\sim 9\sigma$	~ 0
400.3	514	47.3	$\sim 11\sigma$	~ 0

Table 4.14.: 0.3mm offsets in standard deviations of RFC frequency measurements and subsequent chance of a faulty interlock

False Interlock by B-field strength				
Energy [MeV]	0.3mm Offset [μT]	Standard Deviations of Spills [μT]	0.3mm Offset in Standard Deviations	Chance of false Interlock
62.2	709	4.4	$\sim 170\sigma$	~ 0
62.7	709	4.4	$\sim 170\sigma$	~ 0
197.8	189	5.1	$\sim 38\sigma$	~ 0
198.0	189	6.6	$\sim 29\sigma$	~ 0
198.2	189	5.6	$\sim 34\sigma$	~ 0
120.0	2032	7.7	$\sim 264\sigma$	~ 0
120.6	2032	8.6	$\sim 236\sigma$	~ 0
399.9	564	17.3	$\sim 36\sigma$	~ 0
400.1	564	17.5	$\sim 35\sigma$	~ 0
400.3	564	18.5	$\sim 33\sigma$	~ 0

Table 4.15.: 0.3mm offsets in standard deviations of B-field measurements and subsequent chance of faulty interlock

5. Conclusion

Before concluding this thesis, it has to be said, that the measured absolute values don't always agree perfectly with the model - especially for the range measurements. While some of the offset can be explained by passing through some nozzle elements and the peakfinder entrance window, not all of it can be resolved as of writing this thesis. Possible contenders for these issues might be:

- The limitations of the approximated range model
- The limited accuracy of the Peakfinder
- Problems with the (at the time) still experimental RFKO settings at MedAustron

Additionally, a constant offset of in the order of a few kHz can be seen in absolute RFC frequency measurements. A possible reason for this is a know compensation factor of 0.995995981 in the processing of RFC measurements in the MedAustron framework. This factor is however not direct - in fact, how the factor is implemented, is not known at this moment and therefore can not be factored into the presented results. While these unexplained inaccuracies in the absolute range values are obviously a nuisance, they are actually not as problematic as they seem on first glance, as only the relative values - which agree quite well in theory and experiment - are actually used to validate the EVS.

To summarize, it has been shown, that the presented mathematical model is capable of calculating the RFC and B-field offsets equivalent to 0.3mm offset in penetration depth for all energies and particle types used in ion therapy at MedAustron, reliably. The relative error never exceeded 10.07% (with most relative errors being significantly below that value) making the worst case offset a patient could experience 0.3302mm. Alternatively the safe setting for the EVS, so that the maximal offset never exceeds 0.3mm, would be 0.2726mm. Additionally, the calculated 0.3mm offsets represented in standard deviation of RFC frequency (9σ - 185σ) and B-field (29σ - 264σ) measurements, show that a false positive, meaning the triggering of an interlock with a safe spill, is practically impossible. Thus, the calculated model values of the EVS can be seen as validated, according to the conditions set in sec. 3.1 and sec. 3.5.

A. Sub-results

A.1. Dose Depth Measurements Analysis

In this chapter, the sub-results of the measurement analyses for Peakfinder, RFC and B-field measurements are given. These following tables and figures are the basis for the results shown in chapter 4. For each energy of each measurement, there will be tables presented containing information about parameters determined from the raw measurement, but also fitted data and fit parameters. Additionally, figures containing visualization about the measurements and the linear fitting process are provided. Each figure will have the "measured" 0.3mm limits and their uncertainties marked as red lines. While peakfinder measurements will only have the bragg peaks shown, the other measurements will feature sub-result sheets, that feature:

- RFC frequency:
  - A boxplot
  - A histogram containing mean, median and marks for 5σ
  - The plateau frequencies for all analyzed spills
- Magnetic field strength:
  - A boxplot
  - A histogram containing mean, median and marks for 5σ
  - The plateau field strength for all analyzed spills
  - A plot showing the whole spill cycles field strength with the analyzed part marked

A.1.1. Protons

Peakfinder Measurement Proton 62.4 MeV				
Raw Data				
Peak	32.8	mm	4.5417	Gy
R80	33.1	mm	3.63336	Gy
R20	33.7	mm	0.90834	Gy
R80 width	0.9	mm		
Penumbra width	0.6	mm		
Fitted Data				
Peak	32.75	mm	4.54756	Gy
R80_f	33.12	mm	3.63805	Gy
R20	33.61	mm	0.909513	Gy
R80 width	0.97	mm		
Penumbra width	0.49	mm		
Uncertainty values for the R80	0.040418	mm		
Difference Raw-Fitted Data				
Peak	0.05	mm	5.86352e-03	Gy
R80	0.02	mm	4.69082e-03	Gy
R20	0.09	mm	1.17270e-03	Gy
R80 width	0.07	mm		
Penumbra width	0.11	mm		
R^2	0.999294			

Peakfinder Measurement Proton 62.7 MeV				
Raw Data				
Peak	33.0	mm	4.5783	Gy
R80	33.4	mm	3.66264	Gy
R20	34.0	mm	0.91566	Gy
R80 width	0.9	mm		
Penumbra width	0.6	mm		
Fitted Data				
Peak	33.02	mm	4.54073	Gy
R80_f	33.39	mm	3.63258	Gy
R20	33.9	mm	0.908146	Gy
R80 width	0.96	mm		
Penumbra width	0.51	mm		
Uncertainty	0.04186	mm		
Differences Raw-Fitted Data				
Peak	0.02	mm	0.03757	Gy
R80	0.01	mm	0.030056	Gy
R20	0.1	mm	0.00751403	Gy
R80 width	0.06	mm		
Penumbra width	0.09	mm		
R^2	0.996425			

Linear Fit Proton 62.4 + 0.3 MeV		
Fit Parameters		
k	1.111111	
d	25.6	
Energy Offset for Range-Deviation		
0.3mm	0.333333	MeV
0.5mm	0.555556	MeV
1mm	1.111111	MeV
Standard Deviation	0.045717	MeV
Range Offset for 0.1 MeV Energy Deviation		
0.1 MeV	0.09	mm
R^2	1.0	

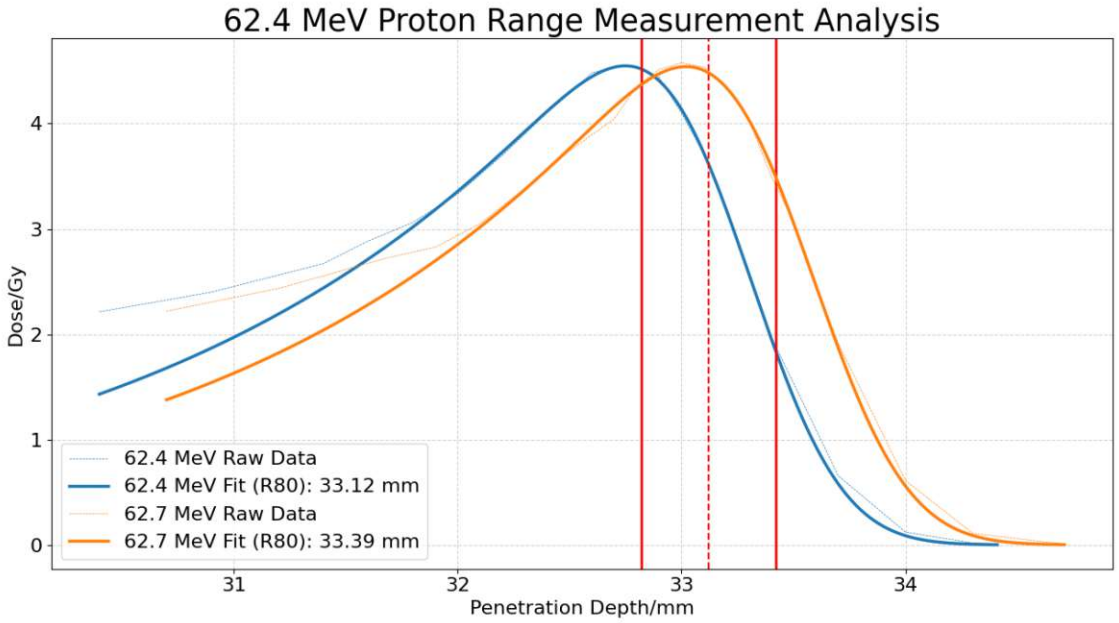

Figure A.1.: Proton 62.4 MeV Range Measurement Analysis with 0.3 mm limits.

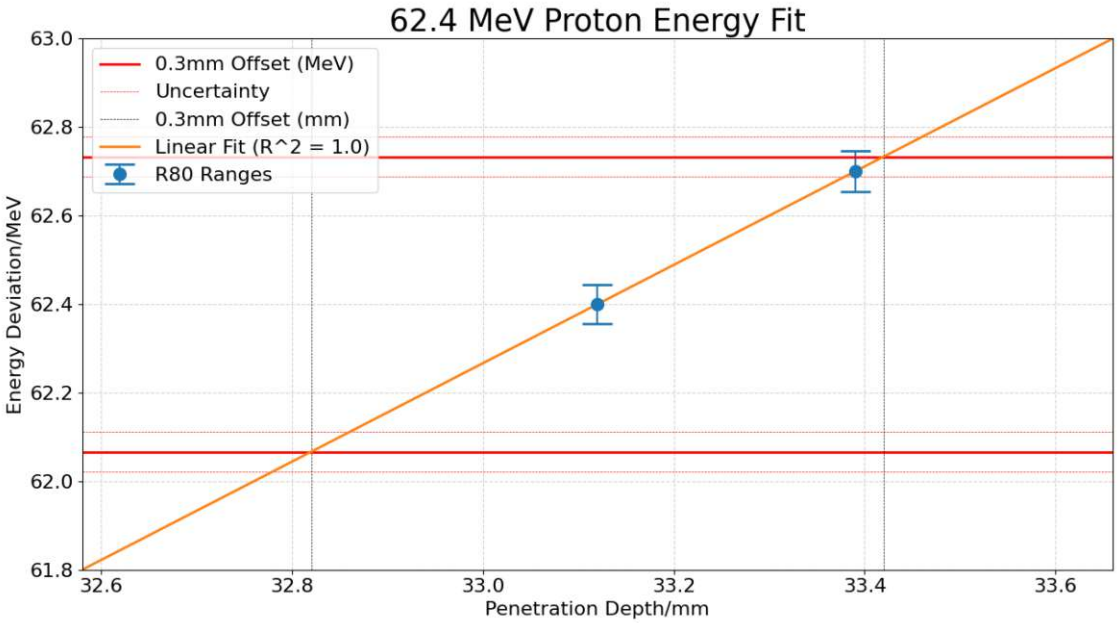

Figure A.2.: Proton 62.4 MeV linear range fit with 0.3 mm limits.

RFC Measurements Proton 62.4 + 0.3 MeV		
Proton 62.4 MeV RFC Measurement		
Mean	1335313.586207	Hz
Median	1335311.0	Hz
Standard Deviation	17.707425	Hz
Proton 62.7 MeV RFC Measurement		
Mean	1338261.612903	Hz
Median	1338224.0	Hz
Standard Deviation	248.125057	Hz
Linear Fit Parameters		
k	0.000102	
d	-73.485498	
RFC Frequency Offset for Range Deviation		
0.3mm	3275.585218	Hz
0.5mm	5459.308697	Hz
1mm	10918.617394	Hz
Standard Deviation	341.152006	Hz
R^2	1.0	

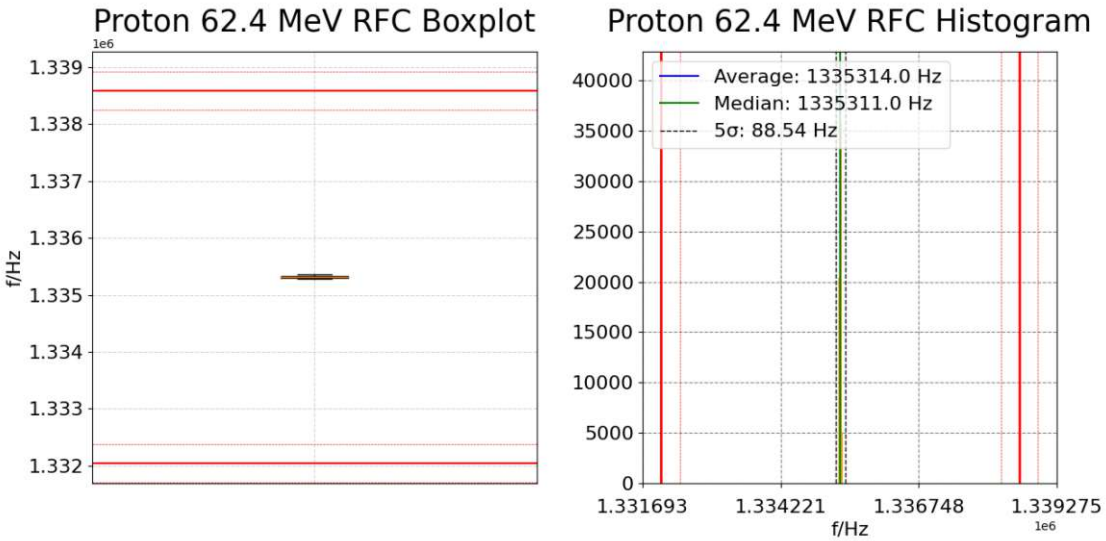

Figure A.3.: Proton 62.4 MeV RFC Frequency Boxplot & Histogram with 0.3 mm limits.

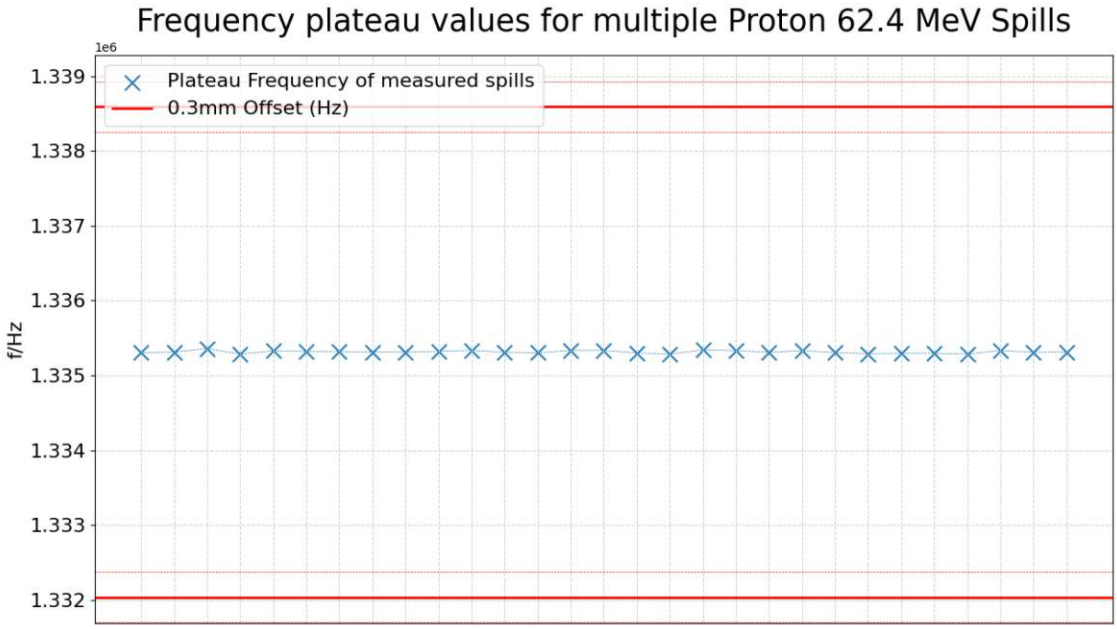

Figure A.4.: Proton 62.4 MeV measured RFC Frequency spill-plateuas with 0.3 mm limits.

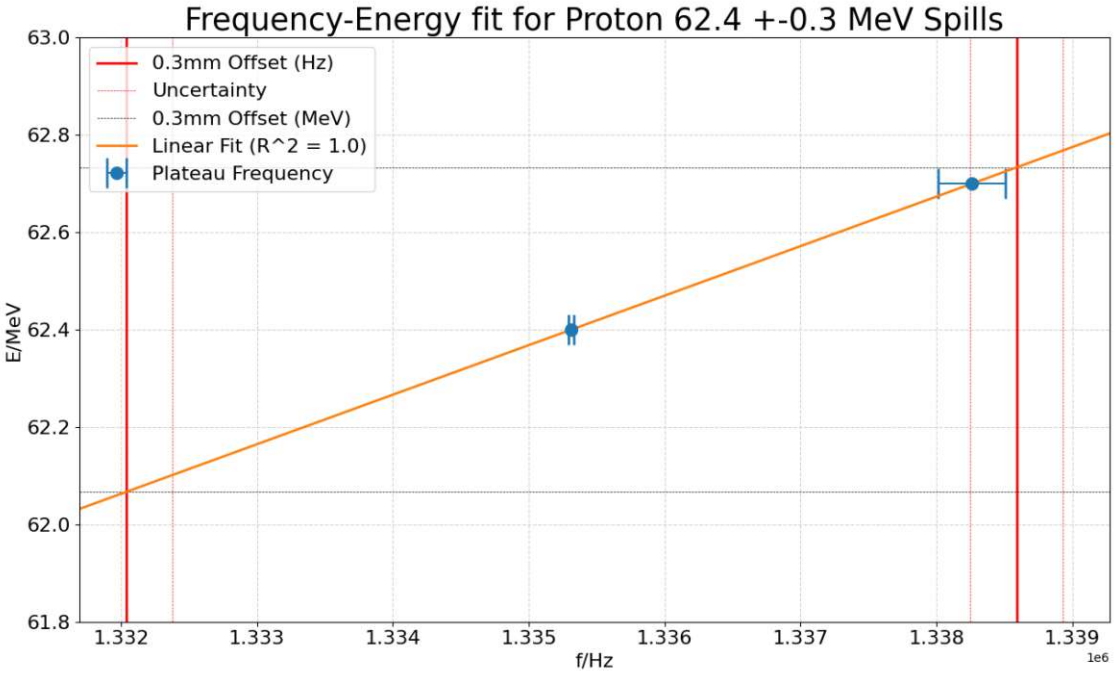

Figure A.5.: Proton 62.4 MeV RFC Frequency linear fit with 0.3 mm limits.

B-field Measurements Proton 62.4 + 0.3 MeV		
Proton 62.4 MeV B-field Measurement		
Mean	272.813006	mT
Median	272.813030	mT
Standard Deviation	0.004443	mT
Proton 62.7 MeV B-field Measurement		
Mean	273.485280	mT
Median	273.485308	mT
Standard Deviation	0.004352	mT
Fit Parameters		
k	0.446244	
d	-59.341234	
B-field Offset for Range Deviation		
0.3mm	0.746975	mT
0.5mm	1.244959	mT
1mm	2.489917	mT
Standard Deviation	0.072509	mT
R^2	1.0	

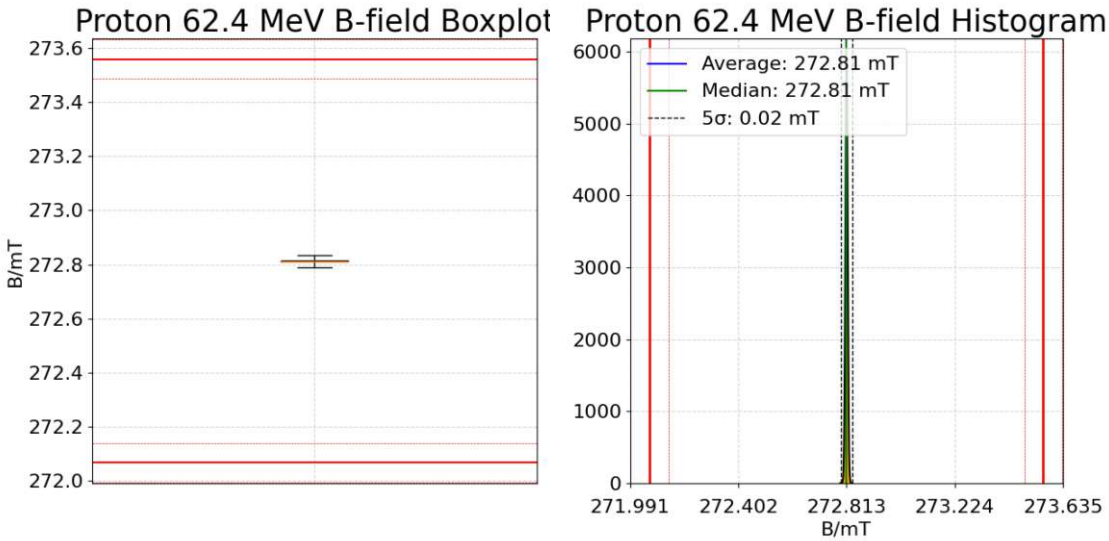

Figure A.6.: Proton 62.4 MeV B-field Boxplot & Histogram with 0.3 mm limits.

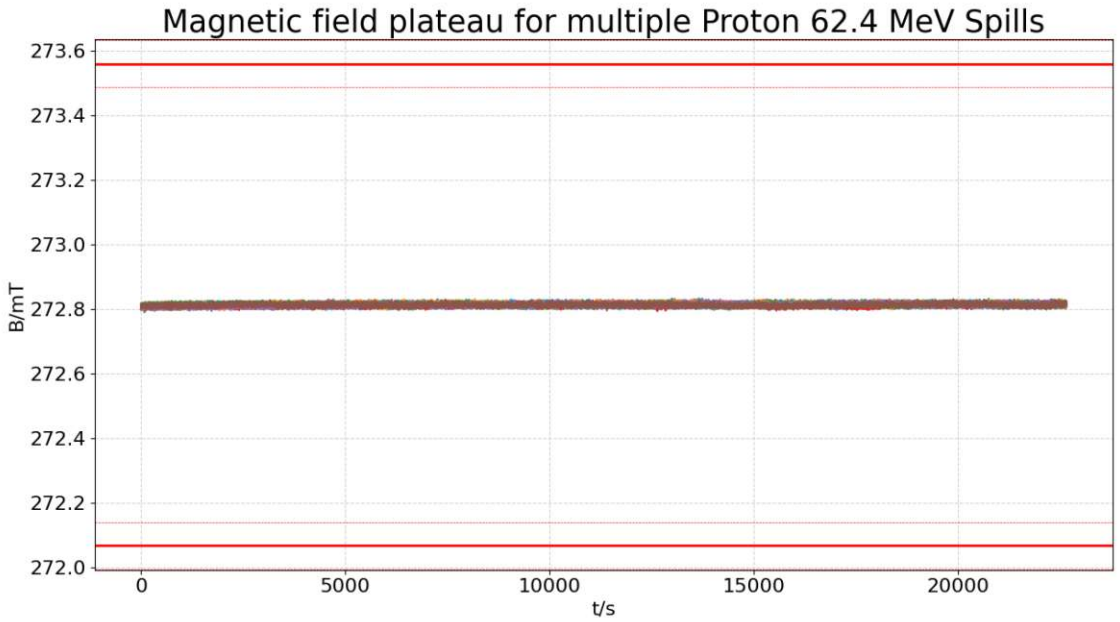

Figure A.7.: Proton 62.4 MeV measured B-field spill-plateaus with 0.3 mm limits.

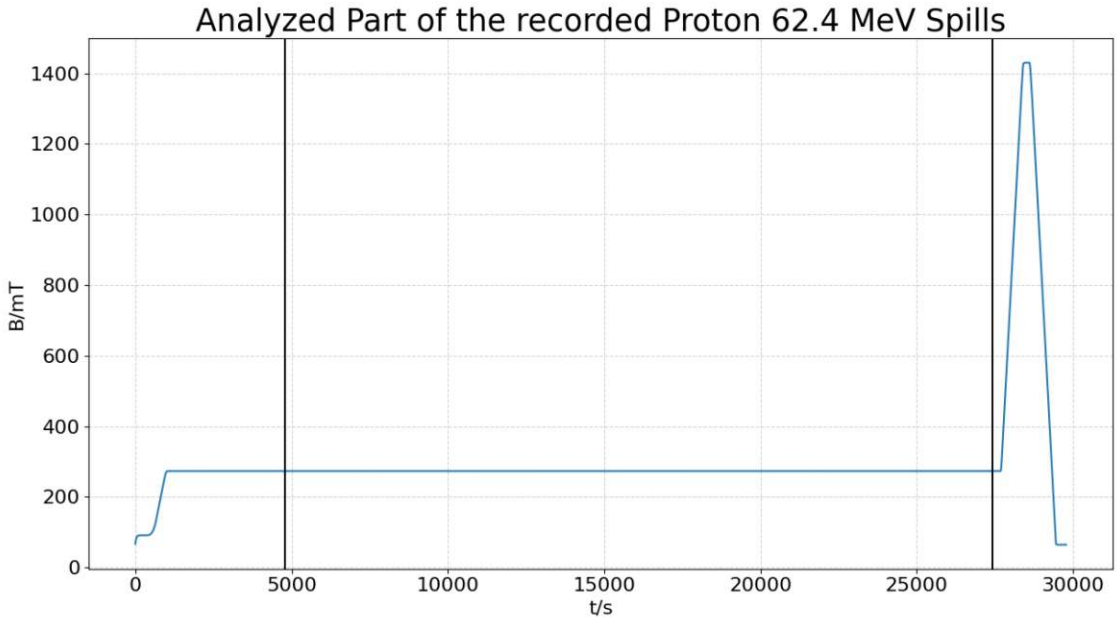

Figure A.8.: Proton 62.4 MeV analyzed part of the spill in measured B-field.

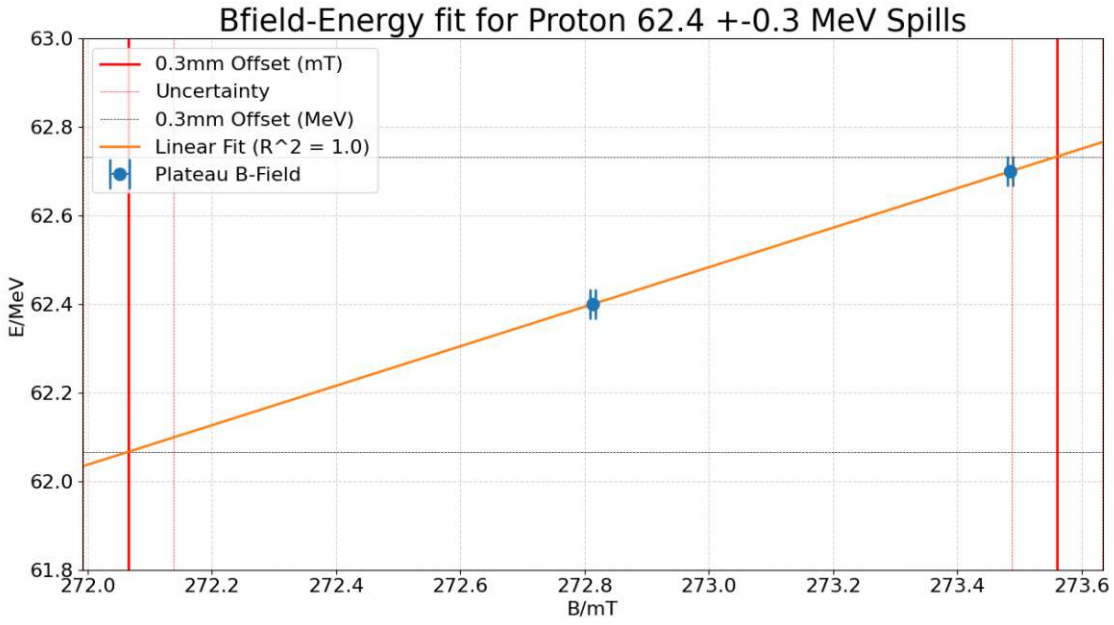

Figure A.9.: Proton 62.4 MeV B-field linear fit with 0.3 mm limits.

Peakfinder Measurement Proton 197.8 MeV				
Raw Data				
Peak	248.9	mm	3.655800	Gy
R80	251.4	mm	2.924640	Gy
R20	254.9	mm	0.731160	Gy
R80 width	7.0	mm		
Penumbra width	3.5	mm		
Fitted Data				
Peak	248.990000	mm	3.671408	Gy
R80_f	251.550000	mm	2.937127	Gy
R20	255.080000	mm	0.734282	Gy
R80 width	6.330000	mm		
Penumbra width	3.530000	mm		
Uncertainty	0.103979	mm		
Difference Raw-Fitted Data				
Peak	0.090000	mm	0.015608	Gy
R80	0.150000	mm	0.012487	Gy
R20	0.180000	mm	0.003122	Gy
R80 width	0.670000	mm		
Penumbra width	0.030000	mm		
R^2	0.998117			

Peakfinder Measurement Proton 198.0 MeV				
Raw Data				
Peak	249.4	mm	3.687900	Gy
R80	251.9	mm	2.950320	Gy
R20	255.4	mm	0.737580	Gy
R80 width	6.5	mm		
Penumbra width	3.5	mm		
Fitted Data				
Peak	249.400000	mm	3.686595	Gy
R80_f	251.970000	mm	2.949276	Gy
R20	255.550000	mm	0.737319	Gy
R80 width	6.260000	mm		
Penumbra width	3.580000	mm		
Uncertainty	0.091572	mm		
Difference Raw-Fitted Data				
Peak	0.000000	mm	0.001305	Gy
R80	0.070000	mm	0.001044	Gy
R20	0.150000	mm	0.000261	Gy
R80 width	0.240000	mm		
Penumbra width	0.080000	mm		
R^2	0.999366			

Peakfinder Measurement Proton 198.2 MeV				
Raw Data				
Peak	248.9	mm	3.649400	Gy
R80	252.4	mm	2.919520	Gy
R20	256.4	mm	0.729880	Gy
R80 width	7.0	mm		
Penumbra width	4.0	mm		
Fitted Data				
Peak	249.840000	mm	3.664638	Gy
R80_f	252.410000	mm	2.931710	Gy
R20	255.950000	mm	0.732928	Gy
R80 width	6.340000	mm		
Penumbra width	3.540000	mm		
Uncertainty	0.106280	mm		
Difference Raw-Fitted Data				
Peak	0.940000	mm	0.015238	Gy
R80	0.010000	mm	0.012190	Gy
R20	0.450000	mm	0.003048	Gy
R80 width	0.660000	mm		
Penumbra width	0.460000	mm		
R^2	0.998049			

Linear Fit Proton 198.0 ± 0.2 MeV		
Fit Parameters		
k	0.465032	
d	80.822675	
Energy Offset for Range Deviation		
0.3mm	0.139510	MeV
0.5mm	0.232516	MeV
1mm	0.465032	MeV
Standard Deviation	0.046883	MeV
Range Offset for 0.1 MeV Energy Deviation		
Range Offset	0.215039	mm
R^2	0.999820	

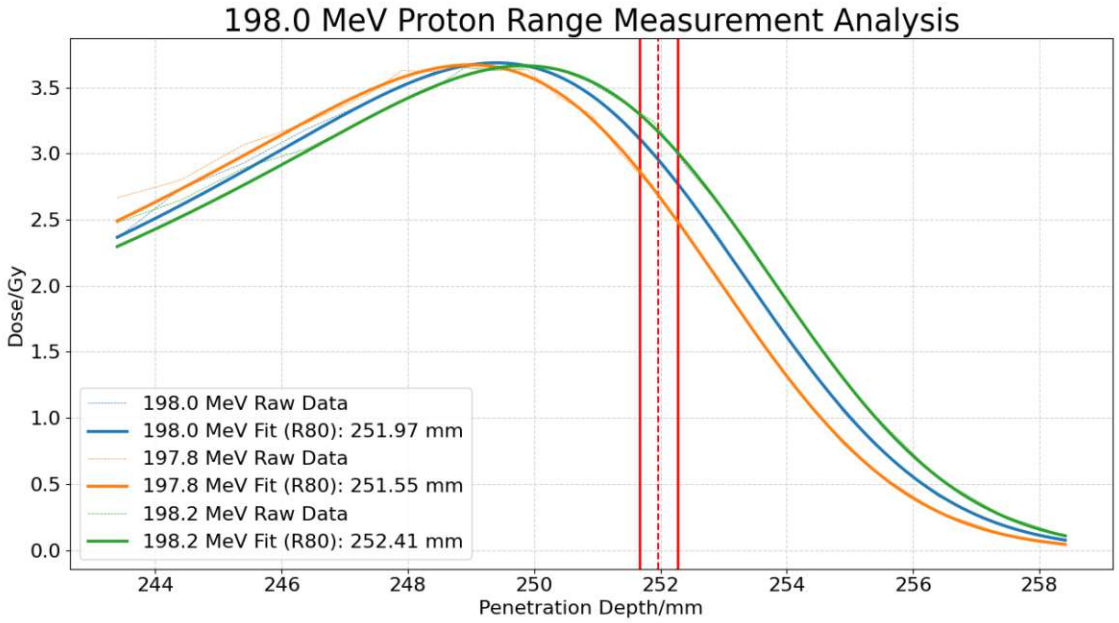

Figure A.10.: Proton 198 MeV Range Measurement Analysis with 0.3 mm limits.

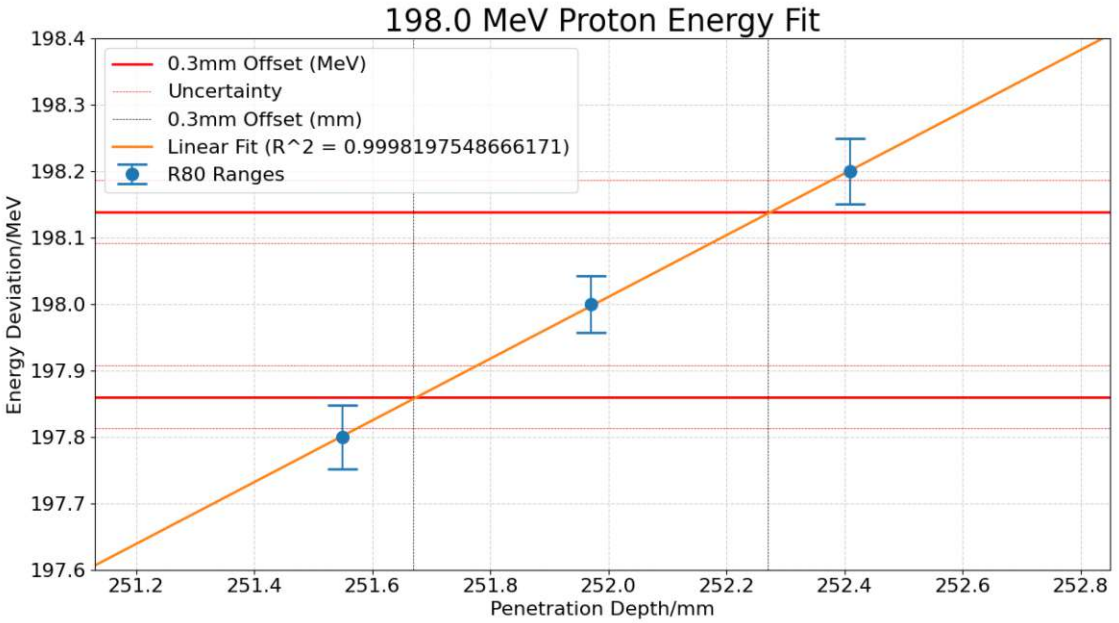

Figure A.11.: Proton 198 MeV linear range fit with 0.3 mm limits.

RFC Measurements Proton 198.0 ± 0.2 MeV		
Proton 197.8 MeV RFC Measurement		
Mean	2169877.280000	Hz
Median	2169875.000000	Hz
Standard Deviation	19.900794	Hz
Proton 198.0 MeV RFC Measurement		
Mean	2170710.833333	Hz
Median	2170710.500000	Hz
Standard Deviation	18.096194	Hz
Proton 198.2 MeV RFC Measurement		
Mean	2171514.055556	Hz
Median	2171517.000000	Hz
Standard Deviation	18.216208	Hz
Fit Parameters		
k	0.000244	
d	-332.421480	
RFC Frequency Offset for Range Deviation		
0.3mm	570.930648	Hz
0.5mm	951.551079	Hz
1mm	1903.102159	Hz
Standard Deviation	136.316166	Hz
R^2	0.999886	

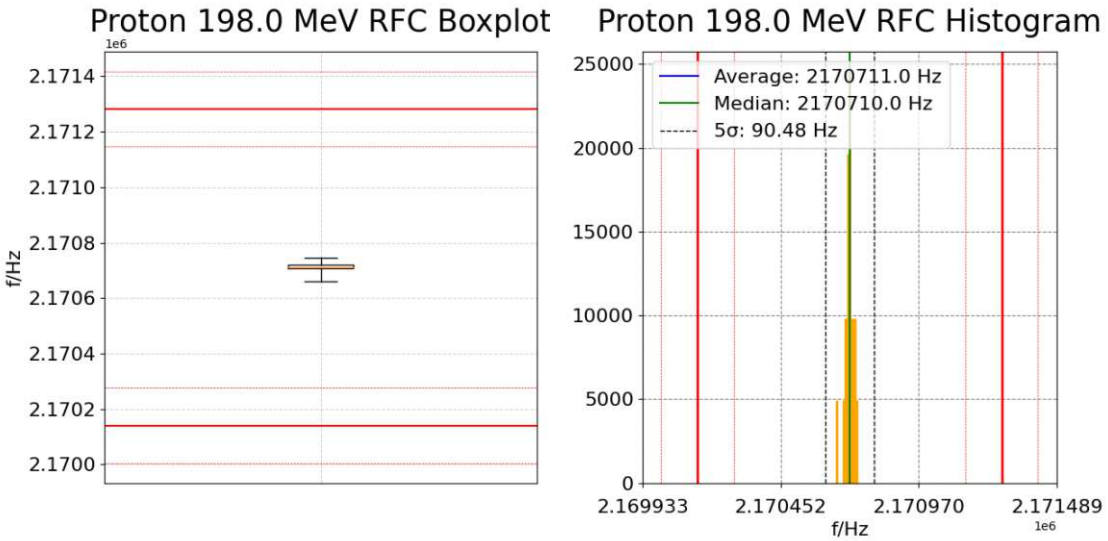

Figure A.12.: Proton 198 MeV RFC Frequency Boxplot & Histogram with 0.3 mm limits.

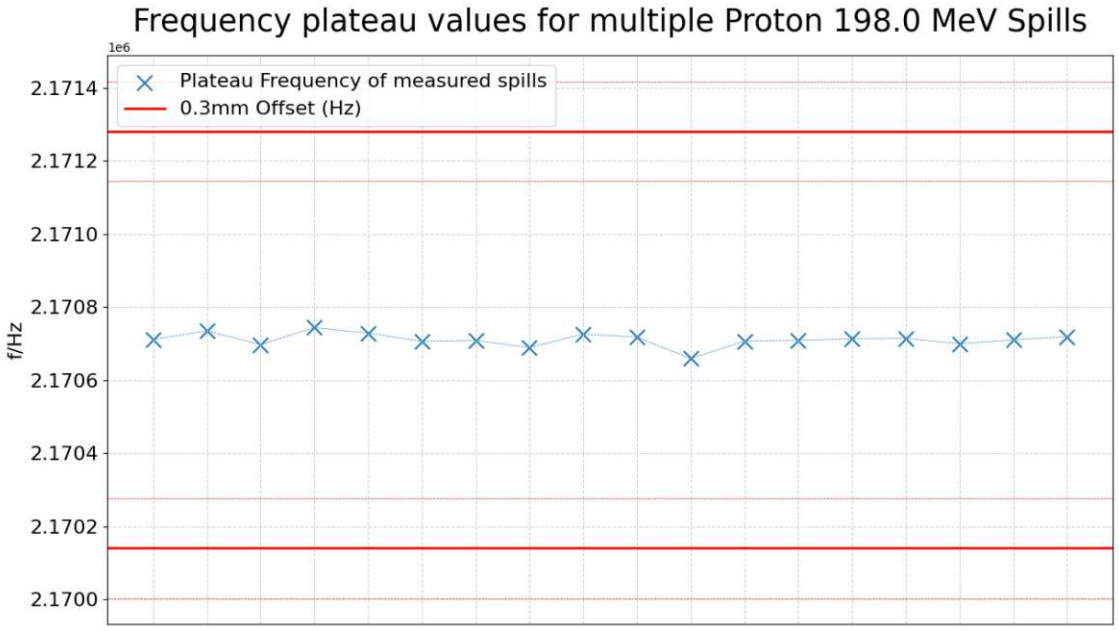

Figure A.13.: Proton 198 MeV measured RFC Frequency spill-plateuas with 0.3 mm limits.

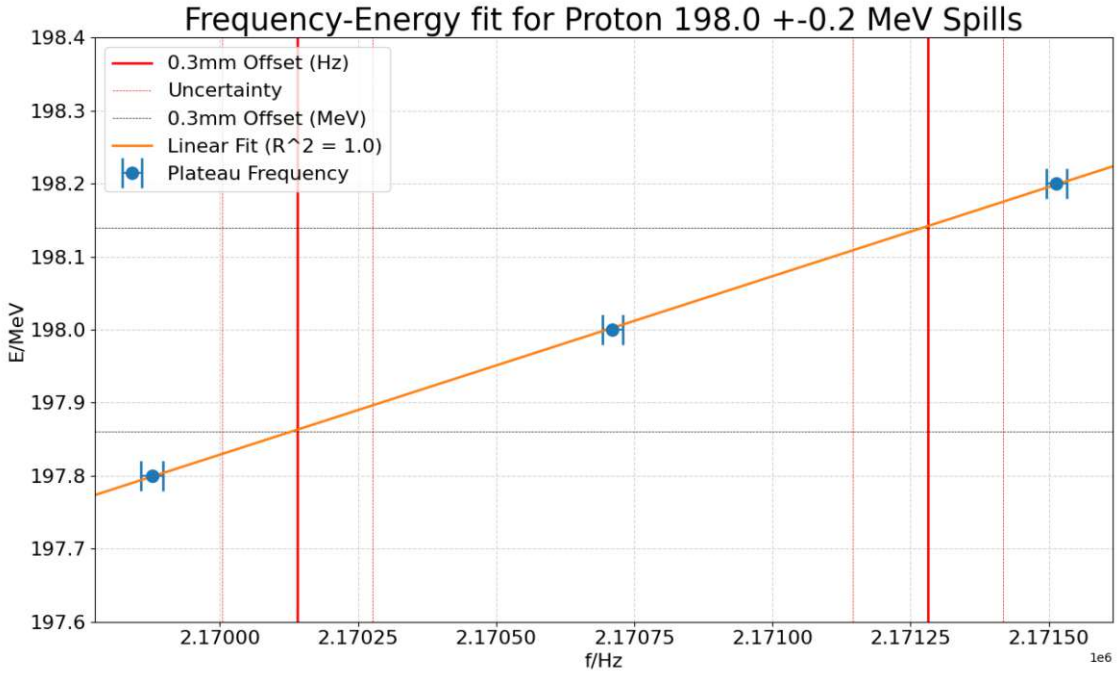

Figure A.14.: Proton 198 MeV RFC Frequency linear fit with 0.3 mm limits.

B-field Measurements Proton 198.0 ± 0.2 MeV		
Proton 197.8 MeV B-field Measurement		
Mean	502.554263	mT
Median	502.554303	mT
Standard Deviation	0.005120	mT
Proton 198.0 MeV B-field Measurement		
Mean	502.829337	mT
Median	502.829181	mT
Standard Deviation	0.006637	mT
Proton 198.2 MeV B-field Measurement		
Mean	503.104856	mT
Median	503.104974	mT
Standard Deviation	0.005627	mT
Fit Parameters		
k	0.726386	
d	-167.248088	
RFC Frequency Offset for Range Deviation		
0.3mm	0.192060	mT
0.5mm	0.320100	mT
1mm	0.640201	mT
Standard Deviation	0.045825	mT
R^2	0.999999	

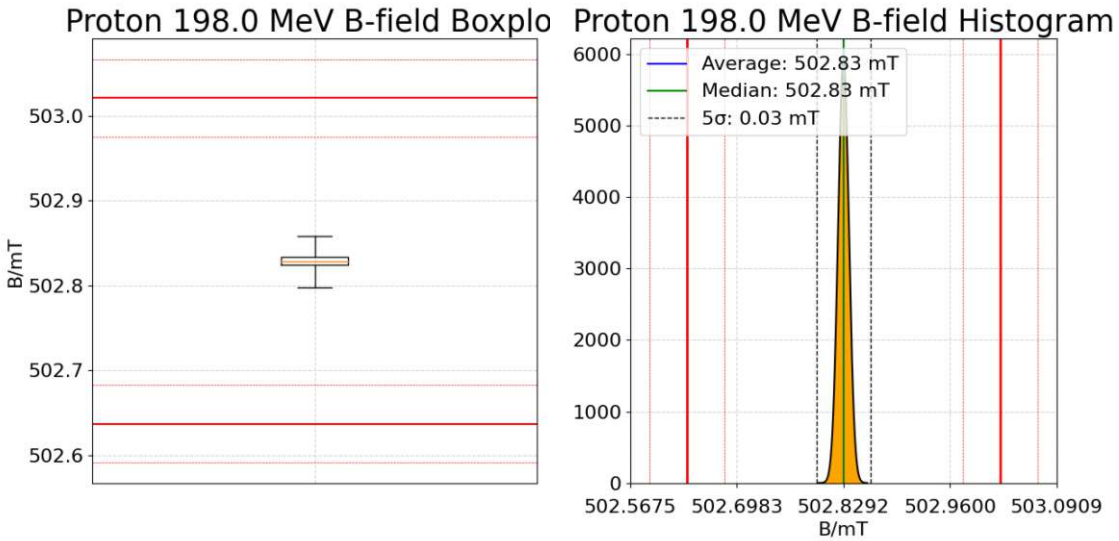

Figure A.15.: Proton 198 MeV B-field Boxplot & Histogram with 0.3 mm limits.

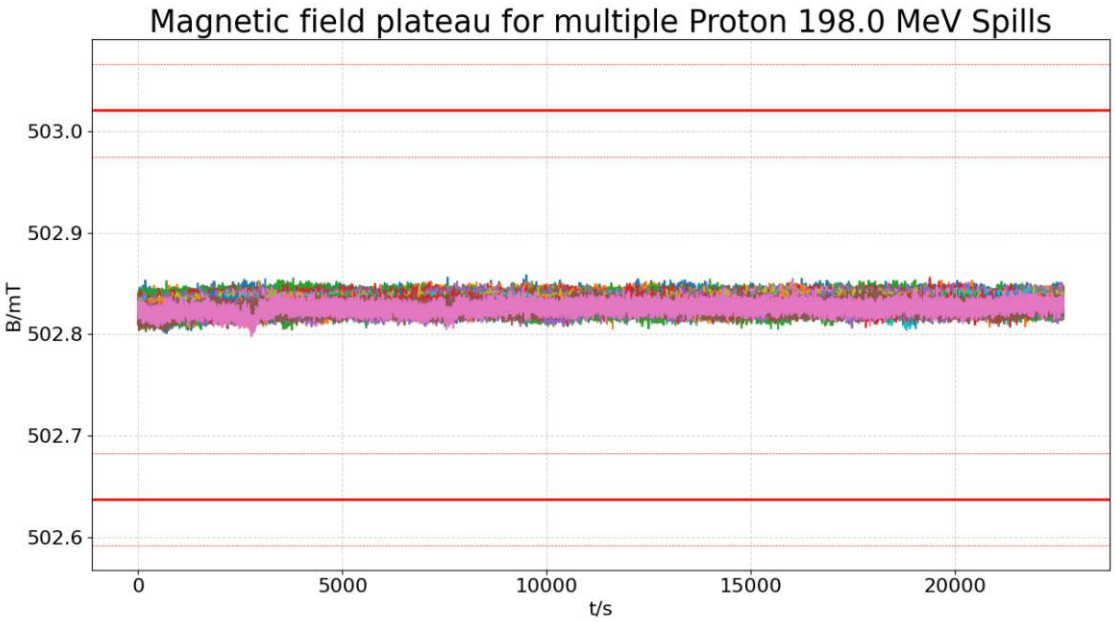

Figure A.16.: Proton 198 MeV measured B-field spill-plateaus with 0.3 mm limits.

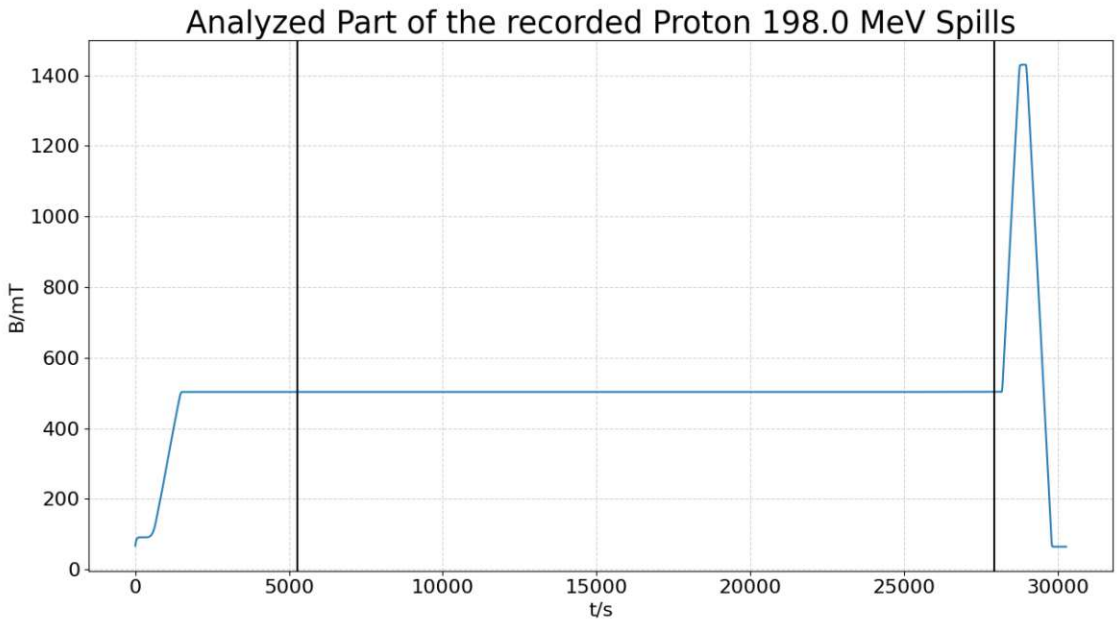

Figure A.17.: Proton 198 MeV analyzed part of the spill in measured B-field.

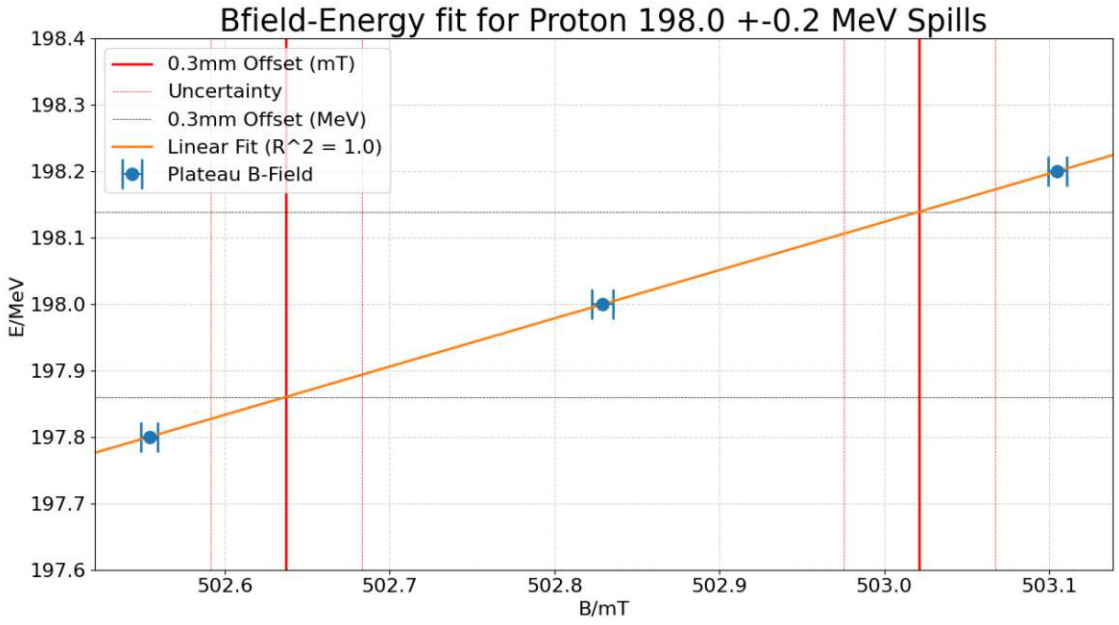

Figure A.18.: Proton 198 MeV B-field linear fit with 0.3 mm limits.

A.1.2. Carbon Ions

Peakfinder Measurements Carbon Ions 120.0 MeV				
Raw Data				
Peak	35.5	mm	6.6031	Gy
R80	35.6	mm	5.28248	Gy
R20	35.8	mm	1.32062	Gy
R80 width	0.4	mm		
Penumbra width	0.2	mm		
Fitted Data				
Peak	35.47	mm	6.466614	Gy
R80_f	35.61	mm	5.173291	Gy
R20	35.78	mm	1.293323	Gy
R80 width	0.41	mm		
Penumbra width	0.17	mm		
Uncertainty	0.040581			
Difference Raw-Fitted Data				
Peak	0.03	mm	0.136486	Gy
R80	0.01	mm	0.109189	Gy
R20	0.02	mm	0.027297	Gy
R80 width	0.01	mm		
Penumbra width	0.03	mm		
R^2	0.98396			

Peakfinder Measurements Carbon Ions 120.6 MeV				
Raw Data				
Peak	35.8	mm	6.6875	Gy
R80	35.9	mm	5.35	Gy
R20	36.1	mm	1.3375	Gy
R80 width	0.3	mm		
Penumbra width	0.2	mm		
Fitted Data				
Peak	35.78	mm	6.518376	Gy
R80_f	35.91	mm	5.214701	Gy
R20	36.08	mm	1.303675	Gy
R80 width	0.4	mm		
Penumbra width	0.17	mm		
Uncertainty	0.04034			
Difference Raw-Fitted Data				
Peak	0.02	mm	0.169124	Gy
R80	0.01	mm	0.135299	Gy
R20	0.02	mm	0.033825	Gy
R80 width	0.1	mm		
Penumbra width	0.03	mm		
R^2	0.991201			

Linear Fit Carbon Ions 120.0 + 0.6 MeV		
Fit Parameters		
k	2.000000	
d	48.780000	
Energy Offset for Range Deviation		
0.3mm	0.600000	MeV
0.5mm	1.000000	MeV
1mm	2.000000	MeV
Standard Deviation	0.080921	MeV
Range Offset for 0.1 MeV Energy Deviation		
Range Offset	0.050000	mm
R^2	1.000000	

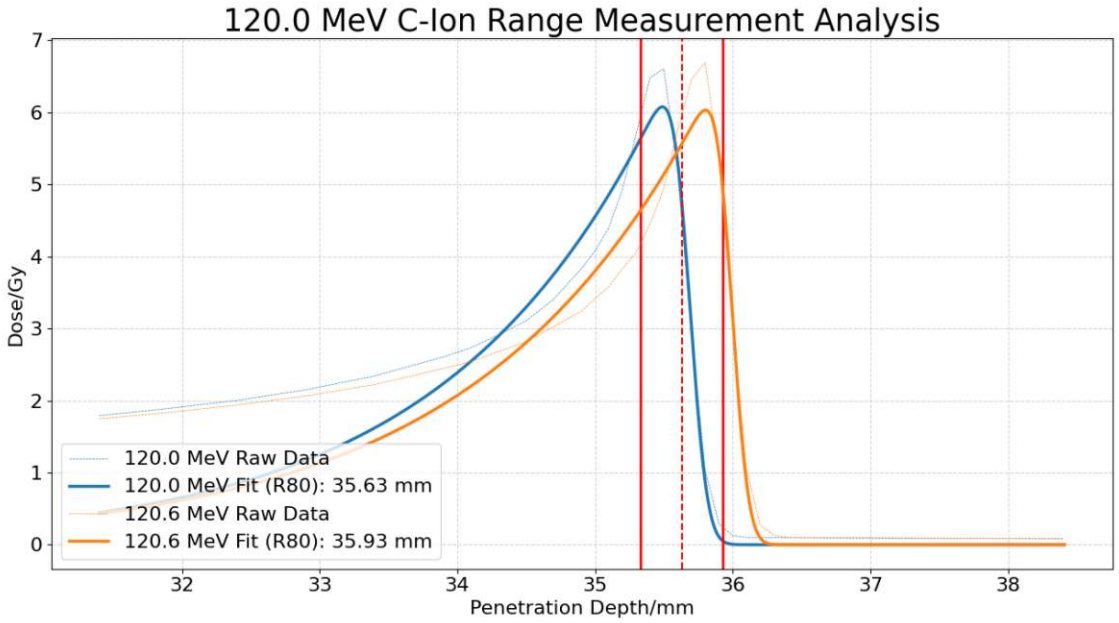

Figure A.19.: C-Ion 120 MeV/u Range Measurement Analysis with 0.3 mm limits.

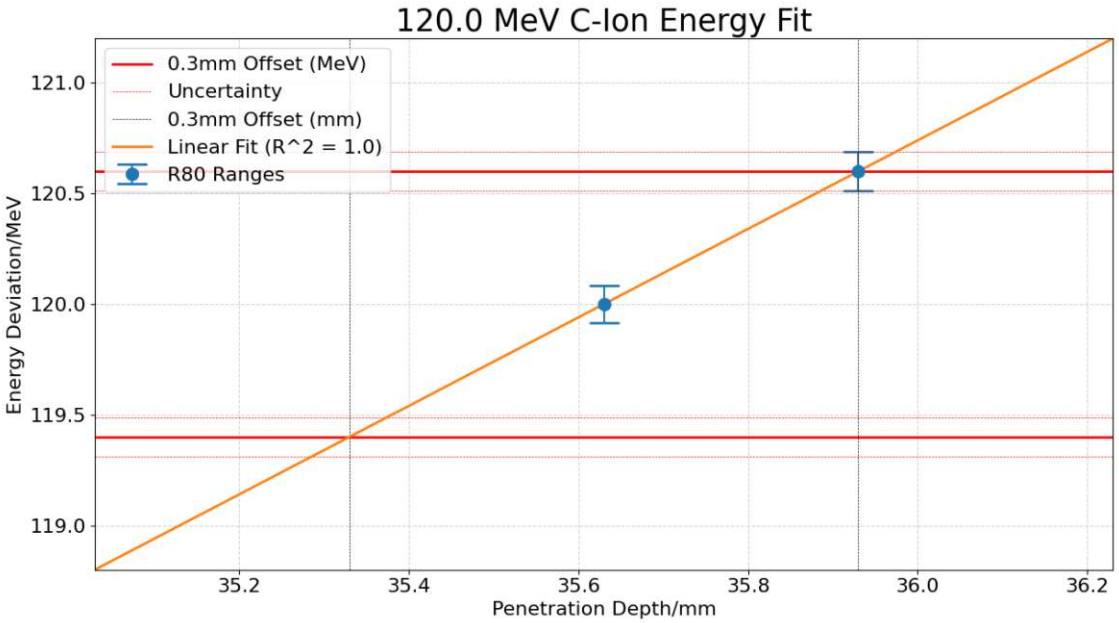

Figure A.20.: Carbon Ion 120 MeV/u linear range fit with 0.3 mm limits.

RFC Measurements Carbon Ions 120.0 + 0.6 MeV		
Carbon 120.0 MeV RFC Measurement		
Mean	1783099.777778	Hz
Median	1783102.0	Hz
Standard Deviation	41.007979	Hz
Carbon 120.6 MeV RFC Measurement		
Mean	1786849.5	Hz
Median	1786867.5	Hz
Standard Deviation	64.955754	Hz
Fit Parameters		
k	0.000160	
d	-165.317099	
RFC Frequency Offset for Range-Deviation		
0.3mm	3749.722222	Hz
0.5mm	6249.537037	Hz
1mm	12499.074074	Hz
Standard Deviation	359.652575	Hz
R^2	1.0	

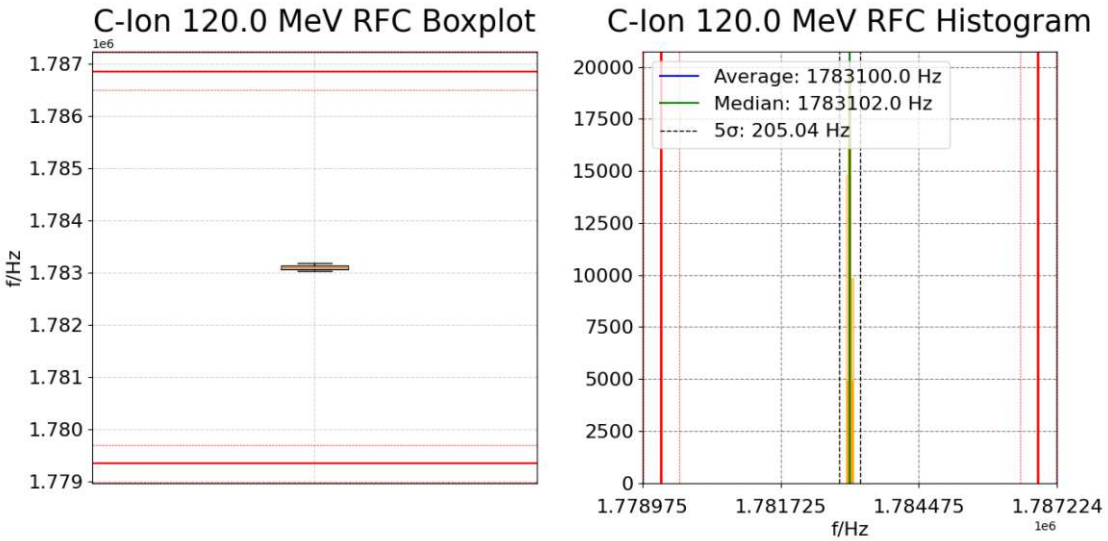

Figure A.21.: Carbon Ion 120 MeV/u RFC Frequency Boxplot & Histogram with 0.3 mm limits.

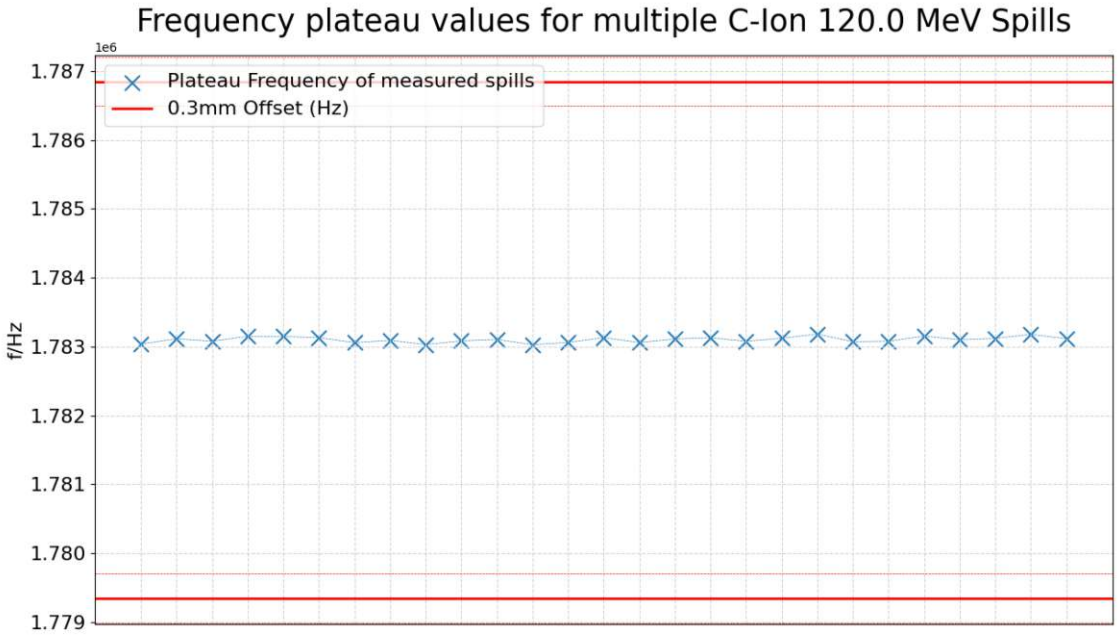

Figure A.22.: Carbon Ion 120 MeV/u measured RFC Frequency spill-plateuas with 0.3 mm limits.

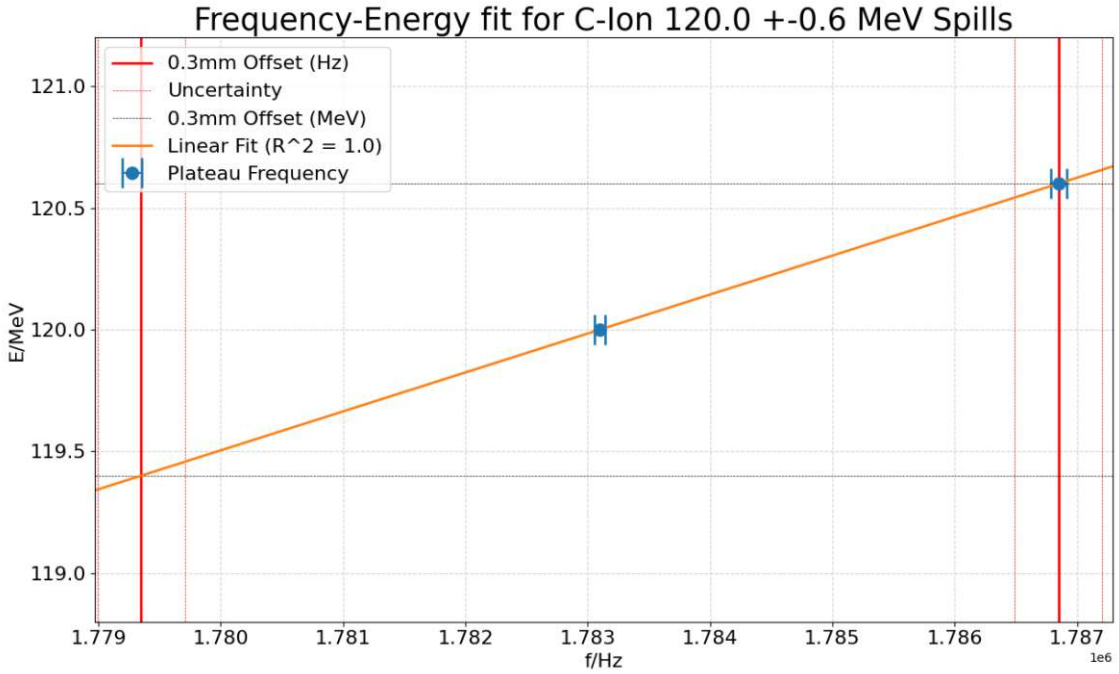

Figure A.23.: Carbon Ion 120 MeV/u RFC Frequency linear fit with 0.3 mm limits.

B-field Measurements Carbon Ions 120.0 + 0.6 MeV		
Carbon 120.0 MeV B-field Measurement		
Mean	765.346229	mT
Median	765.346	mT
Standard Deviation	0.007651	mT
Carbon 120.6 MeV B-field Measurement		
Mean	767.377496	mT
Median	767.377	mT
Standard Deviation	0.008638	mT
Fit Parameters		
k	0.295421	
d	-106.099261	
B-field Offset for Range Deviation		
0.3mm	2.031	mT
0.5mm	3.385	mT
1mm	6.77	mT
Standard Deviation	0.193774	mT
R^2	1.0	

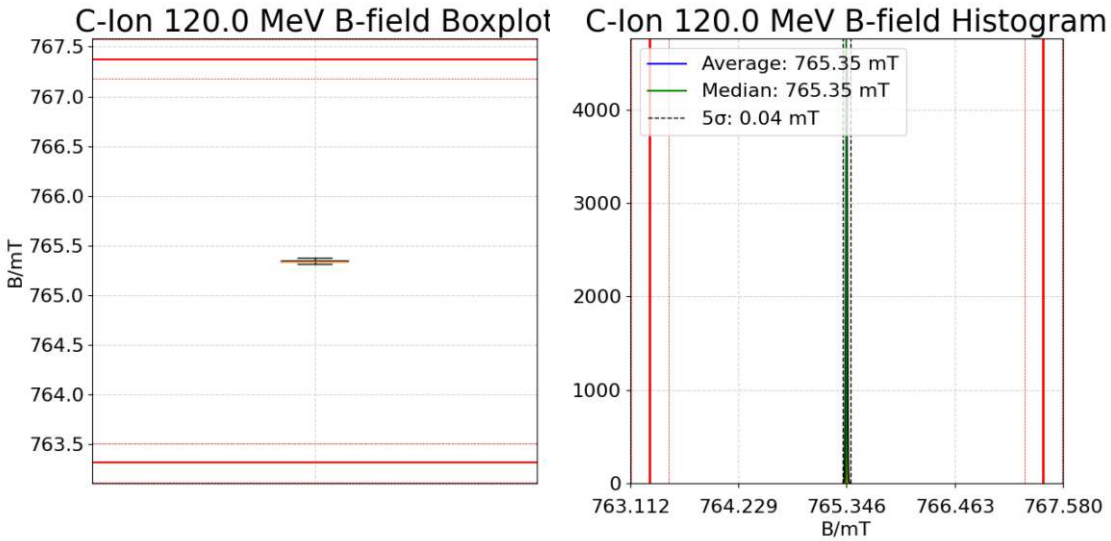

Figure A.24.: Carbon Ion 120 MeV/u B-field Boxplot & Histogram with 0.3 mm limits.

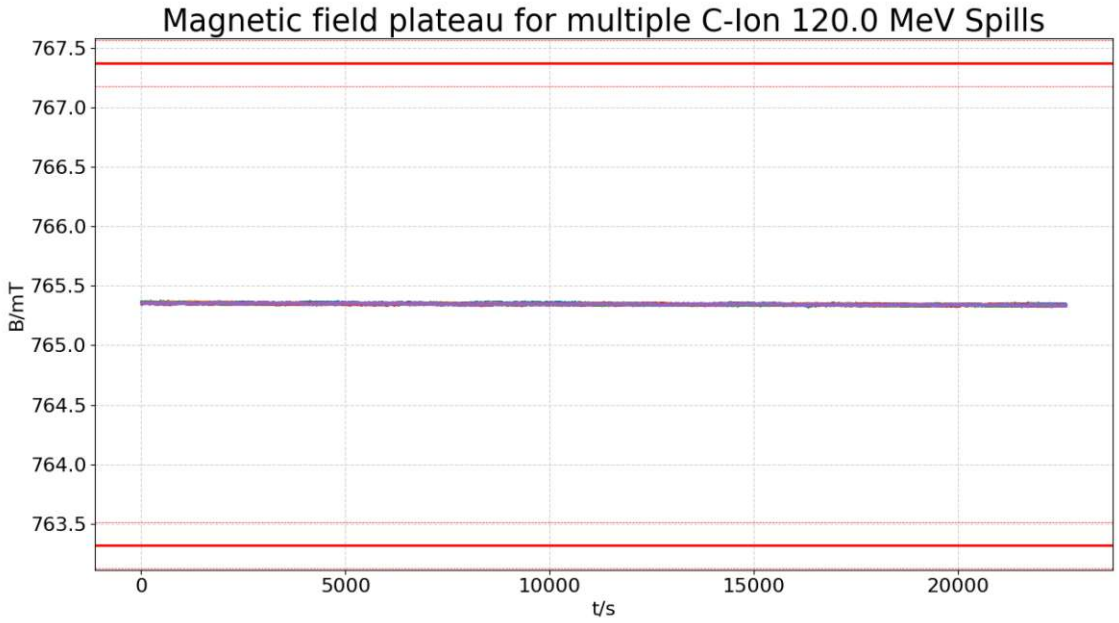

Figure A.25.: Carbon Ion 120 MeV/u measured B-field spill-plateaus with 0.3 mm limits.

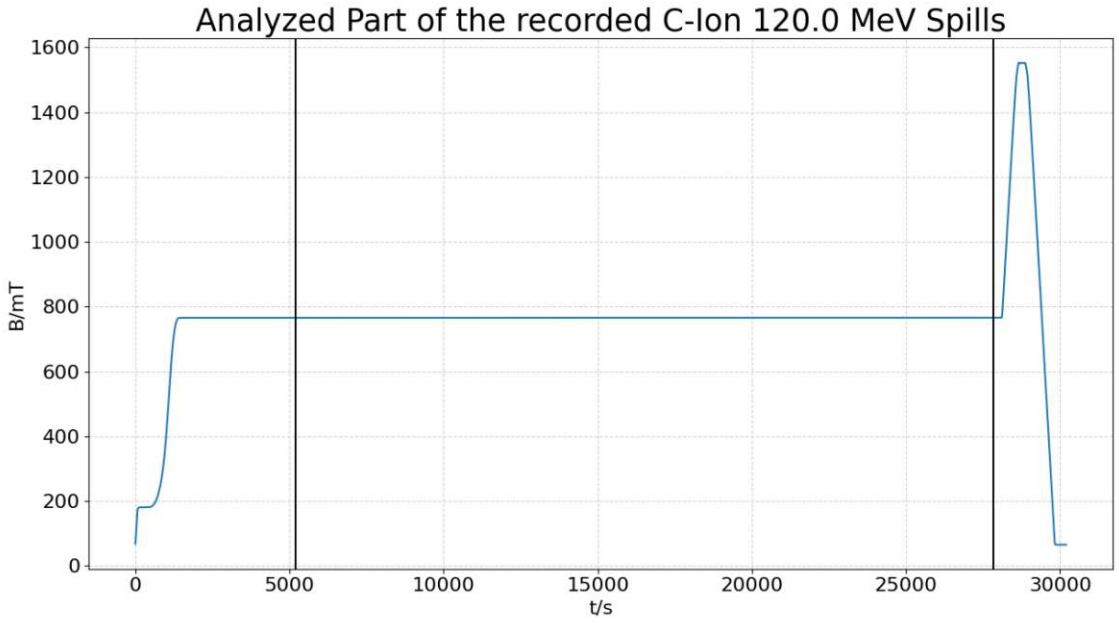

Figure A.26.: Carbon Ion 120 MeV/u analyzed part of the spill in measured B-field.

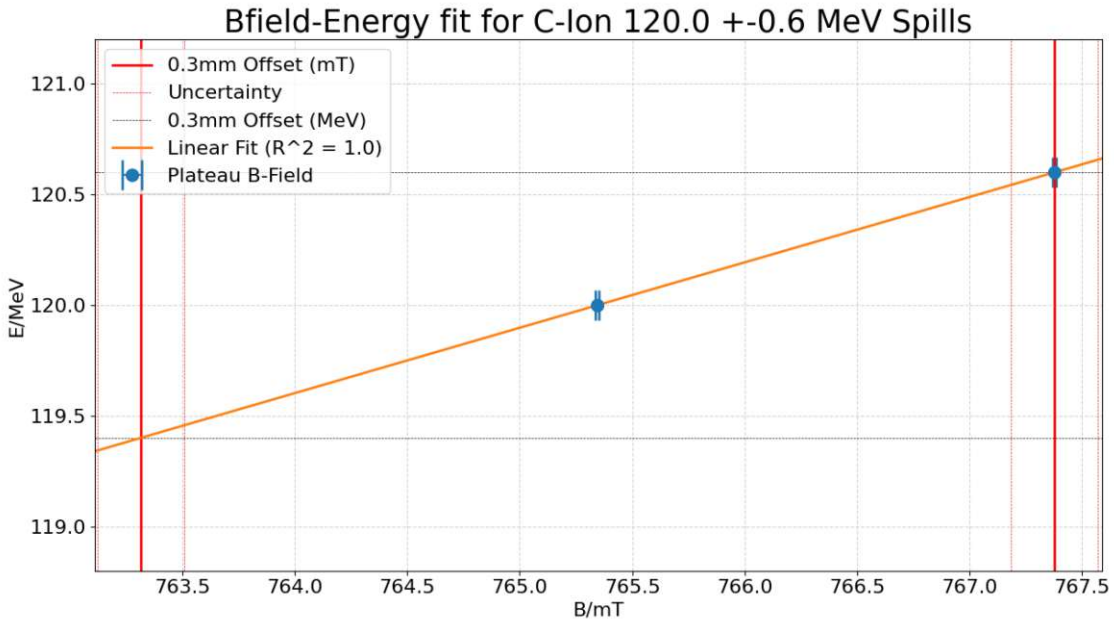

Figure A.27.: Carbon Ion 120 MeV/u B-field linear fit with 0.3 mm limits.

Peakfinder Measurements Carbon Ions 399.9 MeV				
Raw Data				
Peak	271.100000	mm	0.000030	Gy
R80	272.100000	mm	0.000020	Gy
R20	273.500000	mm	0.000010	Gy
R80 width	2.200000	mm		
Penumbra width	1.400000	mm		
Fitted Data				
Peak	271.040000	mm	0.000030	Gy
R80_f	271.980000	mm	0.000020	Gy
R20	273.390000	mm	0.000010	Gy
R80 width	2.060000	mm		
Penumbra width	1.410000	mm		
Uncertainty	0.098220	mm		
Difference Raw-Fitted Data				
Peak	0.060000	mm	0.009946	Gy
R80	0.120000	mm	0.007957	Gy
R20	0.110000	mm	0.001989	Gy
R80 width	0.140000	mm		
Penumbra width	0.010000	mm		
R^2	0.992035			

Peakfinder Measurements Carbon Ions 400.1 MeV				
Raw Data				
Peak	271.300000	mm	0.000003	Gy
R80	272.100000	mm	0.000002	Gy
R20	273.700000	mm	0.000001	Gy
R80 width	2.200000	mm		
Penumbra width	1.600000	mm		
Fitted Data				
Peak	271.270000	mm	0.000003	Gy
R80_f	272.220000	mm	0.000002	Gy
R20	273.600000	mm	0.000001	Gy
R80 width	2.160000	mm		
Penumbra width	1.380000	mm		
Uncertainty	0.072011	mm		
Difference Raw-Fitted Data				
Peak	0.030000	mm	0.013196	Gy
R80	0.120000	mm	0.010556	Gy
R20	0.100000	mm	0.002639	Gy
R80 width	0.040000	mm		
Penumbra width	0.220000	mm		
R^2	0.995562			

Peakfinder Measurements Carbon Ions 400.3 MeV				
Raw Data				
Peak	271.700000	mm	0.000003	Gy
R80	272.300000	mm	0.000002	Gy
R20	273.900000	mm	0.000001	Gy
R80 width	2.200000	mm		
Penumbra width	1.600000	mm		
Fitted Data				
Peak	271.430000	mm	0.000003	Gy
R80_f	272.400000	mm	0.000002	Gy
R20	273.810000	mm	0.000001	Gy
R80 width	2.180000	mm		
Penumbra width	1.410000	mm		
Uncertainty	0.122540			
Difference Raw-Fitted Data				
Peak	0.270000	mm	0.019619	Gy
R80	0.100000	mm	0.015695	Gy
R20	0.090000	mm	0.003924	Gy
R80 width	0.020000	mm		
Penumbra width	0.190000	mm		
R^2	0.985945			

Linear Fit Carbon Ions 400.1 ± MeV		
Fit Parameters		
k	0.945946	
d	142.613514	
Energy Offset for Range Deviation		
0.3mm	0.283784	MeV
0.5mm	0.472973	MeV
1mm	0.945946	MeV
Standard Deviation	0.094356	MeV
Range Offset for 0.1 MeV Energy Deviation		
Range Offset	0.105714	mm
R^2	0.993243	

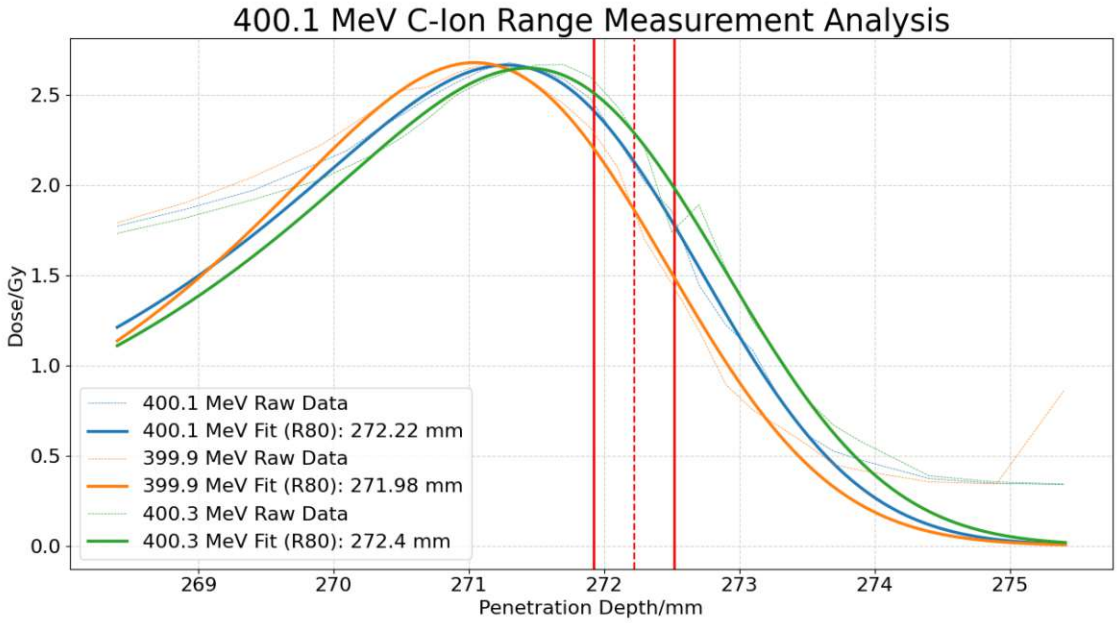

Figure A.28.: C-Ion 400.1 MeV/u Range Analysis with 0.3 mm limits.

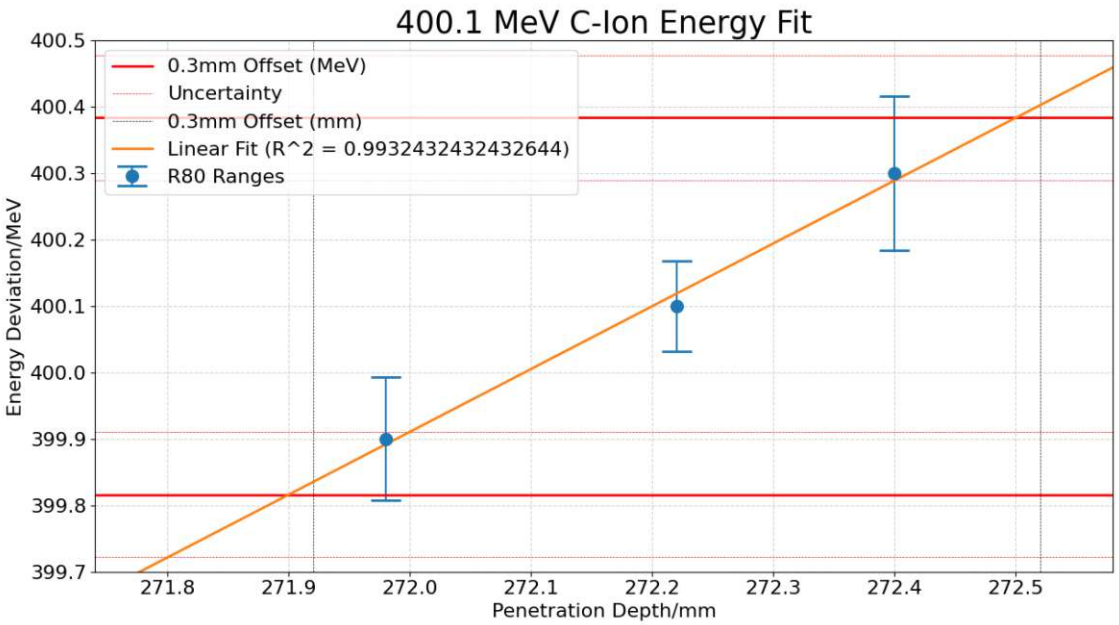

Figure A.29.: Carbon Ion 400.1 MeV/u linear range fit with 0.3 mm limits.

RFC Measurements Carbon Ions 400.1 ± 0.2 MeV		
Carbon Ion 399.9 MeV RFC Measurement		
Mean	2752454.363636	Hz
Median	2752407.000000	Hz
Standard Deviation	204.398685	Hz
Carbon Ion 400.1 MeV RFC Measurement		
Mean	2752794.160000	Hz
Median	2752795.000000	Hz
Standard Deviation	55.859595	Hz
Carbon Ion 400.3 MeV RFC Measurement		
Mean	2753183.545455	Hz
Median	2753182.500000	Hz
Standard Deviation	47.293789	Hz
Fit Parameters		
k	0.000548	
d	-1107.657514	
RFC Frequency Offset for Range Deviation		
0.3mm	518.122461	Hz
0.5mm	863.537435	Hz
1mm	1727.074869	Hz
Standard Deviation	150.647805	Hz
R^2	0.998461	

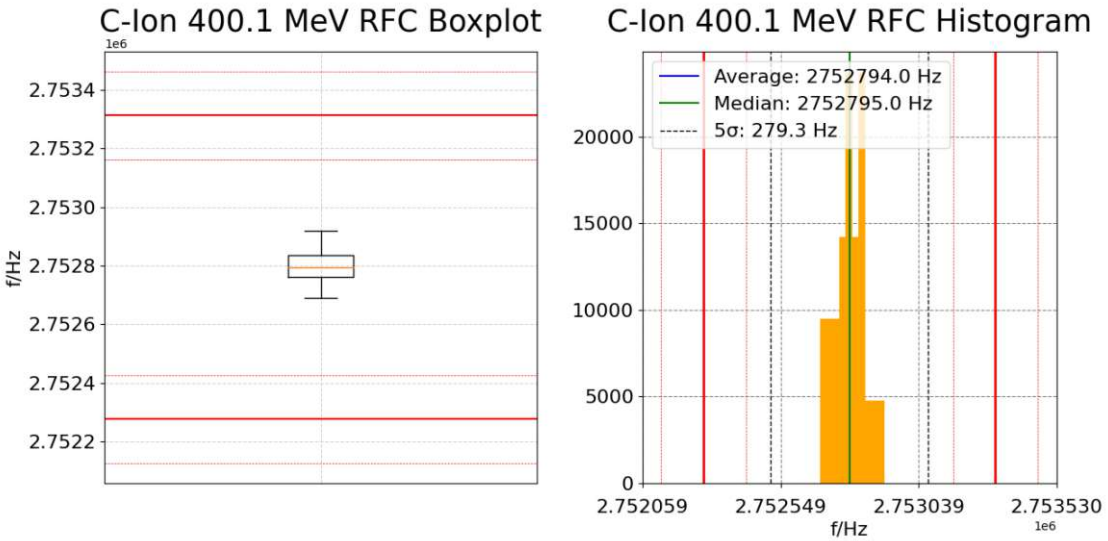

Figure A.30.: Carbon Ion 400.1 MeV/u RFC Frequency Boxplot & Histogram with 0.3 mm limits.

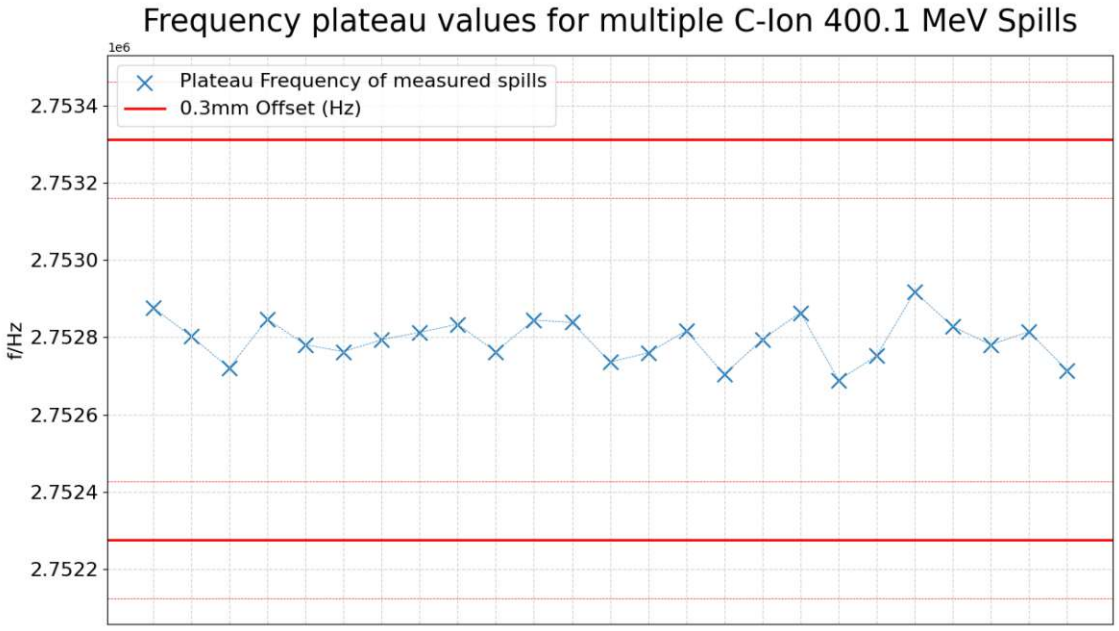

Figure A.31.: Carbon Ion 400.1 MeV/u measured RFC Frequency spill-plateuas with 0.3 mm limits.

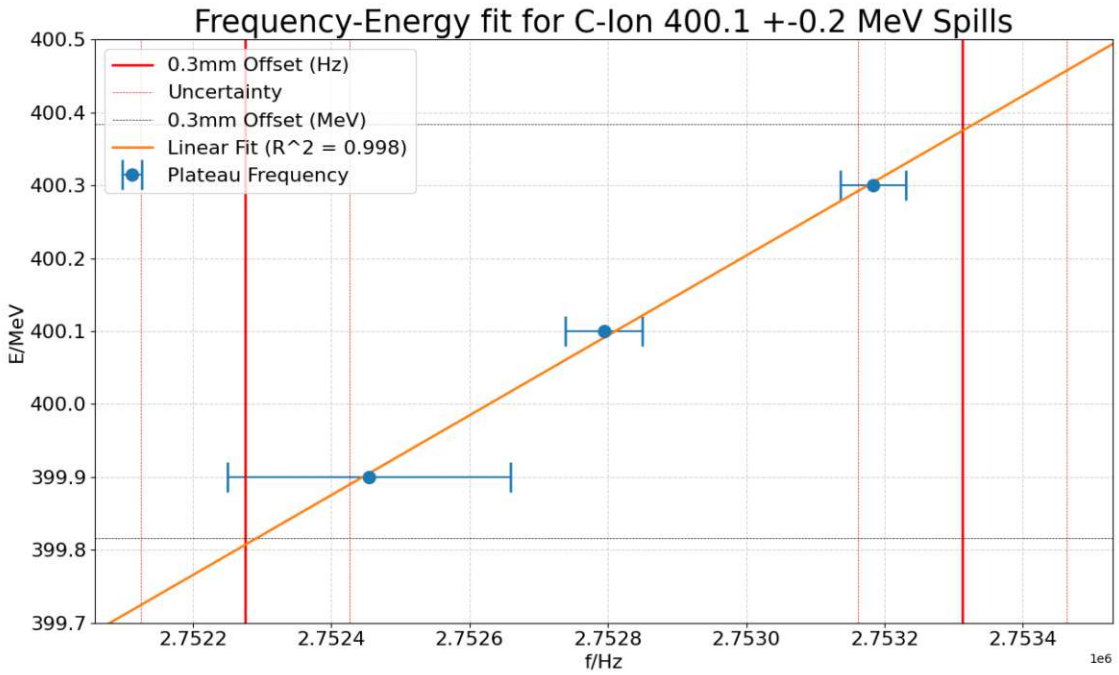

Figure A.32.: Carbon Ion 400.1 MeV/u RFC Frequency linear fit with 0.3 mm limits.

B-field Measurements Carbon Ions 400.1 ± 0.2 MeV		
Carbon Ion 399.9 MeV B-field Measurement		
Mean	1492.401738	mT
Median	1492.404800	mT
Standard Deviation	0.017328	mT
Carbon Ion 400.1 MeV B-field Measurement		
Mean	1492.852671	mT
Median	1492.855400	mT
Standard Deviation	0.017545	mT
Carbon Ion 400.3 MeV B-field Measurement		
Mean	1493.272766	mT
Median	1493.274400	mT
Standard Deviation	0.018522	mT
Fit Parameters		
k	0.459779	
d	-286.279052	
B-field Offset for Range Deviation		
0.3mm	0.617218	mT
0.5mm	1.028696	mT
1mm	2.057392	mT
Standard Deviation	0.145658	mT
R^2	0.999560	

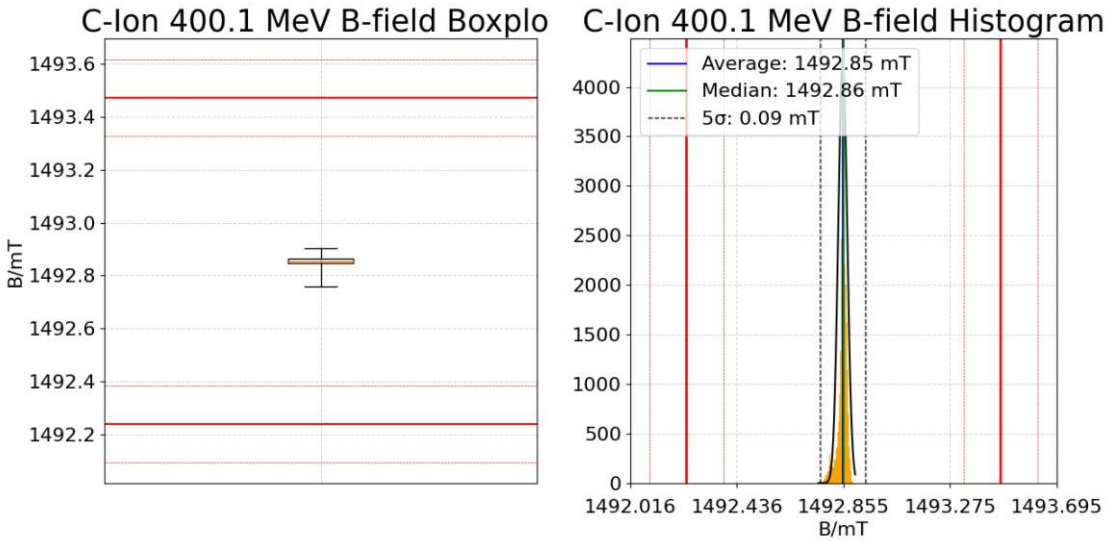

Figure A.33.: Carbon Ion 400.1 MeV/u B-field Boxplot & Histogram with 0.3 mm limits.

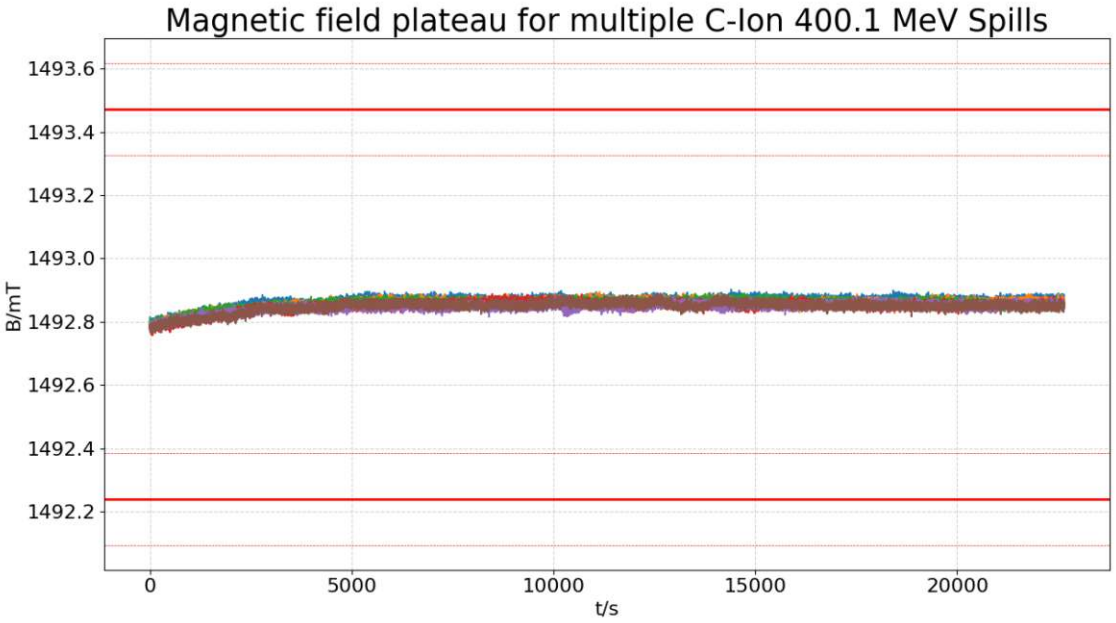

Figure A.34.: Carbon Ion 400.1 MeV/u measured B-field spill-plateaus with 0.3 mm limits.

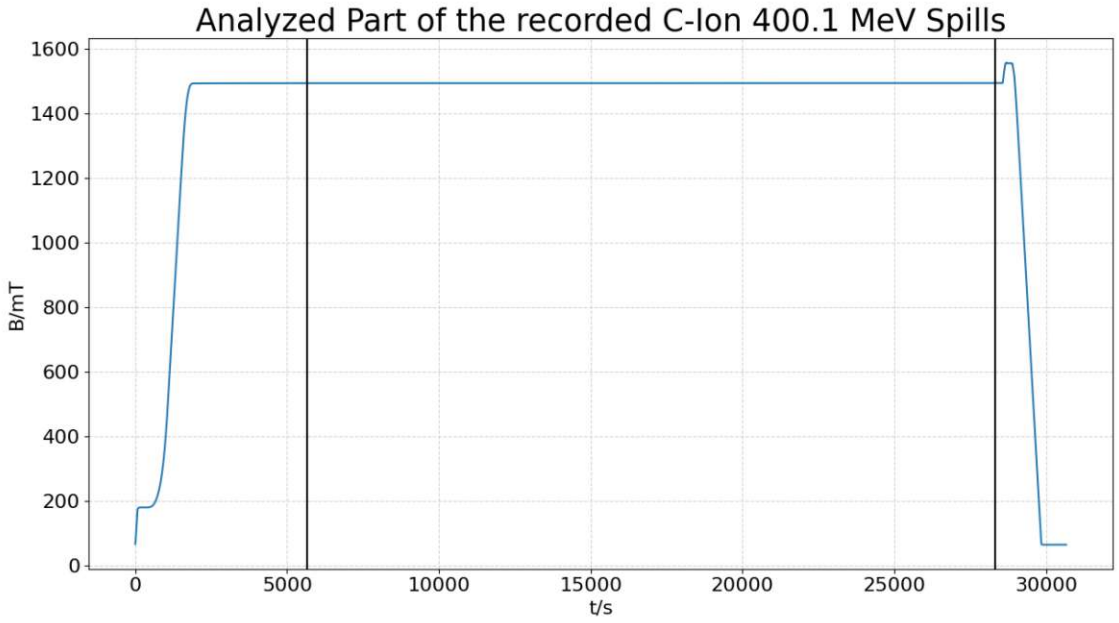

Figure A.35.: Carbon Ion 400.1 MeV/u analyzed part of the spill in measured B-field.

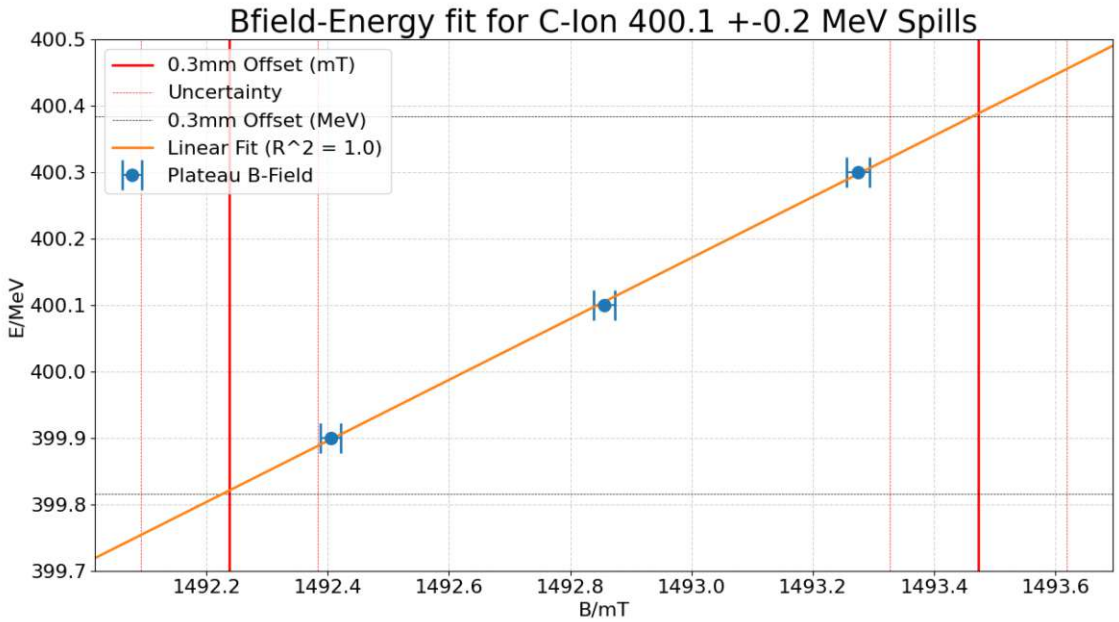

Figure A.36.: Carbon Ion 400.1 MeV/u B-field linear fit with 0.3 mm limits.

B. Workspace Readme

```
######################## README #####################################


### DISCLAIMER ###

The Scripts in this Workspace "grew" over time. They are functional
 but not optimized. There a many funtions, that could be
implemented more practical, efficiently and pretty.
If you want to optimize any of the scripts, please feel free to do
so :).

For more Information about the general topic and the physics behind
 it, see the attached power point presentation [1] or the thesis "
Experimental Validation of the Energy Verification System for Radio
 Frequency Knockout (RFKO) Extractions at MedAustron" [2].



### INTRODUCTION / GENERAL METHOD ###

This Workspace is dedicated to the comparison of measured data of
the particle range, revolution frequency and dipole magnet B-field
of proton and carbon beams at MedAustron to a mathematical model -
specifically for the RFKO extraction method. The compared data
points are the absolute values of these 3 variables at certain
energies + the difference to those absolute values at a certain
range offset (+-0.3mm, +-0.5mm, +-1mm). The absolute values can be
easily found after basic data evaluation - the range offset values
need more calculations. The general method is to "translate" the
range offset into an energy offset, which can than be further "
translated" into frequency and B-field offsets. This is done by
having measurements of all 3 variables for a central energy and
```

```
some nearby offset energies (eg. 198MeV + 197.8MeV and 198.2MeV).
Via linear fit (y = k*x +d) a very localized mathematical model for
 each of the variables can be created (Energy - Range // Energy -
Frequency // Energy - B-field) and hence an offset of any of these
variables can be "translated" in an offset of all other of these
variables.



### OVERVIEW SCRIPTS ###

There are in total 5 scripts doing the analysis:

       - siman_spread.py [](\"hidden\" in \Sim\Proton ; \Sim\Carbon)
       - measan.py []
       - frequency_RL.py [measan]
       - magnetic.py [measan]
       - theory.py [siman_spread, measan, frequency_RL, magnetic]

       - 12.py (creates a mean .mcc file of multiple other .mcc
       files)

       names in [] show the scripts whose results are required

These scripts look for data in specific folders - if you want to
change the folder structure, make sure to also change the paths
accordingly in the scripts. Per default, raw measured data (details
 in respective sections) is to be placed in the main folder -
output will be saved in \Results. Simulated data is to be put in \
Sim\Proton or \Sim\Carbon and respective results will be saved in \
Sim\Proton\Results or \Sim\Carbon\Results. Please note, that
scripts who use results of other scripts will do so out of the
Results folder.

Only "theory.py" will distinguish between on and off momentum
energies. This is done to avoid more variables in every script,
since range and frequency use off- and B-field uses on momentum
energy. Just note that for "measan.py" and "frequency_RL.py" the
corresponding energies are actually lower than displayed. For more
information see [1][2].
```

```
### SIMAN_SPREAD.PY ###

"siman_spread.py" reads TOPAS output data. It will read multiple .
csv files around a central energy by a name consisting of "Output"
+ particle type + energy + "Mono-" + sim-histories + ".csv", so for
 instance "OutputProton198p0Mono-200k.csv". Before executing the
script, make sure the following parameters fit your measurements.

       - title ... Title of output files and charts
       - ns ... Number of simulation histories
       - reb ... Option to rebin the data (y/n)
       - obi ... Original bin number
       - bi ... Chosen bin number if reb == "y"
       - pt1 ... Particle type (p for proton, c for carbon)
       - pe ... Particle energy in the form 198p0
       - multi ... Number of files (for instance 3 for: 197.8,
       198.0, 198.2)
       - acc ... Factor for multiplying the fit resolution while
       searching values (resolution = acc * bin)

The script will now read in the files one by one, performing a
gauss-erf convolution fit and calculating the uncertainty based on
the simulation data. Following this, certain parameters (Peak, R80)
 are determined for the original data and the fit. This will be
repeated automatically for all surrounding energies and finally the
 linear fit is performed. The output files are:

       - pt1 + pe + "curve.png" ... plot of all the curves
       - pt1 + pe + "fit.png" ... plot of all the curves
       - pt + pt + "sim.csv" ... plot of the linear fit


### MEASAN.PY ###

"measan.py" reads the Peakfinder measurements (.mcc files). Per
default, for every .mcc file, the script will want to read in 2
additional files with the same names and an added _1 and _2. The
```

```
reason is, that if you have 2 measurements of the same energy, you
can create the mean values in a seperate file with 12.py and use
the original files for uncertainty calculations via root mean
square [See Disclaimer].

To calculate the energy offset corresponding to a certain range
offset for a certain central energy, you will first have to place
the central energy (eg. 198MeV) together with its surrounding
energies (eg. 197.8Mev and 198.2 MeV), plus the _1 and _2 files for
 each energy into the main folder. The filename should be the
particle type and energy in the form : p198p0.mcc for proton 198.0.
 Before executing the script, make sure the following parameters
fit your measurements.

       - filen ... Number of surrounding energies + central energy
       - title ... Title of output files and charts (should have "_
       en_off" before the file extension)
       - pt ... Particle type (p for proton, c for carbon)
       - WET ... Water equivalent thickness of nozzle + air-gap in
       mm

When starting up the script it will ask you the following
information:

       - Energy fit mode? ... If "y" it will perform a linear
       energy-range fit for the provided energies at the end - "n"
       will just print the curves
       - Draw lines? ... If "y" it will draw lines for Peak, R80, R
       20, etc. in the final chart for this energy - "y" will also
       make this your central energy (see disclaimer)
       - Particle type and energy (p_ty_en)? ... Type in the
       filename in the form also mentioned above - having the
       filenames in this form is also important for the linear fit
       later
       - Filenumber? ... Only relevant if your filename includes
       additional characters in the end, for instance: p198p0_mean.
       mcc

The script will then read in the data and perform a fit with a
gauss-erf convolution. The parameter lists "mini1" and "mini2"
```

```
contain information at which data point of the range measurement to
 start and stop the fit. mini1[4] and mini2[3] means that the fit
will ignore the first 4 and last 3 data points. Per default these
lists are set for a central and 2 surrounding energies, so they
each contain 3 entries.

After the fit, the uncertainties are calculated via the _1, _2
files and certain parameters (Peak, R80) are determined for the
original data and the fit. Following this point, the whole process
will be repeated (filen - 1) times for the surrounding energies
before performing the linear fit and creating the output files:

       - title + "curve.png" ... plot of all the curves
       - title + "fit.png" ... plot of the linear fit
       - title + ".csv" ... output file containing calculated
       information about the input data

Note that, in contrast to other scripts, you will have to put in
draw lines, particle type and energy and filenumber for every
energy.



### FREQUENCY_RL.PY ###

"frequency.py" will read in the frequency measurements. These
measurement files called _____SLC____.msr are to be placed in a
folder called "SLC_ALL_" + particle type and energy in the main
folder, so for instance "SLC_ALL_p198p0". Each .msr file represents
 one spill and the script will read every .msr file in the folder.
Before executing the script, make sure the following parameters fit
 your measurements:

       - filen ... Number of surrounding energies + central energy
       (1 - no fit; 2 - fit with first input + dist; 3 - fit of
       first input with +- dist)
       - dist ... Distance of the surrounding energies to the
       central energy in MeV

When starting up the script it will ask you the following
```

```
information:

        - Particle type and energy? ... Type in the filename in the
        form also mentioned above - having the filenames in this
        form is also important for the linear fit later

The script will now read in the .msr files + the results file of "
measan.py" which has to have particle type, energy and "_en_off" in
 the filename, for instance "p198p0_en_off". After reading in, the
most common frequency of each .msr file is determined (plateau
frequency is stabilized and thus is the only one measured multiple
times) and statistics are determined over all of them. This process
 will repeat automatically for all surrounding energies and the
linear fit will be performed subsequently. The following output
files are then created:

        - p_ty_en + "_freq_chart.png" ... chart including boxplot
        and distribution of the median spill plateau frequencies
        - p_ty_en + "_freq_fit.png" ... plot of the linear fit
        - p_ty_en + "_freq.csv" ... output file containing
        calculated information about the input data



### MAGNETIC.PY ###

"magnetic.py" will read in the B-field measurements. These
measurement files should be called particle type and energy + "mag.
txt" , so for instance "p198p0_mag.txt" and are to be placed the
main folder. For the RFKO EVS project the information about the B-
field was stored in V/10 at a sample rate of 2kHz. To use these
values in mT, they need to be multiplied by a factor of 2000
because of a signal conditioning of 1:10 and the proportionality of
 the Hall probe of 5V/T:

        - x * 10V / (0.005V / mT) = 2000 * x mT

The script will also use the timing events recorded in the SLC
measurements, so make sure, that those are named accordingly.
Before executing the script, make sure the following parameters fit
```

```
 your measurements:

        - mcol ... Column of the measurement in which the
        information is stored
        - filen ... Number of surrounding energies + central energy
        (1 - no fit; 2 - fit with first input + dist; 3 - fit of
        first input with +- dist)
        - dist ... Distance of the surrounding energies to the
        central energy in MeV

When starting up the script it will ask you the following
information:

        - Particle type and energy? ... Type in the filename in the
        form also mentioned above - having the filenames in this
        form is also important for the linear fit later

The script will now read in the the timing events of a random .msr
file + the results file of "measan.py" which has to have particle
type, energy and "_en_off" in the filename, for instance "p198p0_en
_off". After that, the script will scan the selected column (mcol)
of the .txt file, but only start to read, if there is a change of
0.001 in the noise, at which point the measurement is correlated to
 the timing events. For determining the plateau field, only values
for 10 seconds after "StartExtraction|StartChopper" are used. After
 doing this for all recorded spills in the .txt file, statistics
are calculated. This process will repeat automatically for all
surrounding energies and the linear fit will be performed
subsequently. The following output files are then created:

        - p_ty_en + "_mag_chart.png" ... chart including boxplot,
        distribution of the median spill plateau frequencies and a
        figure of the used part of the spill
        - p_ty_en + "_mag_fit.png" ... plot of the linear fit
        - p_ty_en + "_mag.csv" ... output file containing calculated
         information about the input data



### THEORY.PY ###
```

```
"theory.py" contains the mathematical model for RFKO extractions at
 MedAustron and will compare it to the previously analyzed
measurement data. To create the energy-range model, the script will
 also need the output files of "siman_spread.py".
For RFKO extractions only the B-field values will be on momentum,
range and SLC frequency will be off momentum, meaning that the
range and frequency measurements actually correspond to a lower
energy. The script will calculate the off momentum energies at the
beginning and will compare range and frequency measurements only to
 range and frequency calculations at those energies. Before
executing the script, make sure the following parameters fit your
measurements:

       - pt ... Particle type

When starting the script, it will first read in every .csv file in
either \Sim\Proton\Results or \Sim\Carbon\Results (depending on pt)
 and take all values next to "R80_f" to create a polynomial fit of
the 4th order. Then every theoretical value (R, f, B, dE, df, dB)
in a certain energy range is calculated in 10keV steps and the
output files of the other scripts are read in. Finally theoretical
and measurement values are put into an output file and some figures
 are drawn:

       - p_final.csv / c_final.csv
       - p_final_en_abs.png / c_final_en_abs.png
       - p_final_freq_abs.png / c_final_freq_abs.png
       - p_final_mag_abs.png / c_final_mag_abs.png
       - p_final_en_off.png / c_final_en_off.png
       - p_final_freq_off.png / c_final_freq_off.png
       - p_final_mag_off.png / c_final_mag_off.png



For further support contact:

fefeichtinger@gmail.com
```

List of Figures

List of Tables

Bibliography

[1] URL: https://www.medaustron.at.

[2] Michael Benedikt et al. "Overview of the MedAustron design and technology choices". In: 2010, pp. 109–111. URL: https://www.scopus.com/inward/record.uri?eid=2-s2.0-84886875889&partnerID=40&md5=f15c574bb641c7c3c1b254622bdf57c6.

[3] P Bryant and U Dorda. *MedAustron HEBT design report. Engineering Note Version 1.4*. 2010.

[4] Florian Kühteubl. *Design Study of Radio Frequency Knockout Slow Extraction for the MedAustron Synchrotron*. 2020.

[5] Benjamin Cheymol. *Development of beam transverse profile and emittance monitors for the CERN LINAC4*. Dec. 2011.

[6] William R. Leo. *Techniques for Nuclear and Particle Physics Experiments*. 1994. DOI: https://doi.org/10.1007/978-3-642-57920-2.

[7] W. Ulmer and E. Matsinos. "Theoretical methods for the calculation of Bragg curves and 3D distributions of proton beams". English. In: *European Physical Journal: Special Topics* 190.1 (2010), pp. 1–81. URL: www.scopus.com.

[8] F. Hinterberger. *Physik der Teilchenbeschleuniger und Ionenoptik*. 2008. DOI: 10.1007/978-3-540-75282-0.

[9] URL: https://en.wikipedia.org/wiki/File:Linear_accelerator_animation_16frames_1.6sec.gif.

[10] URL: https://de.wikipedia.org/wiki/Zyklotron#/media/Datei:Zyklotron_Prinzipskizze02.svg.

[11] URL: https://www.schoolphysics.co.uk/.

[12] L Badano et al. *Proton-Ion Medical Machine Study (PIMMS), 1*. 2000. URL: https://cds.cern.ch/record/385378.

[13] L Badano and S Rossi. *Characteristics of a betatron core for extraction in a proton-ion medical synchrotron*. Tech. rep. Geneva: CERN, 1997. URL: https://cds.cern.ch/record/327305.

[14] G Feldbauer, M Benedikt, and U Dorda. *Simulations of Various Driving Mechanisms for the 3rd Order Resonant Extraction from the MedAustron Medical Synchrotron*. 2011. URL: https://cds.cern.ch/record/1379901.

[15] Nicola Carmignani et al. "RF-knockout Extraction System for the CNAO Synchrotron". In: *Conf. Proc. C* 100523 (2010). Ed. by Akira Noda et al., THPEB007.

[16] W. Demtröder. *Experimentalphysik 2: Elektrizität und Optik*. Springer-Lehrbuch. Springer Berlin Heidelberg, 2013. ISBN: 9783642299438.

[17] URL: https://www.physik.gym-wst.de/qphase/ga/magnetfeld/03.halleffekt.

[18] URL: https://www.matsusada.com/application/ps/ionization_chambers/.

[19] Wolfgang Demtröder. *Experimentalphysik 4: Kern-, Teilchen- und Astrophysik; 2nd ed.* Berlin: Springer, 2005.

[20] URL: https://de.wikipedia.org/wiki/Z%C3%A4hlrohr#/media/Datei:Kennlinie_Zaehlrohr-GER.svg.

[21] Pauli Virtanen et al. "SciPy 1.0: Fundamental Algorithms for Scientific Computing in Python". In: *Nature Methods* 17 (2020), pp. 261–272. DOI: 10.1038/s41592-019-0686-2.

[22] *CAS - CERN Accelerator School : 5th General Accelerator Physics Course: Jyväskylä, Finland 7 - 18 Sep 1992. CAS - CERN Accelerator School : 5th General Accelerator Physics Course*. 2 volumes, consecutive pagination. CERN. Geneva: CERN, 1994. DOI: 10.5170/CERN-1994-001. URL: https://cds.cern.ch/record/235242.

[23] J. Perl et al. "TOPAS: An innovative proton Monte Carlo platform for research and clinical applications". English. In: *Medical physics* 39.11 (2012), pp. 6818–6837. URL: www.scopus.com.

[24] J. Allison et al. "Geant4 developments and applications". In: *IEEE Transactions on Nuclear Science* 53.1 (2006), pp. 270–278. DOI: 10.1109/TNS.2006.869826.

[25] J. Allison et al. "Geant4 developments and applications". In: *IEEE Transactions on Nuclear Science* 53.1 (2006), pp. 270–278. DOI: 10.1109/TNS.2006.869826.

[26] PTW. *PEAKFINDER Water Column T41030 with Servo Control Unit T41027 user manual*. 2008.

[27] Felix Ulrich-Pur et al. "Commissioning of low particle flux for proton beams at MedAustron". In: *Nuclear Instruments and Methods in Physics Research, Section A: Accelerators, Spectrometers, Detectors and Associated Equipment* 1010 (2021). DOI: 10.1016/j.nima.2021.165570. URL: https://www.scopus.com/inward/record.uri?eid=2-s2.0-85108640554&doi=10.1016%5C%2fj.nima.2021.165570&partnerID=40&md5=e33857ad0bbf64dbba16f654ee2324ce

[28] URL: http://www.gaussmeter.com.cn.

[29] Koen Lambrechts. *Fitting the Bragg peak for accurate proton range determination*. 2015.

[30] Joint Committee for Guides in Metrology. *Evaluation of measurement data — Guide to the expression of uncertainty in measurement*. 2008.